Supplementary Materials for

A molecular mediator for reductive concerted proton-electron transfers via electrocatalysis

Matthew J. Chalkley*, Pablo Garrido-Barros*, Jonas C. Peters†

*These authors contributed equally to this work.
†Corresponding author. Email: jpeters@caltech.edu

Published 14 August 2020, *Science* **369**, 850 (2020)
DOI: 10.1126/science.abc1607

This PDF file includes:

Table of Contents:

S1. Experimental Details:

S1.1. General Considerations:

All manipulations were carried out using standard Schlenk or glovebox techniques under an N_2 atmosphere. Solvents were deoxygenated and dried by thoroughly sparging with N_2 followed by passage through an activated alumina column in a solvent purification system by SG Water, USA LLC. Non-halogenated solvents were tested with sodium benzophenone ketyl in tetrahydrofuran (THF) in order to confirm the absence of oxygen and water. Deuterated solvents were purchased from Cambridge Isotope Laboratories, Inc., degassed, and dried over activated 3-Å molecular sieves prior to use.

Cobaltocenium hexafluorophosphate ($[Cp_2Co][PF_6]$), trifluoromethanesulfonimide, triflic acid, ferrocene, acetophenone (PhC(O)Me), 2-pentanone ($C_3H_7C(O)Me$) 4-methoxyacetophenone, 4-methylacetophenone, 4-chloroacetophenone, 4-trifluoromethylacetophenone, 2,3-diphenyl-2,3-butanediol, dodecane, 4-cyanoaniline ($^{4\text{-CN}}PhNH_3$), 2-chloroaniline ($^{2\text{-Cl}}PhNH_2$), 4-chloroaniline ($^{4\text{-Cl}}PhNH_2$), samarium diiodide (SmI_2), and tetrabutylammonium hexafluorophosphate ($[TBA][PF_6]$) were all used as purchased. Ferrocenium triflate,(*33*) 4-lithiodimethylaniline,(*34*) anilinium triflate acids,(*17*) deutero-substituted 4-cyanoaniline ($^{4\text{-CN}}PhND_2$),(*35*) and $[D(OEt_2)_2][BAr^F{}_4]$ ($[BAr^F{}_4]^-$ = tetra(2,6-trifluoromethylphenyl)borate)(*36*) were synthesized as described previously.

S1.2 Computational Details:

All calculations were performed using the ORCA 4.0 program.(*37*, *38*) In cases where crystal structures were available these coordinates were used as the input. The calculations were performed using the TPSS (meta-GGA)(*39*) functional with def2-TZVPP(*40*, *41*) on all atoms, Grimme-d3 dispersion correction,(*42*) and SMD(*43*) solvation modelling acetonitrile. That optimized structures represented true stationary points was checked by doing a single-point frequency calculations on the optimized structure and ensuring that there were no significant negative frequencies (*i.e.*, all frequencies are ≥ -50 cm^{-1}).

Reduction potentials were determined via calculated exchange reactions with ferrocene/ferrocenium. The pK_a values were likewise determined via exchange reactions with 2-chloroanilinium/2-chloroaniline.(*23*) The hydricity values were determined via exchange reactions with $CO_2/[HCO_2]^-$ (formate).(*44*) The bond dissociation free energies (BDFEs) were calculated directly using the free energy of H·.

S1.3 EPR Spectroscopy:

X-band (9.4 GHz) continuous wave (CW) electron paramagnetic resonance (EPR) spectra were acquired using a Bruker EMX spectrometer equipped with a Super High-Q (SHQE) resonator using Bruker Win-EPR software (ver. 3.0). Spectra were acquired at 77 K using a vacuum-insulated quartz liquid nitrogen immersion dewar inserted into the EPR resonator.

S1.4 X-Ray Crystallography:

X-ray diffraction (XRD) studies were carried out at the Beckman Institute Crystallography Facility on a Bruker Kappa Apex II diffractometer (Mo Kα radiation). Structures were solved using SHELXS or SHELXT and refined against F^2 on all data by full-matrix least squares with SHELXL.(*45*) All of the solutions were performed in the Olex2 program.(*46*) The crystals were mounted on a glass fiber under Paratone N oil.

S1.5 Electrochemistry:

A CHI instruments 600B electrochemical analyzer was used for all electrochemical data collection.

Cyclic voltammetry (CV), linear sweep voltammetry (LSV) and differential pulse voltammetry (DPV) experiments were carried out in a one-compartment three-electrode cell using a glassy carbon (GC) disk or a boron doped diamond (BDD) disk as the working electrode (3 mm diameter), a Pt wire as the counter electrode, and a Ag/AgOTf (5 mM) reference electrode. Details for the CVs and LSVs are noted as they appear. DPVs were obtained with the following parameters: amplitude= 50 mV, step height=4 mV, pulse width= 0.05 s, pulse period= 0.5 s and sampling width= 0.0167 s. $E_{1/2}$ values for the reversible waves were obtained from the half potential between the oxidative and reductive peaks and for irreversible processes are estimated according to the potential at the I_{max} in DPV measurements. For all measurements were IR compensation was applied accounting for 85% of the total resistance. All of the reported potentials are referenced to the ferrocenium/ferrocene couple ($Fc^{+/0}$) used as internal standard.

Controlled potential coulometry (CPC) experiments were carried out in a gas-tight single compartment cell using a BDD plate (dimensions 1x2 cm) working electrode, a Ag/AgOTf (5 mM) reference electrode, and a GC plate (dimensions 1x5 cm) counter elecrode. The solution was stirred throughout the CPE. In a typical experiment, 7 ml of DME of 0.2 M [TBA][PF_6] was added to the electrochemical cell. Then, 120.5 mg of toluenesulfonic acid (100 mM) and 40 μL of acetophenone (50 mM) were added. In experiments using cobaltocene as catalyst, either 3.2 mg of [(Cp)**Co**(Cp^N)][OTf] (1 mM) or 2.3 mg of [Cp_2Co][PF_6] (1 mM) were then added.

GC electrodes were pretreated by polishing with 1, 0.3 and 0.05 μm alumina paste followed by rinsing with water and acetone. The BDD electrodes were pre-treated according to literature procedures.(*47*)

S1.7 Products quantification:

Upon completion of CPEs, the headspace is analyzed for H_2 via gas chromatography with a thermal conductivity detector (GC-TCD). A 100 μL Hamilton syringe was used to sample the headspace and to inject into the GC-TCD. GC-TCD was performed in the Environmental Analysis Center (Caltech) using a HP 5890 Series II instrument with N_2 as the carrier gas. A calibration curve was determined by direct injection of known volumes of H_2.

The solution was then analyzed with electrochemical methods (CV and DPV) prior to work-up for analysis of the products. The work-up procedure consisted first of quenching the solution with a solution 2 M HCl in ether. After 5 min of stirring, the solvent was evaporated under reduced pressure until dry. The resulting solids were extracted with ether (3 x 10 mL) and the solution was subsequently washed with an aqueous solution containing 0.1 M Na_2CO_3 (20 mL). The aqueous phase was further washed with ether (5 x 20 mL), and the organic fractions were added to the previous ether solution and evaporated until dryness. Finally, the resulting solid was extracted with 4 mL of ethyl acetate and filtered through celite yielding the analysis solution which was then used for detection and quantification of the products and remaining substrate.

The formation of product was analyzed via gas chromatography coupled to either mass spectrometry (GC-MS, for products identification) or flame ionization detector (GC-FID, for product identification and quantification). For the GC-MS, 0.1 ml of the analysis solution was diluted to a total volume of 0.5 ml with ethyl acetate and used for injection. For the GC-FID analysis, 0.5 mL of the analysis solution were used for the injection after addition of 50 μL of an internal standard solution consisting in dodecane 0.206 M in ethyl acetate. The chromatograms were compared with those of pure compounds obtained from commercial sources. Calibration curves were determined using ethyl acetate solution of the pure compounds at known concentrations with added dodecane as internal standard. GC-MS was performed in an Agilent 5975C instrument in the Center for Catalysis and Chemical Synthesis (Caltech). GC-FID was performed using an Agilent 6850 instrument equipped with an Agilent HP-5 5% phenyl methyl siloxane capillary column (J&W Scientific). The yield of the reaction was calculated as percentage of product detected compared to the theoretical amount.

The Faradaic efficiency (FE) was calculated taking into account the total charge passed during the CPE (Q), the number of electrons involved in the formation of one molecule of the final product detected (n_e = 2 per pinacol or H_2 produced), the Faraday constant (F) and the mols of product (2,3-diphenyl-2,3-butanediol or H_2) produced ($N_{product}$), following **Eq. S1**:

$$FE = \frac{N_{product}}{\frac{Q}{n_e F}} \qquad \textbf{(Eq. S1)}$$

1.8 IR Spectroscopy:

Spectra were obtained using a Bruker Alpha Platinum ATR spectrometer with OPUS software in a glovebox under an N_2 atmosphere.

S1.9 UV-vis Spectroscopy:

Measurements were taken on a Cary 50 UV/Visible spectrophotometer using a 1 cm quartz cell connected to a round-bottom flask and sealed with a Teflon stopcock. Variable temperature measurements were collected with a Unisoku CoolSpek cryostat mounted within the Cary spectrophotometer. The 2-MeTHF:THF mixture used herein to solutions that remain mixable at very low temperatures has been reported previously.(*48*)

S1.10 NMR Spectroscopy:

^{1}H and ^{13}C chemical shifts are reported in ppm relative to tetramethylsilane, using residual solvent resonances as internal standards. Solution phase magnetic measurements were performed by the method of Evans.(*49*)

S1.11 XPS Spectroscopy:

The BDD working electrode used in the CPE experiment with [(Cp)**Co**(Cp^{N})][OTf] as the catalyst was analyzed by X-ray photoelectron spectroscopy using a Kratos AXIS Ultra XPS instrument with an X-ray source consisting of a monochromatic Al Kα line at 1486.6 eV, with 0.2 eV resolution at the full width half maximum. XPS results were analyzed using CasaXPS, Casa Software Ltd. The XPS instrument was calibrated to the Au $4f_{7/2}$ peak at 84 eV. Samples were calibrated to the adventitious carbon peak at 284.5 eV.

S2. Synthetic Details:

Cp(η^4-$C_5H_5PhNMe_2$)Co- A suspension of $[Cp_2Co][PF_6]$ (399 mg, 1.2 mmol) was stirred in THF (6 mL) at −78 °C. To this was added dropwise a room temperature, THF (10 mL) solution of 4-lithiodimethylaniline (152 mg, 1.2 mmol, 1 eq.) causing the reaction mixture to go orange. The suspension was allowed to stir at −78 °C for three hours and then allowed to warm slowly to room temperature at which point the reaction became homogeneous. The reaction was then evaporated to dryness and the solid was extracted with pentane (3x 100 mL). The pentane was then filtered through an alumina plug and the solution was evaporated. (Yield: 148 mg, 40%)

^{1}H NMR (C_6D_6, 400 MHz, 298 K): δ 6.90 (2H, "d", J = 8.5 Hz), 6.58 (2H, "d", J = 8.5 Hz), 5.13 (2 H, t, $^3J_{H-H}$ = 2 Hz), 4.63 (5H, s, Cp), 3.94 (1H, t, $^3J_{H-H}$ = 2.4 Hz), 2.93 (2H, dt $^3J_{H-H}$ = 2.4, 2.0 Hz), 2.51 (6H, s, NMe_2).

$^{13}C\{^1H\}$ NMR (CD_3CN 100 MHz, 298 K): δ 149.57, 135.96, 126.35, 113.05, 79.42, 75.01, 56.35, 45.99, 40.67

Elemental Analysis: (calculated) C: 69.90%, H: 6.52%, N: 4.53%; (observed) C: 70.33%, H: 6.85%, N: 4.51%

(Cp)Co(Cp^N): Cp(η^4-$C_5H_5PhNMe_2$)Co (50 mg, 0.16 mmol) was dissolved in 5:1 methylcyclohexane:benzene (20 mL total). The solution was brought to reflux and allowed to reflux for 18 hours during which the solution went from orange to dark red. After 18 hours, the solution was cooled to room temperature. The solvent was removed under reduced pressure. The solid was extracted with pentane (3x 5 mL) and filtered through celite. The solution was then concentrated by slow evaporation of pentane to yield crystalline (Cp)**Co**(Cp^N). (Yield: 29.4 mg, 59%)

^{1}H NMR (C_6D_6, 400 MHz, 298 K): δ 11.32 (2H), 4.99 (6H), −2.82 (2H), −41.49 (2H), −47.45 (2H), −50.12 (5H).

μ_{eff} (C_6D_6, 298 K): 1.75.

Elemental Analysis: (calculated) C: 70.13%, H: 6.21%, N: 4.54%; (observed) C: 70.01%, H: 6.30%, N: 4.62%

[(Cp)Co(Cp^N)][OTf]: (Cp)**Co**(Cp^N) (43.7 mg, 0.147 mmol) was dissolved in THF (3 mL) and added dropwise to a stirring a THF suspension (3 mL) of ferrocenium triflate (50 mg, 0.149 mmol) was added dropwise. The solution was allowed to stir for thirty minutes and then the solvent was evaporated. The solid was washed with pentane to remove ferrocene and then the solid was redissolved in THF. The solution was then layered with toluene and cooled to −35 °C. Overnight crystalline material of [(Cp)**Co**(Cp^N)][OTf] was deposited. (Yield: 48 mg, 74 %)

^{1}H NMR (CD_3CN, 400 MHz, 298 K): δ 7.61 (2H, d, $^3J_{H,H}$ = 8.5 Hz), 6.78 (2H, d, $^3J_{H,H}$ = 8.5 Hz), 6.07 (2 H, s), 5.69 (2H, s), 5.39 (5H, s, Cp), 3.01 (6H, s, NMe_2).

^{19}F NMR (CD_3CN, 376 MHz, 298 K): δ 76.6.

$^{13}C\{^1H\}$ NMR (CD_3CN 100 MHz, 298 K): δ 153.10, 129.91, 113.21, 86.11, 84.52, 78.99, 68.25, 40.30, 26.22.

Elemental Analysis: (calculated) C: 55:97%, H: 4.89%, N: 2.61%; (observed) C: 55.28%, H: 4.59, N: 2.60. (includes one molecule of toluene, which is persistently observed in recrystallized material)

[(Cp)Co(Cp^{NH})][OTf]$_2$: A dimethoxyethane (5 mL) solution of [(Cp)**Co**(Cp^{N})][OTf] (37 mg, 0.08 mmol) was stirred. To this a dimethoxyethane (1 mL) solution of HOTf (60.8 mg, 39 μL, 0.40 mmol) was added dropwise. This caused the reaction to turn yellow and then over thirty minutes a yellow solid precipitated. The solvent was removed and the solid residue was extracted with acetonitrile. The acetonitrile solution was filtered through celite and then concentrated. Layering with toluene containing 0.40 mmol of HOTf at −35 °C led to the precipitation of crystalline material of [(Cp)**Co**(Cp^{NH})][OTf]$_2$ overnight. (Yield: 25 mg, 50%)

^{1}H NMR (C_6D_6, 400 MHz): δ 10.08 (1H, br s, N*H*Me$_2$) 7.96 (2H, "d", $^{3}J_{H,H}$ = 8.6 Hz), 7.73 (2H, "d", $^{3}J_{H,H}$ = 8.6 Hz), 6.26 (2 H, tt, J = 2.3, 2.3 Hz), 5.83 (2H, tt, J = 2.3, 2.3 Hz), 5.54 (5H, s, Cp), 3.29 (6H, s, NH*Me*$_2$).

^{19}F NMR (CD_3CN, 376 MHz, 298 K): δ 76.5.

^{13}C NMR (C_6D_6, 100 MHz): δ 144.31, 130.72, 122.69, 102.76, 86.93, 86.12, 82.57, 66.16, 47.73.

Elemental Analysis: (calculated) C: 39.55%, H: 3.32%, N: 2.31%; (observed) C: 39.23%, H: 3.44%, N: 2.35%

S.3. NMR Spectroscopy:

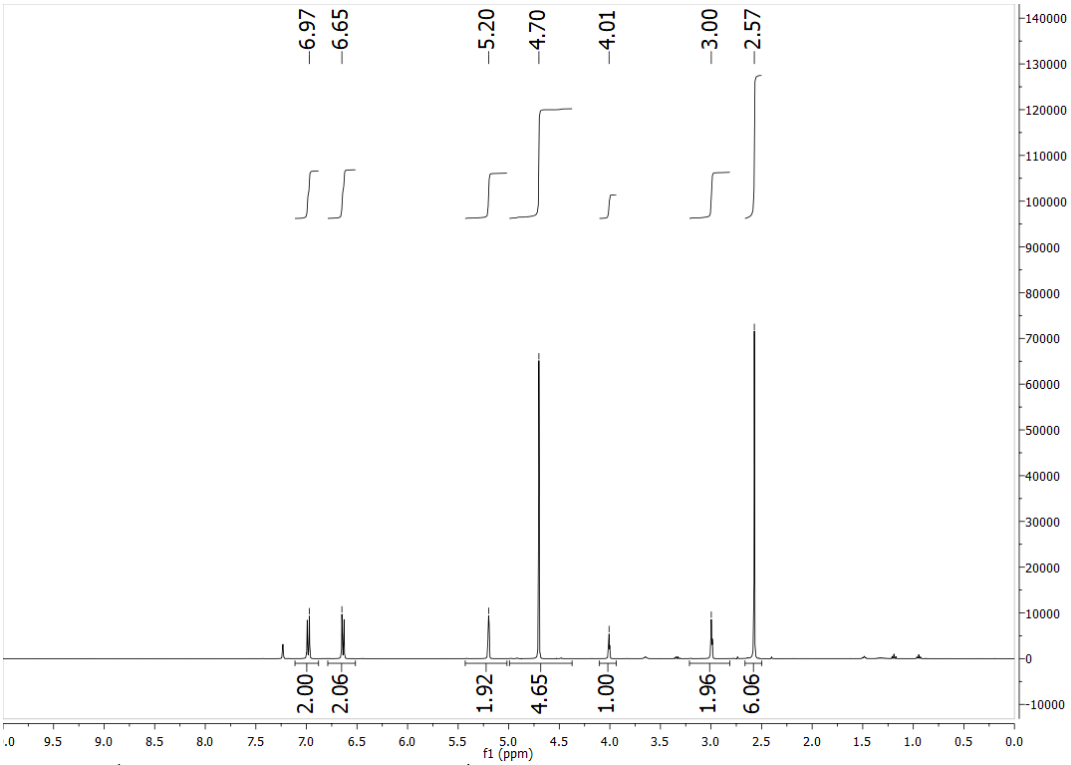

Fig. S1. ^{1}H NMR spectrum of Cp(η^4-$C_5H_5PhNMe_2$)Co in C_6D_6, 400 MHz, 298 K.

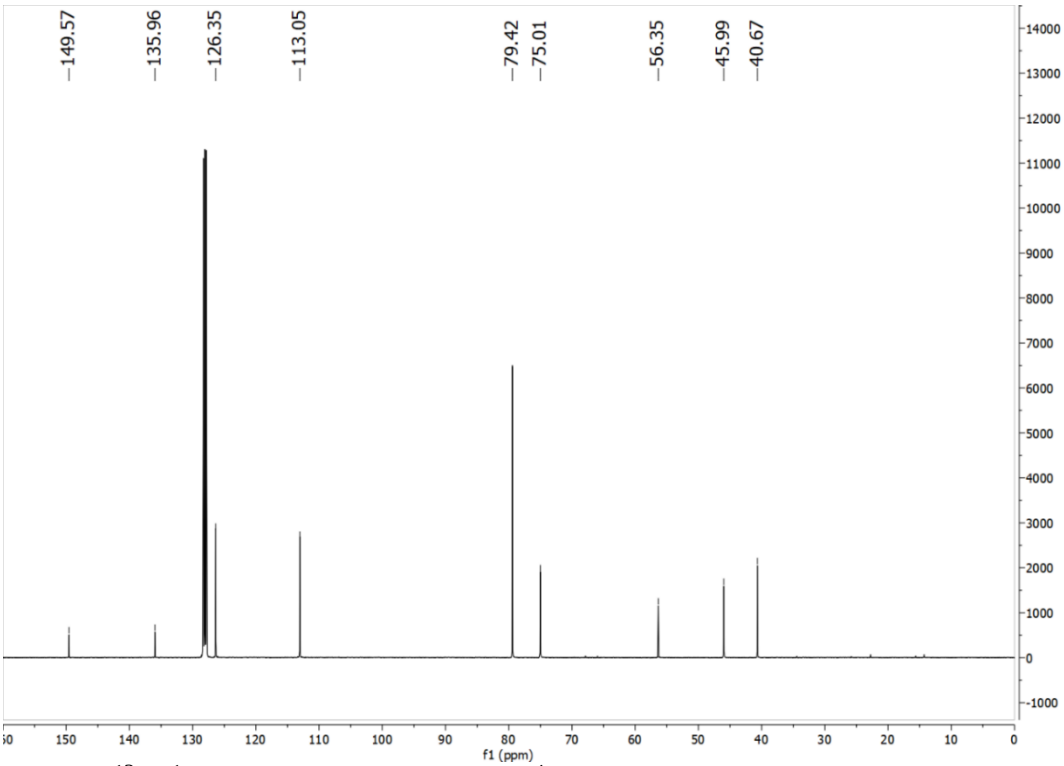

Fig. S2. ^{13}C{^{1}H} NMR spectrum of Cp(η^4-$C_5H_5PhNMe_2$)Co in C_6D_6, 100 MHz, 298 K.

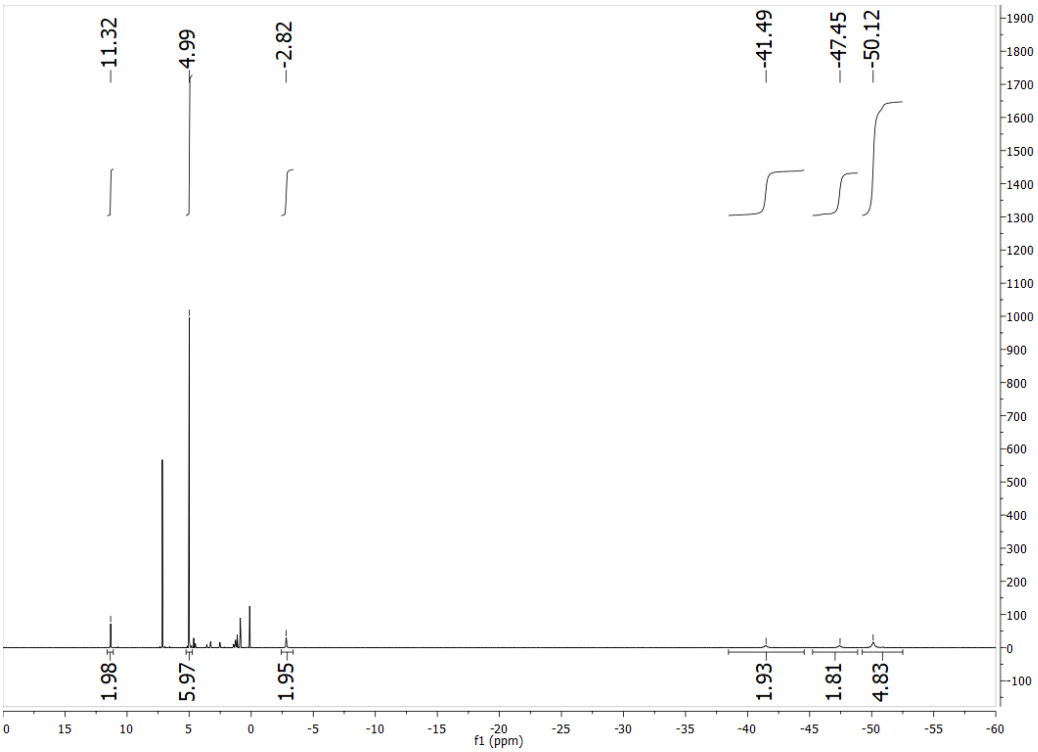

Fig. S3. ^{1}H NMR spectrum of (Cp)**Co**(Cp^{N}) in CD_3CN, 400 MHz, 298 K.

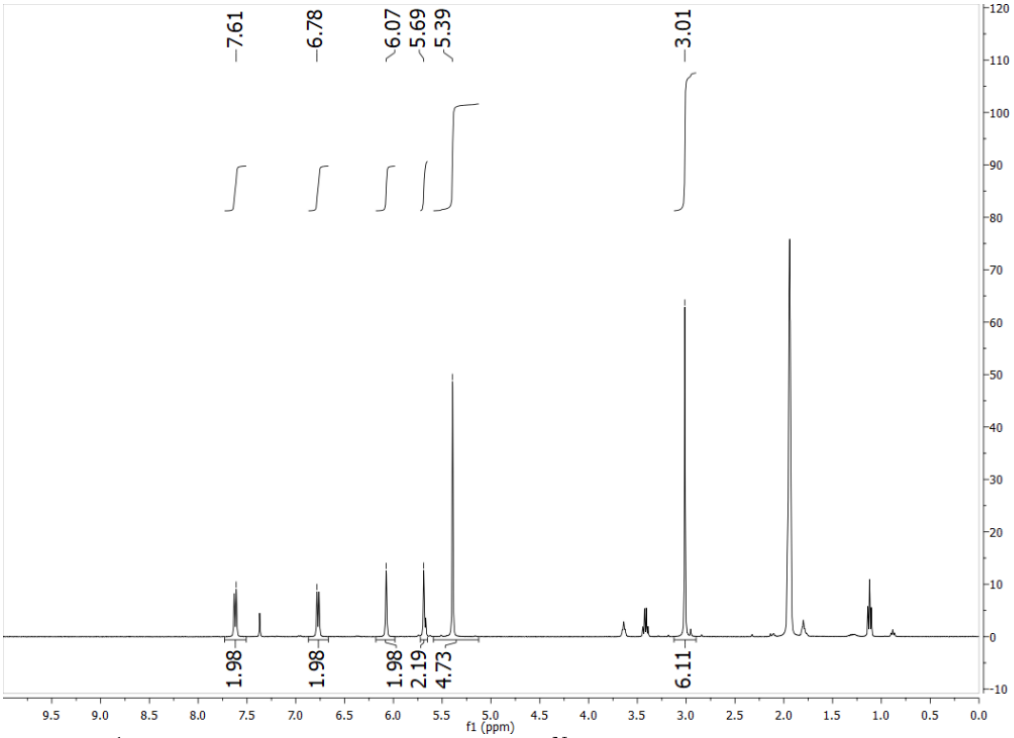

Fig. S4. ^{1}H NMR spectrum of [(Cp)**Co**(Cp^{N})][OTf] in CD_3CN, 400 MHz, 298 K.

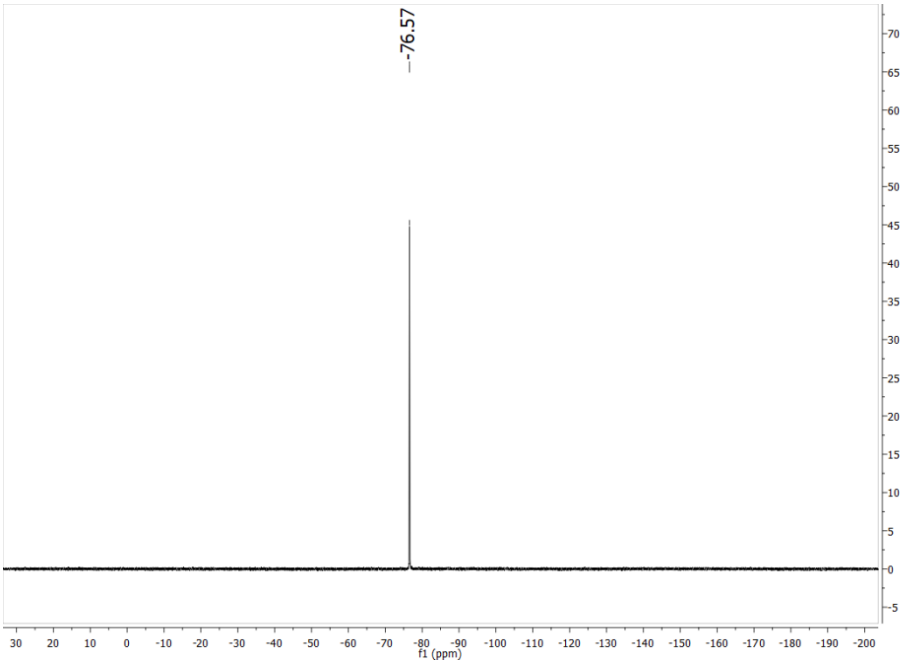

Fig. S5. ^{19}F NMR spectrum of [(Cp)**Co**(Cp^N)][OTf] in CD_3CN, 376 MHz, 298 K.

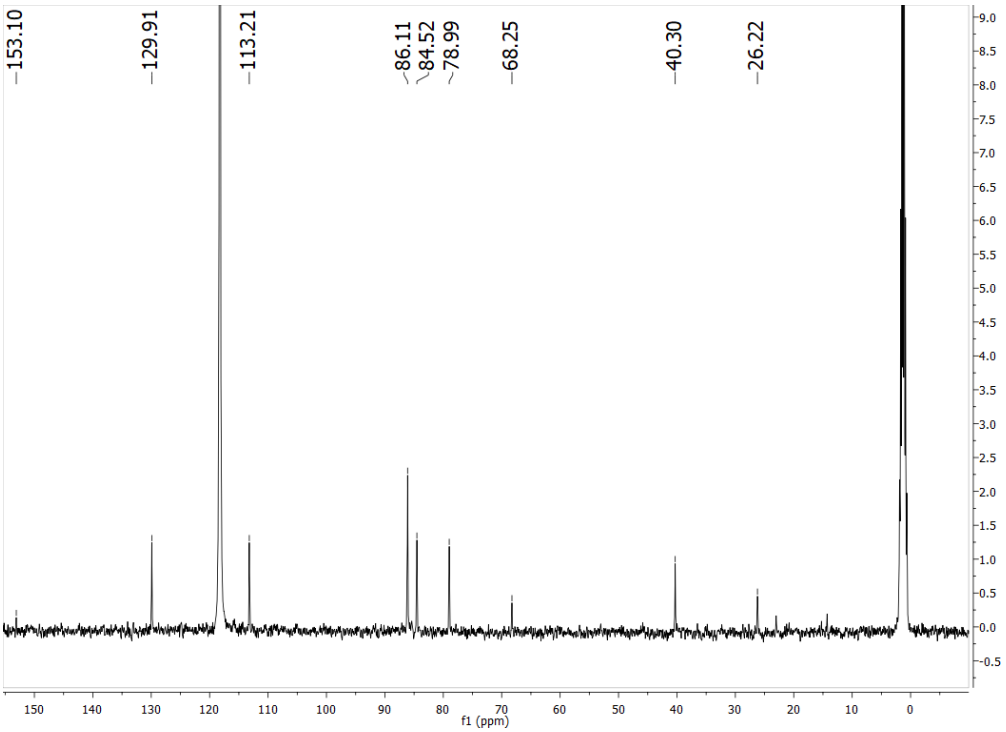

Fig. S6. $^{13}C\{^1H\}$ NMR spectrum of [(Cp)**Co**(Cp^N)][OTf] in CD_3CN, 100 MHz, 298 K.

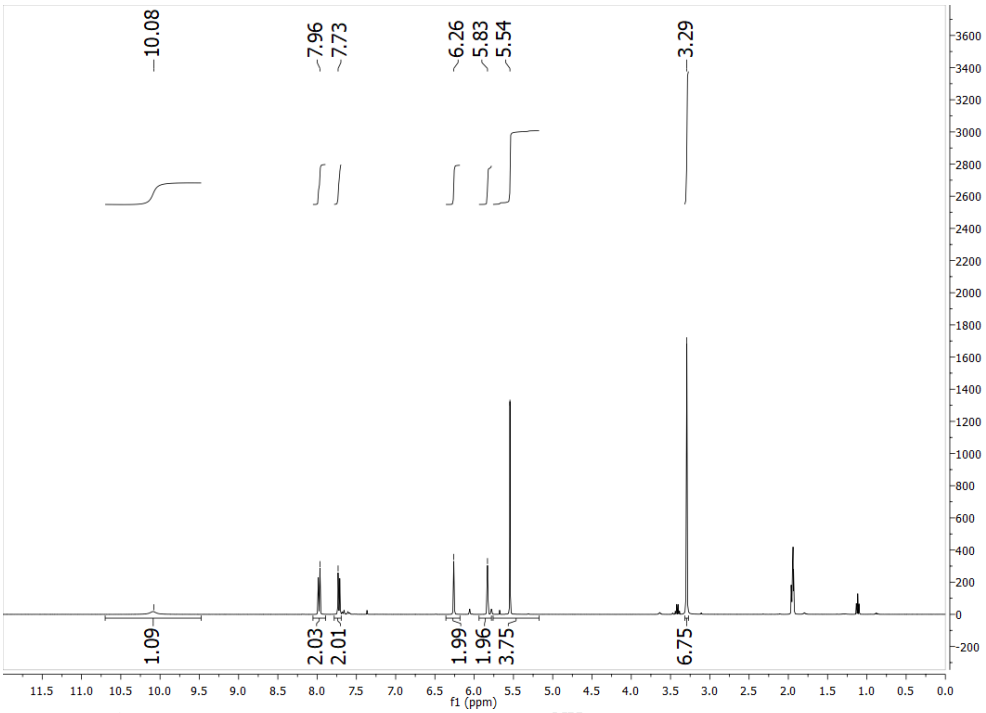

Fig. S7. ^{1}H NMR spectrum of [(Cp)**Co**(Cp^{NH})][OTf]$_2$ in CD_3CN, 400 MHz, 298 K.

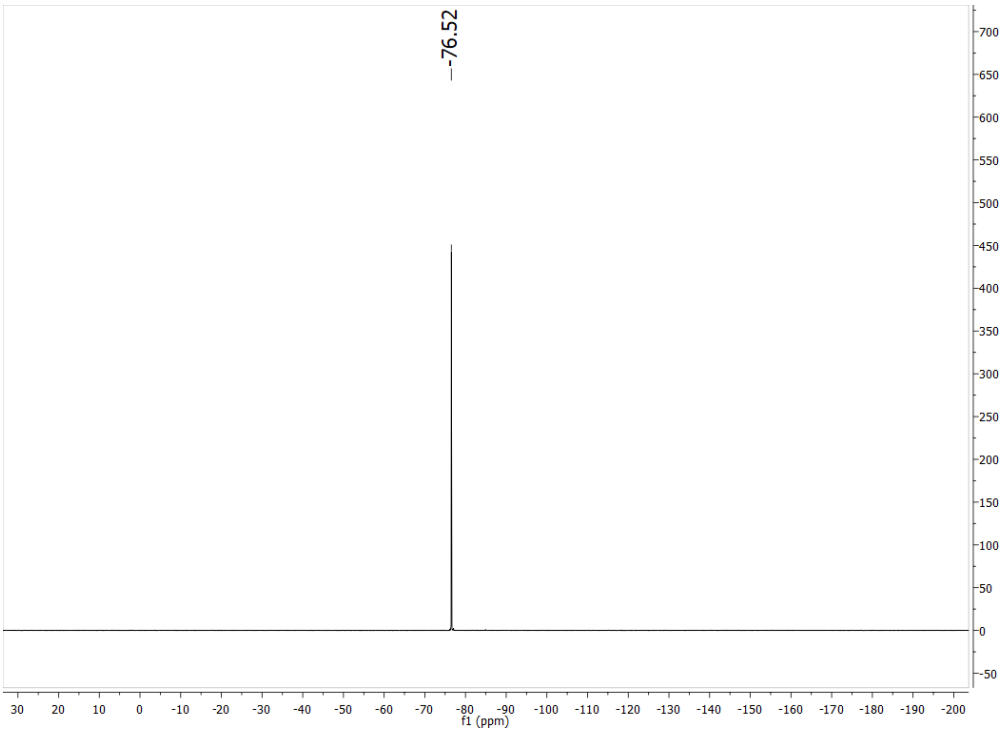

Fig. S8. ^{19}F NMR spectrum of [(Cp)**Co**(Cp^{NH})][OTf]$_2$ in CD_3CN, 376 MHz, 298 K.

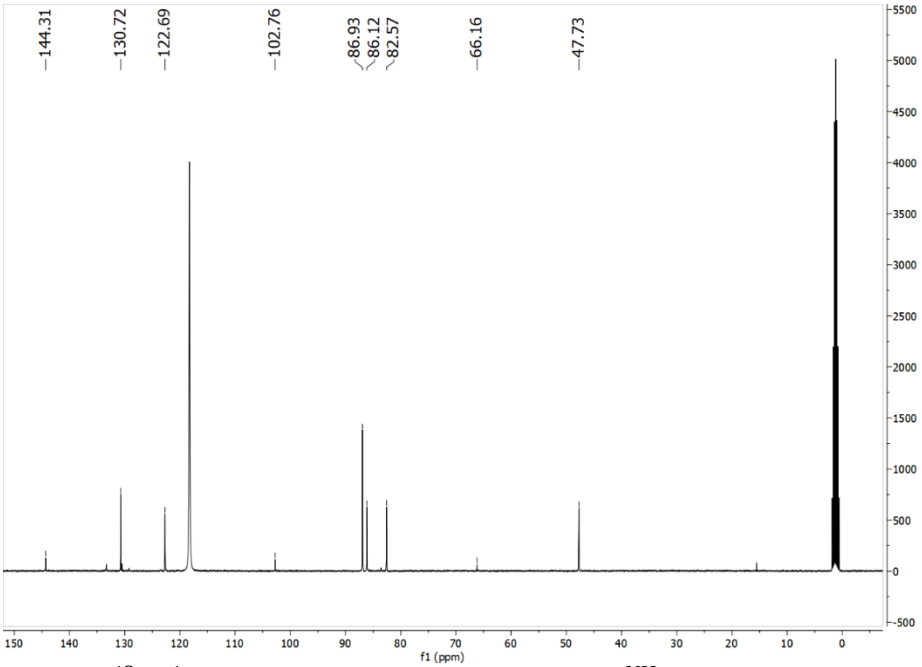

Fig. S9. $^{13}C\{^{1}H\}$ NMR spectrum of [(Cp)**Co**(Cp^{NH})][OTf]$_2$ in CD_3CN, 100 MHz, 298 K.

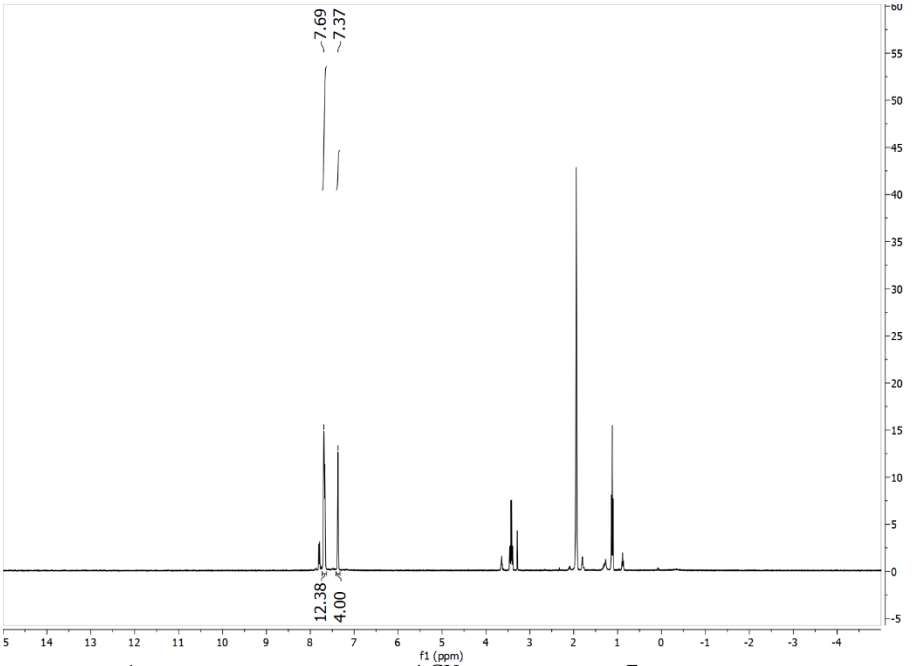

Fig. S10. ^{1}H NMR spectrum of [$^{4\text{-CN}}PhND_3$][$BAr^F{}_4$] in CD_3CN, 400 MHz, 298 K. The NH_3 protons which typically resonate at 8.3 ppm are clearly absent. The peaks for the anilinium are lying under the $BAr^F{}_4$ resonances at 7.69 consistent with previous reports.(*50*) The acid was synthesized via the reaction of [$^{4\text{-CN}}PhND_2$] (30 mg, 0.25 mmol) with one equivalent of [$D(OEt_2)_2$][$BAr^F{}_4$] (252.82 mg, 0.25 mmol) in ether (2 mL) at room temperature. Purification was achieved by filtering through celite, concentrating the solvent, and layering with pentane at −35 °C overnight. The crystalline precipitate was then washed with pentane and dried before use.

S.4. UV-Vis Spectroscopy:

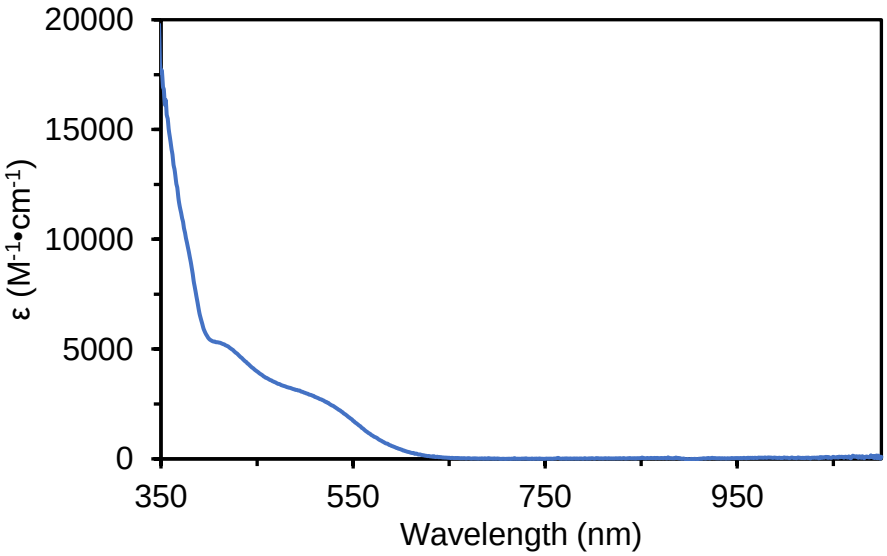

Fig. S11. UV-Vis spectrum at room temperature for [(Cp)**Co**(Cp^N)] in 2-MeTHF:THF solution (4:1).

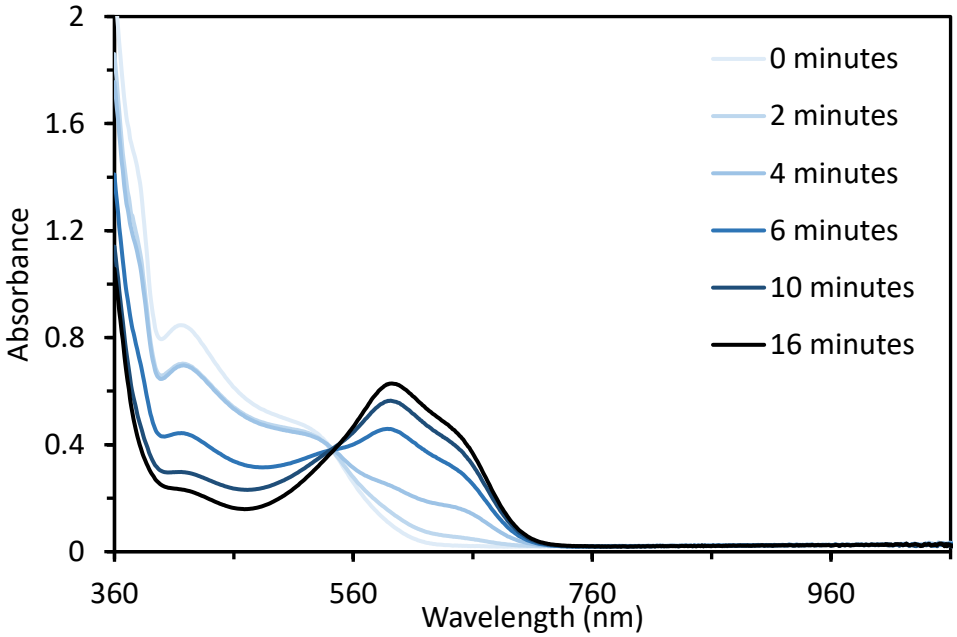

Fig. S12. UV-Vis spectra of the reaction of trifluoromethanesulfonimide and (Cp)**Co**(Cp^N) at −130 °C in 2-MeTHF:THF solution (4:1) showing conversion to [(Cp)**Co**(Cp^{NH})][NTf_2].

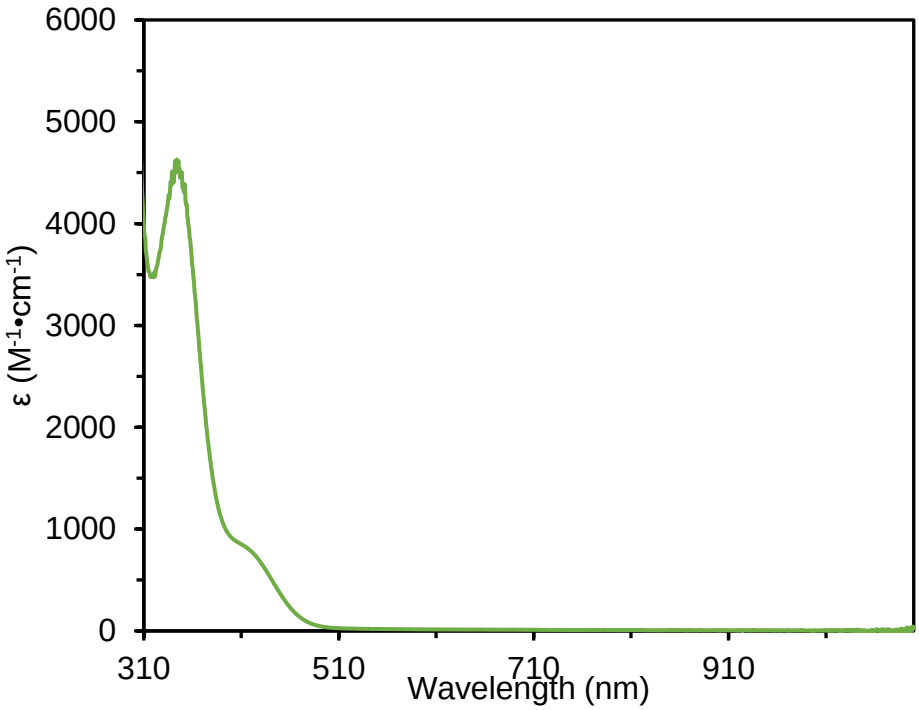

Fig. S13. UV-Vis spectrum at room temperature for [(Cp)**Co**(Cp^{NH})][OTf]$_2$ in acetonitrile.

S5. EPR Spectroscopy

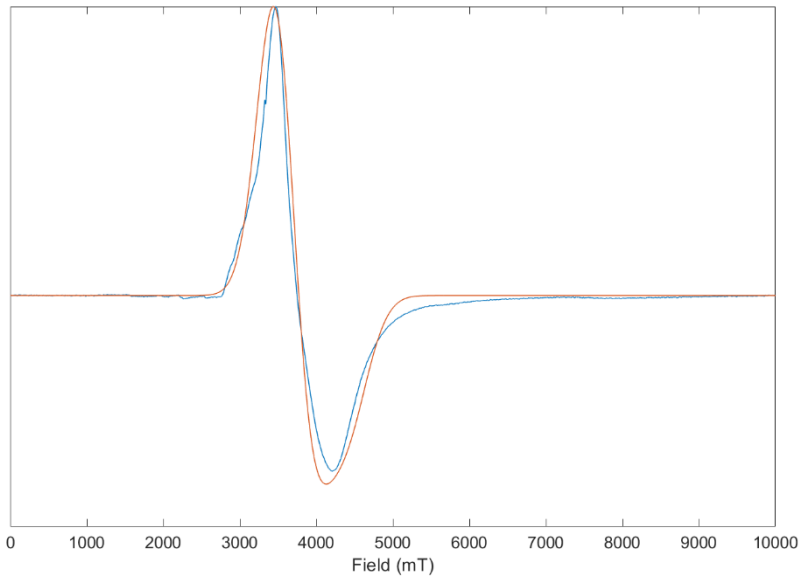

Fig. S14. (blue) X-band EPR spectrum of a 1 mM solution of (Cp)**Co**(Cp^N) in a 2-methyltetrahydrofuran glass at 77 K. (orange) Spectral simulation using EasySpin(*51*) with the following parameters: g = [1.8669, 1.8654, 1.5172], linewidth = 61.42 Hz, Hstrain = [0.0965 19.3818 510.669] Hz.

Sample Preparation for [(Cp)Co(Cp^{NH})][OTf]:

Protonation: In a glovebox cold well, a 2 mM solution of (Cp)**Co**(Cp^N) in 2-methyltetrahydrofuran (0.5 mL) was layered on a frozen solution of 2-chloroanilinium triflate in 2-methyltetrahydrofuran (2 mM, 0.5 mL). The layers were briefly allowed to thaw and agitated with a pre-chilled spatula. The solution turned a dark blue color. It was then rapidly transferred with a prechilled pipette to an X-band EPR tube. The solution was then frozen, brought out of the glovebox, and analyzed by continuous wave X-band EPR at 77 K.

Reduction: In a glovebox cold well, a 2 mM solution of [(Cp)**Co**(Cp^{NH})][OTf]$_2$ in acetonitrile (0.5 mL) was added to a vial. This was frozen and on this was layered a 2 mM solution of SmI_2 in acetonitrile (0.5 mL). The layers were thawed and quickly mechanically mixed with a pre-chilled spatula. The solution turned a dark blue color and then transferred with a pre-chilled pipette to an X-band EPR tube. The solution was then frozen, brought out of the glovebox, and analyzed by continuous wave X-band EPR.

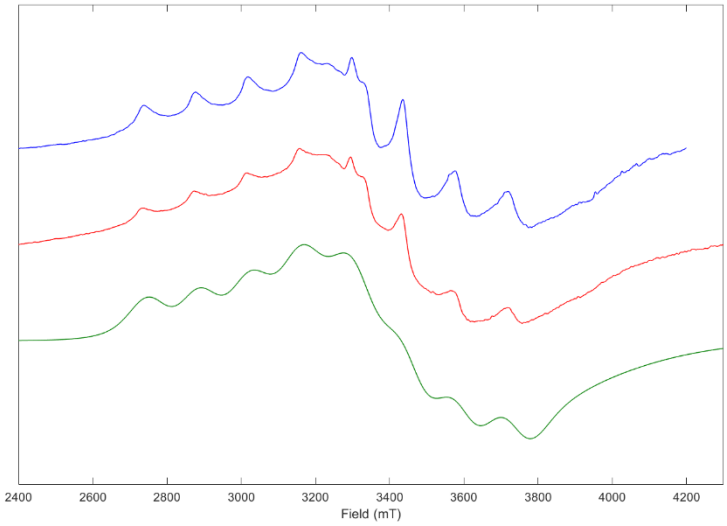

Fig. S15. (blue) X-band EPR spectrum of a 1 mM solution of [(Cp)**Co**(Cp^{NH})][OTf] in a 2-methyltetrahydrofuran glass at 77 K generated via protonation of (Cp)**Co**(Cp^{N}). (red) X-band EPR spectrum of a 1 mM solution of [(Cp)**Co**(Cp^{NH})][OTf] in frozen acetonitrile at 77 K generated via reduction of [(Cp)**Co**(Cp^{NH})][OTf]$_2$. (green) Simulation of these data with EasySpin.(*51*) g = [2.0555, 1.9932, 1.7959]; A(^{59}Co) = [401.1050, 27.8926, 41.6297] Hz; HStrain = [220.0820, 656.3320, 1885.5] Hz; gStrain=[0.0307, 0.0305, 0.0342]

The high degree of strain in the simulation is suggestive of a variety of conformations or hydrogen bonding interactions, or poor homogeneity of the solution. The broadness of (Cp)**Co**(Cp^{N}) in 2Me-THF glass supports the possibility of the variety of conformations. Indeed the g-values of many cobaltocenes display high sensitivity to their local environment.(*52–54*) The increased broadness of the acetonitrile sample relative to the 2-MeTHF sample provides support for the source of broadness being heterogeneity.

S.6. IR Spectroscopy:

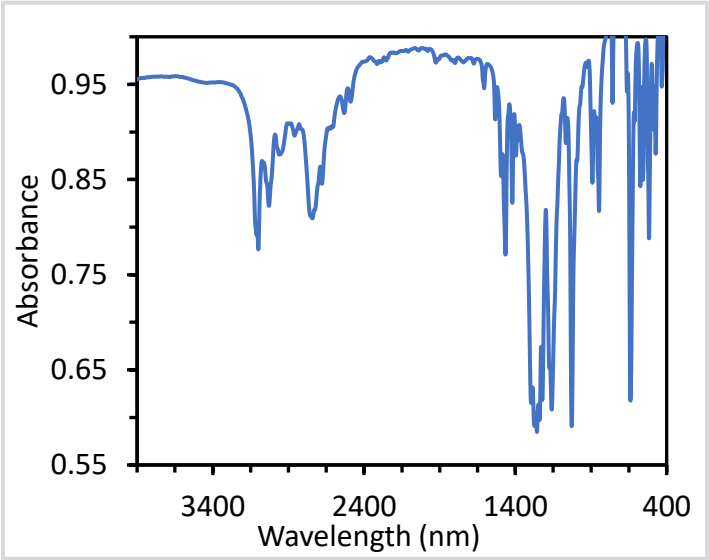

Fig. S16. IR spectrum of [(Cp)**Co**(Cp^{NH})][OTf]$_2$ in a KBr pellet. The N−H vibration is evident as the weak mode at 3430 cm^{-1}.

S.7. X-ray Crystallography:

Table S1. Crystallographic data for complexes (Cp)**Co**(Cp^N), [(Cp)**Co**(Cp^{NH})][OTf]$_2$ and [(Cp)**Co**(Cp^N)][OTf].

Compound	(Cp)**Co**(Cp^N)	[(Cp)**Co**(Cp^{NH})][OTf]$_2$	[(Cp)**Co**(Cp^N)][OTf]
Chemical Formula	$C_{18}H_{19}CoN$	$C_{20}H_{20}CoNF_6O_6S_2$	$C_{19}H_{19}CoNF_3O_3S$
Formula Weight	308.27	607.42	457.34
Crystal System	Triclinic	Triclinic	Triclinic
Space Group	P −1	P −1	P −1
a (Å)	13.3390(15)	8.2326(5)	10.5419(7)
b (Å)	10.8922(13)	12.5729(7)	11.6519(8)
c (Å)	9.6039(11)	12.9491(8)	16.4972(10)
α (°)	90	67.614(3)	89.708(2)
β (°)	90	76.729(3)	79.981(2)
γ (°)	90	81.730(3)	67.013(2)
V (Å^3)	1395.4(3)	1203.85(13)	1832.6(2)
Z	4	2	4
D_{calcd} (g·cm^{-1})	9.518	1.676	1.658
F_{000}	644.0	616.0	936.0
μ (mm^{-1})	9.518	7.997	1.101
Temperature (K)	100(2)	100(2)	100(2)
Wavelength (Å)	0.71073	1.54178	
Measured Reflections	1457	4716	12299
Unique Reflections	1314	4491	10976
Data/Restraints/Parameters	1457/0/509	4716/0/327	10976/0/509
R(F) (I>2σ(I))	0.0543	0.0411	0.0297
wR(F^2) (all)	0.1400	0.0970	0.0793
GOOF	1.068	1.046	1.033

S8 Kinetic analysis:

S8.1 General Introduction:

The kinetic analyses in these papers are done within frameworks developed by Savéant and coworkers.(*26*, *55*) These frameworks allow one to use the plateau current observed during an ideal S-shaped catalytic process (i_{cat}) to extract mathematical information about the observed reaction rate (k_{obs}). In this plateau current regime, the reaction is only limited by chemical steps performed by the catalyst and thus this k_{obs} can be related to the catalytic rate (k_{cat}) by assuming a mechanism. Herein, we are evaluating i_{cat} as the maximum current of the electrocatalytic wave.

S8.2 Kinetic Analysis of HER by $[Cp_2Co]^+$:

Based on our study of HER by $[Cp_2Co]^+$, we propose that it occurs via an ECEC mechanism (**Fig. S17**), in which E_1 is the reduction of $[Cp_2Co]^+$ to Cp_2Co; C_1 is the protonation of Cp_2Co to form $[(Cp)\mathbf{Co}(\eta^4\text{-}C_5H_6)]^+$; E_2 is the reduction of $[(Cp)\mathbf{Co}(\eta^4\text{-}C_5H_6)]^+$ to $(Cp)\mathbf{Co}(\eta^4\text{-}C_5H_6)$; C_2 is the protonation of $(Cp)\mathbf{Co}(\eta^4\text{-}C_5H_6)$ to release H_2 and reform $[Cp_2Co]^+$. E_2 (−0.33 V vs $Fc^{+/0}$) is easier than E_1 (−1.33 V vs $Fc^{+/0}$). Also, we have established that Cp_2Co builds up during HER (**Fig. S22**), so the first chemical step must be much slower than the second. In such cases, the plateau current of the catalytic process is described by **Eq. S2**, in which F is Faraday's constant, S is the surface area of the electrode, C^0_{cat} is the catalyst concentration, D_{cat} is the diffusion coefficient of the catalyst, k_1 is the rate of C_1, and C^0_A is the concentration of the acid. This can be converted to a maximum turnover frequency (TOF_{max}) by **Eq. S3**.(*55*) The Randles-Sevcik equation (**Eq. S4**), in which n' is the number of electrons transferred in the absence of catalysis, ν is the scan rate, R is the gas constant, and T is the temperature, can be used to ascertain D_{cat} ($4\cdot10^{-10}$ $m^2\cdot s^{-1}$) from CVs performed at different scan rates in the absence of acid. By measuring i_{cat}, in the presence of acid (**Fig. S24**), we can use **Eq. S3** and **S4** to determine a value for k_1 of 0.60 $M^{-1}\cdot s^{-1}$ and a TOF_{max} of 0.06 s^{-1} for HER by $[Cp_2Co]^+$.

$$i_{cat} = 2FSC^0_{cat}\sqrt{D_{cat}k_1C^0_A} \qquad \textbf{Eq. S2}$$

$$TOF_{max} = k_1C^0_A \qquad \textbf{Eq. S3}$$

$$i_p = 0.4463n'FSC^0_{cat}\sqrt{\frac{n\prime D_{cat}F\nu}{RT}} \qquad \textbf{Eq. S4}$$

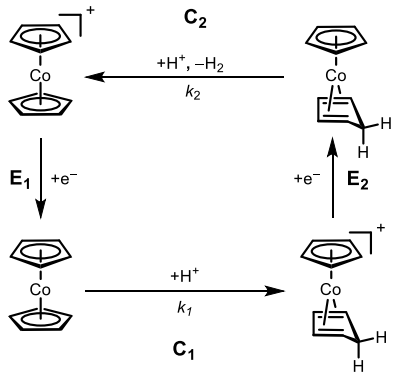

Fig. S17: Mechanism for catalytic HER by $[Cp_2Co]^+$.

S8.3 Kinetic Analysis of CPET by $[(Cp)Co(Cp^{NH})]^+$:

The mechanism for the electrocatalytic CPET reaction is shown in **Fig. S18**. Within the framework of Savéant and coworkers this is described as an EC_{cat} mechanism, meaning that there is one reduction step followed by subsequent chemical steps.(*26*) Such reactions are modelled by **Eq. S5**. As there are two chemical steps, in the CPET reaction between $[(Cp)\mathbf{Co}(Cp^{NH})]^+$ and acetophenone to form the neutral radical and $[(Cp)\mathbf{Co}(Cp^{N})]^+$, and subsequent protonation of $[(Cp)\mathbf{Co}(Cp^{N})]^+$ by the acid to reform $[(Cp)\mathbf{Co}(Cp^{NH})]^{2+}$, k_{obs} represents a convolution of the rate of these two steps.

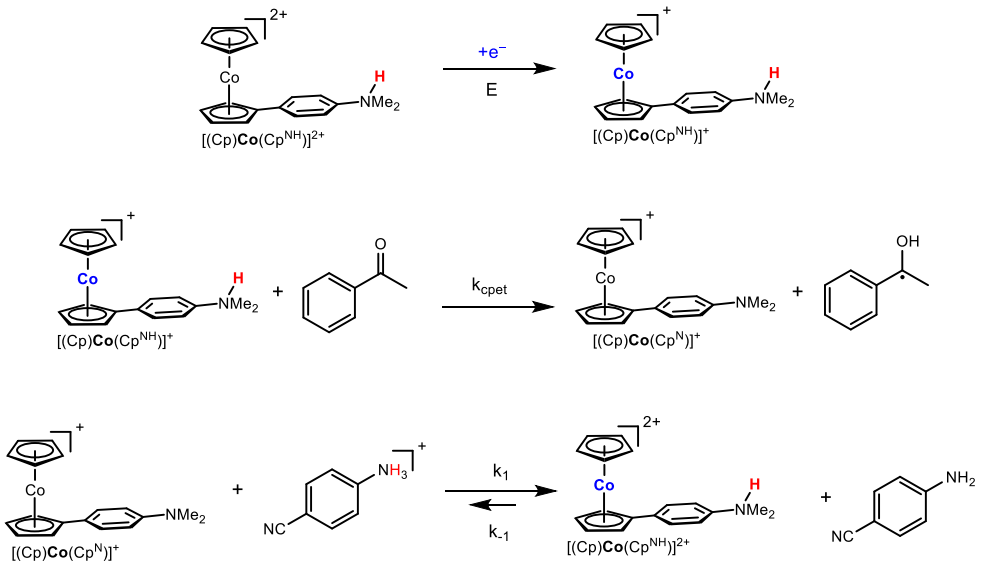

Fig. S18. EC_{cat} mechanism describing the electrocatalytic CPET reaction.

However, because we observe that the reaction rate is not affected by acid concentration, we can safely assume that protonation is much faster than CPET. Thus, by using **Eq. S6**, k_{obs} can be used to determine the rate of CPET (k_{CPET}) by accounting for the concentration (of acetophenone (C^0_K). Substituting **Eq. S6** into **Eq. S5** and normalizing by **Eq. S4** again results in **Eq. S7**, which makes evident that a first order dependence on acetophenone in the chemical step results in a half-order dependence of i_{cat} on acetophenone. From this S-shape analysis, we obtain a k_{CPET} of 4.6 $M^{-1}\cdot s^{-1}$. The same method of analysis has been applied to the other ketone substrates in this study.

$$i_{cat} = 2FSC^0_{cat}\sqrt{D_{cat}k_{obs}} \qquad \textbf{Eq. S5}$$

$$k_{obs} = k_{CPET}C^0_K \qquad \textbf{Eq. S6}$$

$$\frac{i_{cat}}{i_p{}^0} = 2.24\sqrt{\frac{RT}{Fv}k_{CPET}C^0_K} \qquad \textbf{Eq. S7}$$

Savéant and coworkers have also suggested that in cases with non-ideal catalytic responses, an alternative approach, termed foot-of-the-wave analysis (FOWA), may be more suitable for extracting kinetic information.(*26*) By looking at the current variation at the beginning of the

catalytic process there is less time for deviations from ideal behavior (*e.g.*, substrate consumption, catalyst decomposition, etc.) to effect the rate analysis. The FOWA is encapsulated by **Eq. S8**, in which i_c is the current at a given potential E under the catalytic conditions and i_p is the current at the same potential E under non-catalytic conditions. The $E_{cat/2}$ is the potential at which half of the maximum catalytic current is achieved.(*26*)

$$\frac{i_c}{i_p^0} = \frac{2.24\sqrt{\frac{RT}{Fv}k_{CPET}C_K^0}}{1+\exp\left[\frac{F}{RT}(E-E_{cat/2})\right]} \qquad \textbf{Eq. S8}$$

Determining k_{PCET} in this way results in a value of 5.7 $M^{-1}\cdot s^{-1}$, very similar to what we observed using the more straightforward S-shape analysis (4.6 $M^{-1}\cdot s^{-1}$). This suggests that the catalytic system is well-behaved and that, under the conditions used, the catalysis is close to the pure kinetic regime. Thus, for simplicity, we have used the more straightforward S-shape analysis for the values presented in the main text. Nonetheless, analysis of the data with the more general FOWA does not alter any of the conclusions presented.

This rate can also be evaluated in terms of a TOF_{max} for better comparison with other reactions that differ in their rate law. This is done with **Eq. S9** and yields a TOF_{max} of 0.46 s^{-1}.

$$TOF_{max} = k_{\text{obs}} = k_{\text{CPET}}[C_K^0] \qquad \textbf{Eq. S9}$$

Lastly, the kinetic isotope effect, *KIE*, was determined by evaluating k_{CPET} for the reaction in the presence of protio-acid, $[^{4\text{-CN}}PhNH_3]^+$, and deutero-acid, $[^{4\text{-CN}}PhND_3]^+$, and comparing them as described in **Eq. S10**.

$$KIE = \frac{k_{CPET}\,(^1H)}{k_{CPET}\,(^2H)} \qquad \textbf{Eq. S10}$$

S8.4 Kinetic Analysis of HER by $[(Cp)Co(Cp^{NH})]^+$:

In the case of [(Cp)**Co**(Cp^N)][OTf], we propose that HER proceeds via a homolytic mechanism that involves coupling of two $[(Cp)\mathbf{Co}(Cp^{NH})]^+$ (**Fig. S19**), because subsequent protonation or reduction steps are unfavorable, making a hetero-coupling mechanism (*e.g.*, ECEC) unfavorable. As HER by $[(Cp)\mathbf{Co}(Cp^N)]^+$ is very slow, it was necessary to perform a CV at a very low scan rate (5 $mV\cdot s^{-1}$) in order to observe even partial catalytic behavior at the wave associated with reduction of $[(Cp)\mathbf{Co}(Cp^{NH})]^{2+}$ to $[(Cp)\mathbf{Co}(Cp^{NH})]^+$. At this scan rate, the reduction wave in the presence of acid is more irreversible and more intense than in the absence of acid, indicative of slow HER. This situation has been well-described by Savéant and coworkers as the KD regime (slow kinetic and no substrate consumption), and the plateau current can therefore be used to extract kinetic information about the HER process. For a homolytic mechanism, the plateau current is described by **Eq. S11**.(*55*)

$$i_{cat} = FS\sqrt{\frac{4D_{cat}k_d}{3}}\left(\frac{k_1C_A^0}{k_{-1}}\right)\frac{{C_{cat}^0}^{3/2}}{\left(1+\frac{k_1C_A^0}{k_{-1}}\right)^{3/2}} \qquad \textbf{Eq. S11}$$

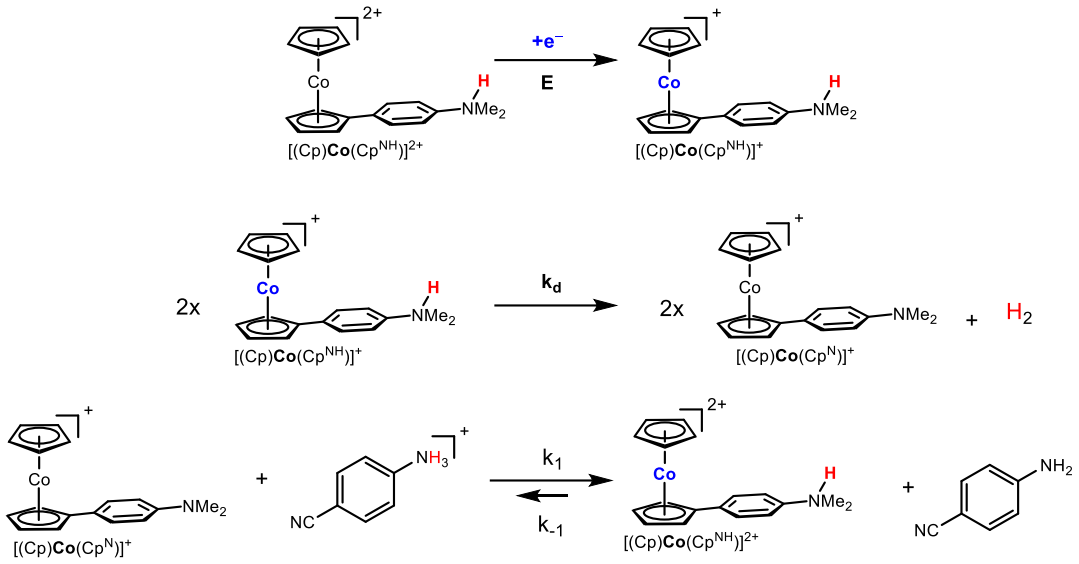

Fig. S19. Proposed homolytic mechanism for HER by [(Cp)**Co**(Cp^{NH})]$^+$.

In our mechanism the term k_1/k_{-1} can be rewritten as the equilibrium constant of the protonation step (K_1, **Eq. S12**), which can be evaluated from the known pK_a values of the [(Cp)**Co**(Cp^{NH})]$^{2+}$ and the [$^{4\text{-CN}}$PhNH$_3$]$^+$ acid. Plugging **Eq. S12** into **Eq. S11** allows us to generate **Eq. S13**. The value of D_{cat} ($5\cdot10^{-10}$ $m^2\cdot s^{-1}$) can again be determined from the Randles-Sevcik equation (**Eq. S4**). In this way, we can obtain a kinetic constant for the dimerization process (k_d) of 0.46 $M^{-1}\cdot s^{-1}$. Using this value and the catalyst concentration (1 mM), we can use **Eq. S14** to assess the TOF_{max} for HER by [(Cp)**Co**(Cp^{NH})]$^+$ to be 0.0004 s^{-1}.

$$K_1 = \frac{k_1}{k_{-1}} = 10^{-\mathrm{p}K_a} \quad \textbf{Eq. S12}$$

$$i_{cat} = FS\sqrt{\frac{4D_{cat}k_d}{3}}\,(K_1C_A^0)\frac{{C_{cat}^0}^{3/2}}{(1+K_1C_A^0)^{3/2}} \quad \textbf{Eq. S13}$$

$$TOF_{max} = \frac{4}{3}k_d\,C_{cat}\left(\frac{\frac{k_1C_A^0}{k_{-1}}}{1+\frac{k_1C_A^0}{k_{-1}}}\right) \quad \textbf{Eq. S14}$$

S8.5 Comparison of Kinetic Data:

HER by [(Cp)**Co**(Cp^{N})]$^+$ (0.0004 s^{-1}) is two order of magnitude slower than by [Cp_2Co]$^+$ (0.06 s^{-1}). Furthermore, it is three orders of magnitude slower than CPET by [(Cp)**Co**(Cp^{NH})]$^+$ (0.46 s^{-1}). These values are consistent with the selectivity observed in the controlled potential coulometry (CPC) results, but it is important to underscore that side reactions, changes in the solution and electrode over time, and diffusion can be notably different under CPC conditions.

S8.6 Error analysis:

Much of the analysis of the electrochemical data involves generating lines of best fit and then interpreting the slope (m) of those lines in order to extract kinetic information. Lines of best fit were generated using Excel and the LINEST function was used to determine the error in their slopes (m_{err}). That error was then propagated to generate the error in k_{cat} (k_{err}) as shown here in **Eq. S15**.

$$k_{err} = \left(2\frac{m \times m_{err}}{2.24}\right)\frac{F}{RTC_K^0} \qquad \textbf{(Eq. S15)}$$

For the KIE, the error (KIE_{err}) was determined as shown in **Eq. S16**.

$$KIE_{err} = KIE\sqrt{\left[\left(\frac{k_{err}(\,^1H)}{k_{cat}(\,^1H)}\right)^2\left(\frac{k_{err}(\,^2H)}{k_{cat}(\,^2H)}\right)^2\right]} \qquad \textbf{(Eq. S16)}$$

S9. Cyclic Voltammetry

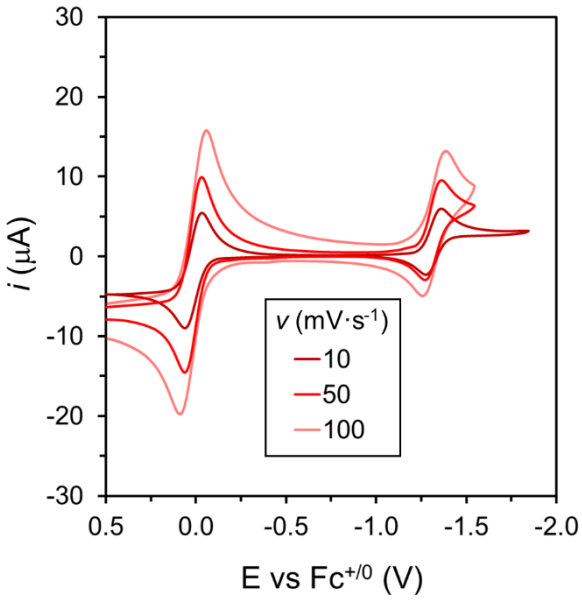

Fig. S20. Variable scan rate CVs of a solution containing 1 mM $[Cp_2Co][OTf]$ and 1 mM ferrocene in DME with 0.1 M $[TBA][PF_6]$ at different scan rates.

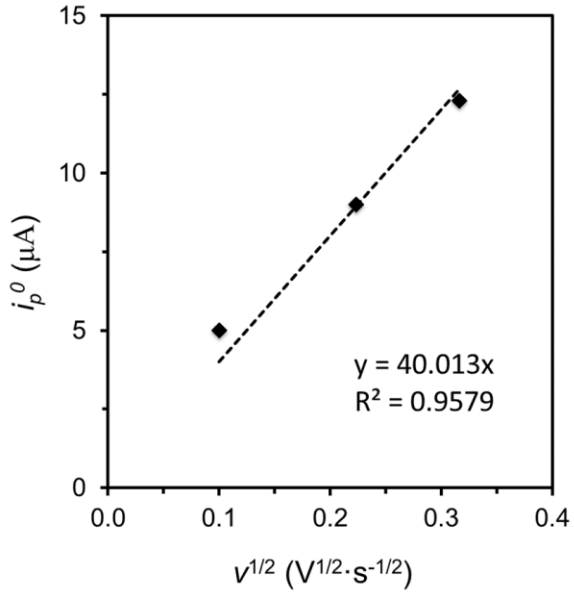

Fig. S21. Plot of the peak current of the redox wave associated to the reduction of $[Cp_2Co]^{+/0}$ from CVs of a solution containing 1 mM $[Cp_2Co][OTf]$ and 1 mM ferrocene in DME with 0.1 M $[TBA][PF_6]$ versus the square root of the scan rate in the presence of 100 equiv of $[^{4\text{-CN}}PhNH_3]^+$. The linear character of the relationship observed indicates the reversible character of this one-electron wave. From the slope of this plot, a diffusion coefficient $D_{cat} = 4 \cdot 10^{-10}$ $m^2 \cdot s^{-1}$ is obtained using **Eq. S4**.

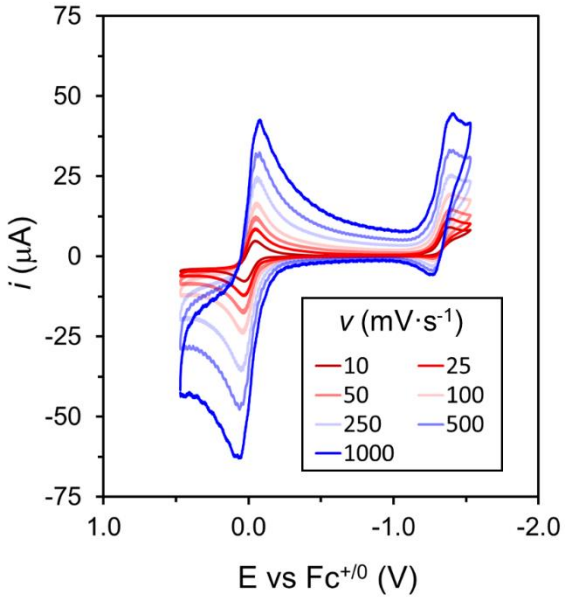

Fig. S22. Variable scan rate CVs of a solution containing 1 mM $[Cp_2Co][OTf]$ and 1 mM ferrocene in DME with 0.1 M $[TBA][PF_6]$ in the presence of 100 mM acid ($[^{4\text{-}CN}PhNH_3][OTf]$). Partial reversibility of the $[Cp_2Co]^{+/0}$ redox couple is observed at scan rates from 250 to 1000 $mV \cdot s^{-1}$.

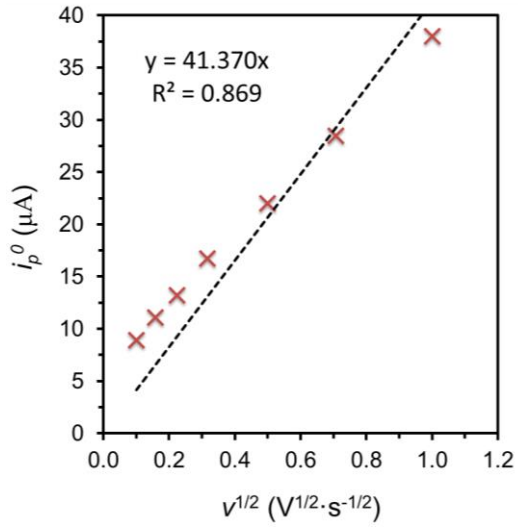

Fig. S23. Plot of the peak current of the redox wave associated with the $[Cp_2Co]^{+/0}$ couple in CV's of a solution containing 1 mM $[Cp_2Co][OTf]$ and 1 mM ferrocene in DME with 0.1 M $[TBA][PF_6]$ in the presence of 100 mM acid ($[^{4\text{-}CN}PhNH_3][OTf]$) against the square root of the scan rate. This relationship should be linear and go through zero (line shown) according to the Randles-Sevcik equation describing an electrochemically reversible electron transfer process for a freely diffusing molecule in solution at an electrode. The deviation from this line indicates the multielectron character of this process consistent with hydrogen evolution catalysis.

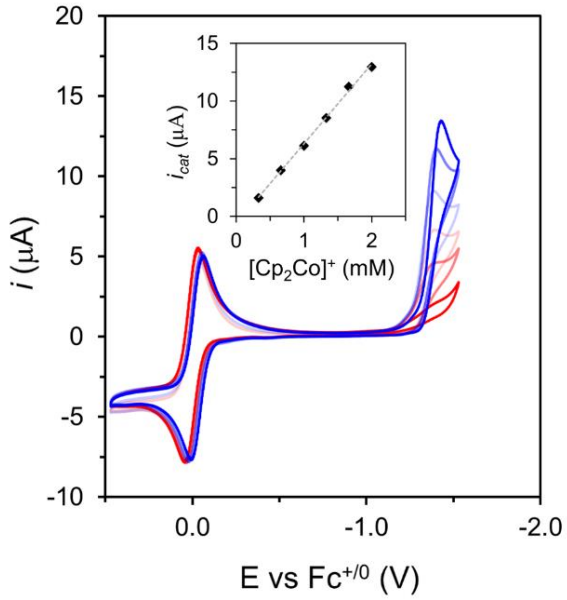

Fig. S24. CVs of a 1 mM solution of ferrocene in DME with 0.1 M [TBA][PF_6] with increasing concentrations of [Cp_2Co][OTf] (0.33-2 mM) in the presence of 100 mM acid ([$^{4\text{-CN}}PhNH_3$][OTf]). These CV's demonstrate the catalytic character of the redox redox process ascribed to HER. Inset shows the plot of the catalytic current versus the concentration of $[Cp_2Co]^+$. The linear relationship is in agreement with a catalytic HER process that is first order in $[Cp_2Co]^+$.

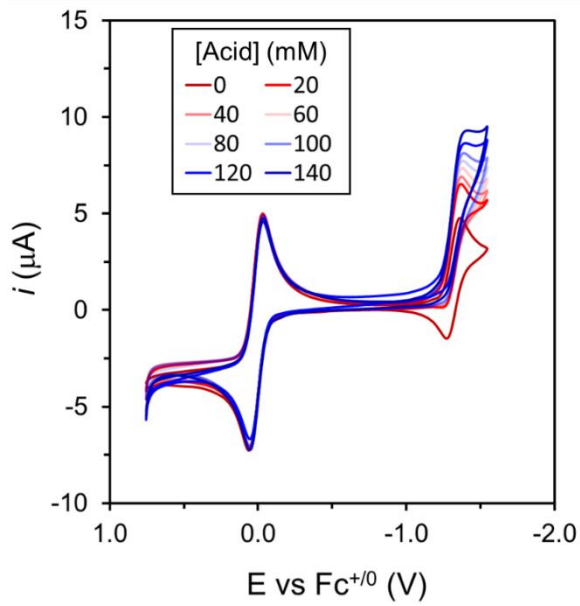

Fig. S25. CVs of a solution containing 1 mM [Cp_2Co][OTf] and 1 mM ferrocene in DME with 0.1 M [TBA][PF_6] and increasing concentrations acid ([$^{4\text{-CN}}PhNH_3$][OTf], 0-140 mM).

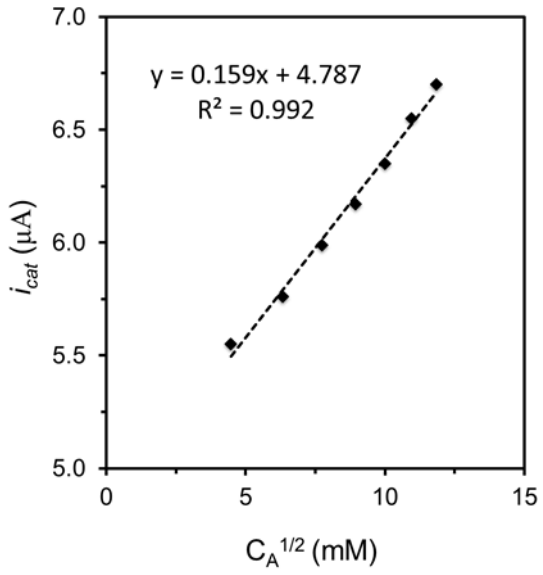

Fig. S26. Plot of the catalytic current (i_{cat}) versus the concentration of acid ([$^{4\text{-CN}}$PhNH$_3$][OTf]) revealing a linear relationship in agreement with a mechanism for catalytic HER that is first order in acid.

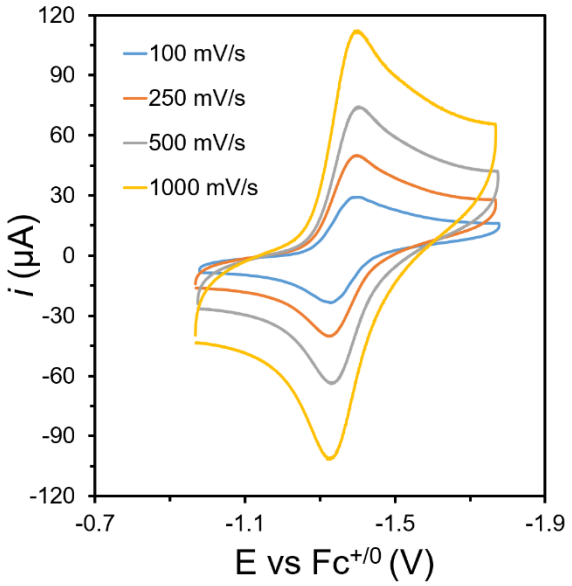

Fig. S27. Variable scan rate CVs with a glassy carbon working electrode of a 1 mM solution of the [(Cp)**Co**(Cp^{N})]$^{+/0}$ in acetonitrile with 0.1 M [TBA][PF$_6$].

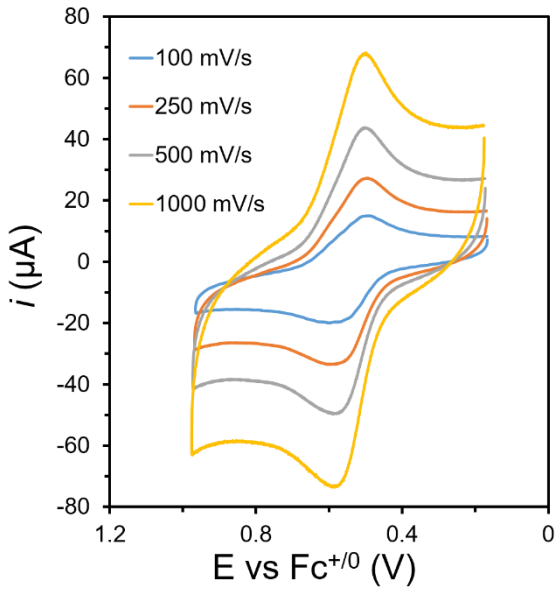

Fig. S28. Variable scan rate CVs with a glassy carbon working electrode of a 1 mM solution of the [(Cp)**Co**(Cp^{N})]$^{2+/+}$ in acetonitrile with 0.1 M [TBA][PF_6].

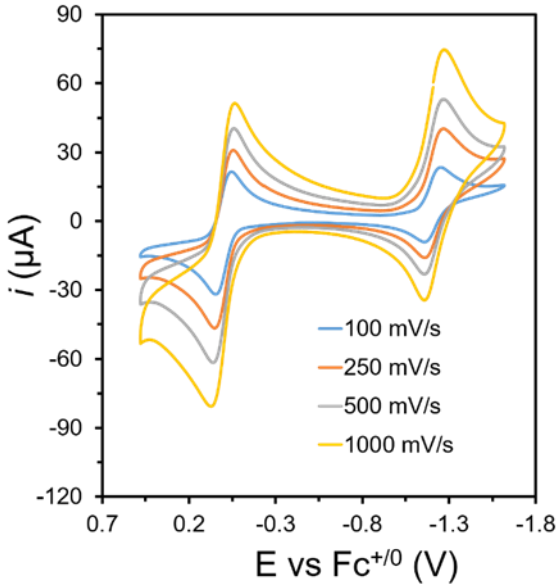

Fig. S29. Variable scan rate CVs with a BDD working electrode of a 1 mM solution of [(Cp)**Co**(Cp^{NH})][OTf]$_2$ and 1 mM solution of ferrocene in acetonitrile with 0.1 M [TBA][PF_6].

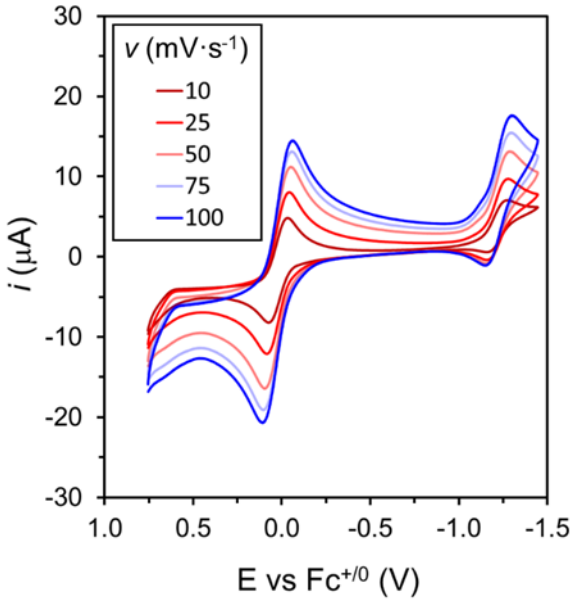

Fig. S30. Variable scan rate CVs of a solution containing 1 mM [(Cp)**Co**(Cp^{N})][OTf] and 1 mM ferrocene in DME with 0.1 M [TBA][PF_6] in the presence of 100 mM acid ([$^{4\text{-CN}}PhNH_3$][OTf]). A highly reversible electron transfer process is observed across the entire range of scan rates, indicating slow reactivity of this species toward HER.

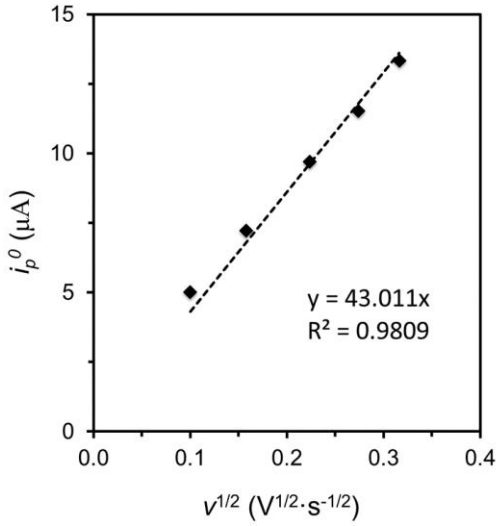

Fig. S31. Plot of the peak current of the redox wave associated to the reduction of [(Cp)**Co**(Cp^{NH})]$^{2+/+}$ from CVs of a solution containing 1 mM [(Cp)**Co**(Cp^{N})][OTf] and 1 mM ferrocene in DME with 0.1 M [TBA][PF_6] in the presence of 100 mM acid versus the square root of the scan rate in the presence of 100 equiv of [$^{4\text{-CN}}PhNH_3$]$^{+}$. According to the Randles-Sevcik Figuation (**Eq. S4**) for an electrochemically reversible electron transfer process of a freely diffusing molecule in solution should be linear. The linear relationship observed indicates the reversible character of this one-electron wave and, thus, slow HER reactivity. From the slope of this plot, a diffusion coefficient $D_{cat} = 5 \cdot 10^{-10}$ $m^2 \cdot s^{-1}$ is obtained using **Eq. S4**.

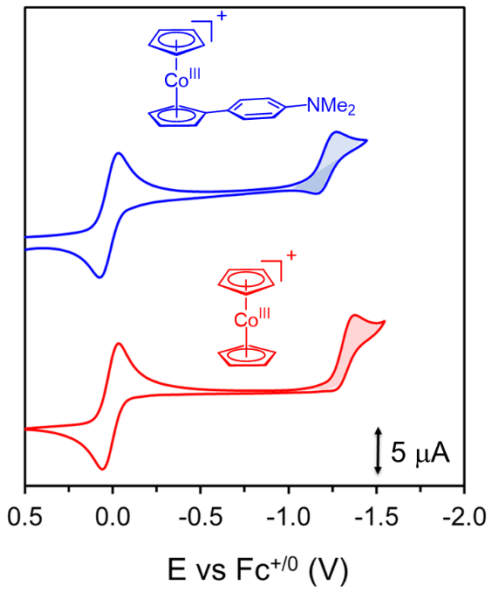

Fig. S32. CVs of a 1 mM solution of either [(Cp)**Co**(Cp^N)][OTf] (blue trace) or [Cp_2Co][OTf] (red trace) with 1 mM ferrocene , 0.1 M [TBA][PF_6], and 0.1M acid ([$^{4\text{-CN}}PhNH_3$][OTf]) at 10 mV·s^{-1} in DME. Comparison reveals the different character of the reduction wave for each cobaltocenium species, being a one-electron reversible reduction for [(Cp)**Co**(Cp^N)]$^+$ (light shading = cathodic, dark shading = anodic) and a catalytic HER wave for [Cp_2Co]$^+$ (only light shading).

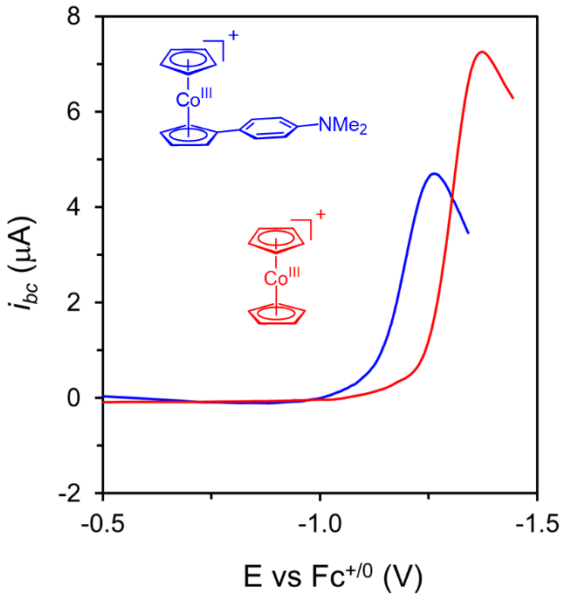

Fig. S33. LSVs of a 1 mM solution of either [(Cp)**Co**(Cp^N)][OTf] (blue trace) or [Cp_2Co][OTf] (red trace) and 1 mM ferrocene in DME with 0.1 M [TBA][PF_6] in the presence of 100 mmM acid ([$^{4\text{-CN}}PhNH_3$][OTf]) at 10 mV·s^{-1}. Comparison of the peak currents reveals the catalytic character of [Cp_2Co] species toward HER.

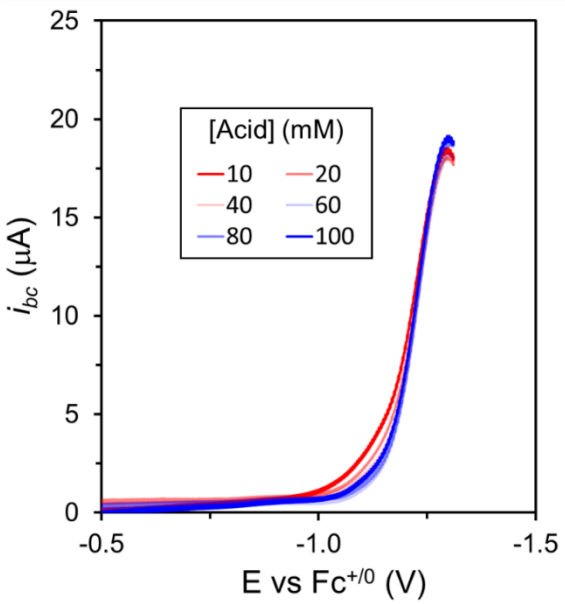

Fig. S34. Background corrected LSVs of a solution containing 1 mM [(Cp)**Co**(Cp^{N})][OTf], 1 mM ferrocene and 50 mM acetophenone in DME with 0.1 M [TBA][PF_6] and increasing concentrations acid ([$^{4\text{-CN}}PhNH_3$][OTf], 0-100 mM). Similar peak currents were obtained for each conditions demonstrating the 0^{th} order of the catalytic reaction in acid.

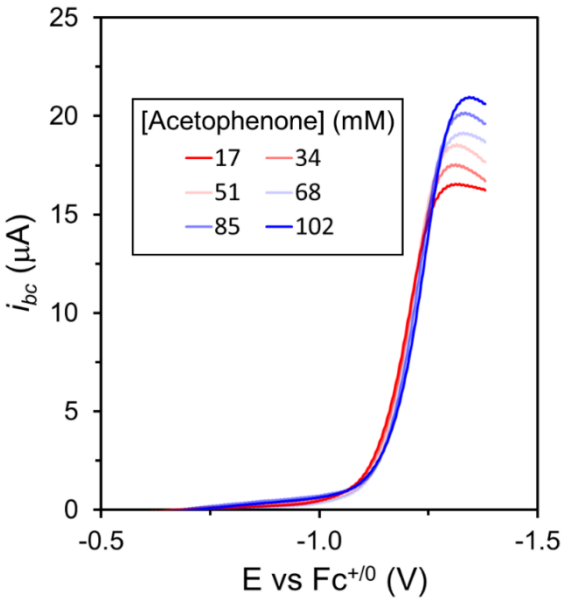

Fig. S35. Background corrected LSVs of a solution containing 1 mM [(Cp)**Co**(Cp^{N})][OTf], 1 mM ferrocene and 100 mM [$^{4\text{-CN}}PhNH_3$][OTf] in DME with 0.1 M [TBA][PF_6] and increasing concentrations of acetophenone (0-102 mM). The continuous and regular increase in the catalytic peak currents demonstrates the 1^{st} order of the catalytic reaction in acetophenone.

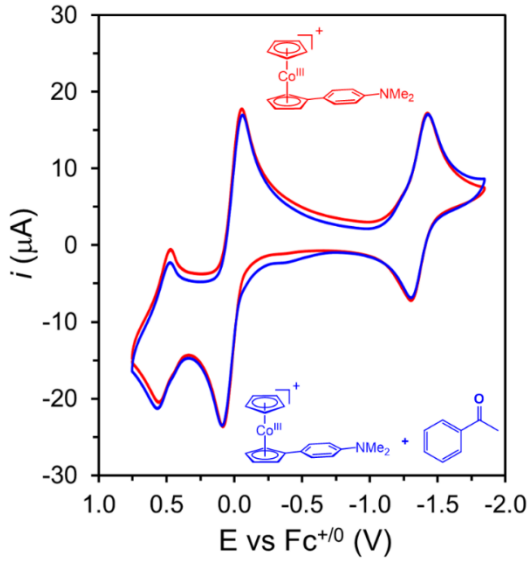

Fig. S36. CVs of a solution containing 1 mM [(Cp)**Co**(Cp^{N})][OTf] and 1 mM ferrocene in DME with 0.1 M [TBA][PF_6] in the presence (blue trace) and absence (red trace) of 50 mM acetophenone at 100 mV·s^{-1}. These CVs demonstrate the lack of reactivity between the reduced (Cp)**Co**(Cp^{N}) and acetophenone, supporting the hypothesis that the reactivity proceeds from [(Cp)**Co**(Cp^{NH})]$^{+}$.

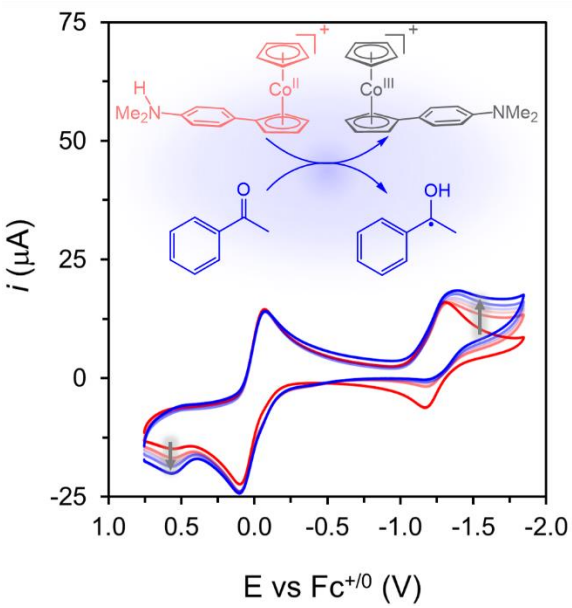

Fig. S37. CVs of a solution containing 1 mM [(Cp)**Co**(Cp^{NH})][OTf] and 1 mM ferrocene in DME with 0.1 M [TBA][PF_6] with increasing concentrations of acetophenone (0-50 mM) at 100 mV·s^{-1}. In the absence of acetophenone (red trace), [(Cp)**Co**(Cp^{NH})][OTf] does not show any reactivity upon reduction consistent with the lack of HER activity. As the acetophenone concentration increases, the couple associated to [(Cp)**Co**(Cp^{NH})]$^{+/0}$ becomes less reversible and the intensity at ~−1.4 V vs $Fc^{+/0}$ increases. These observations are consistent with the loss of [(Cp)**Co**(Cp^{NH})]$^{+}$ and the formation of [(Cp)**Co**(Cp^{N})]$^{+}$, a consequence of the PCET reactivity.

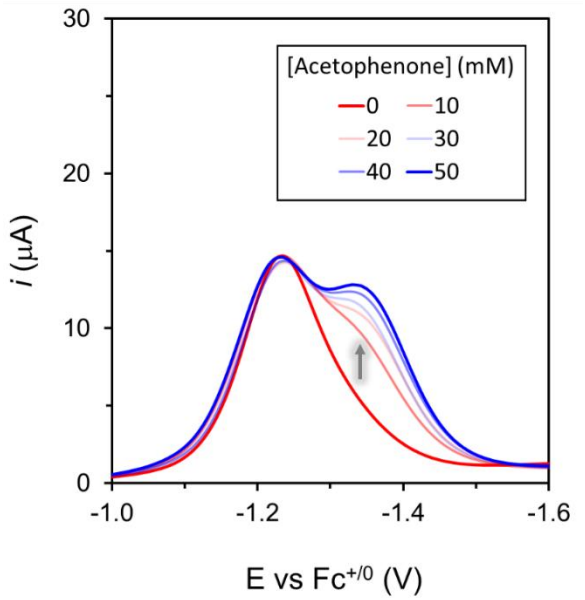

Fig. S38. DPVs of a 1 mM solution of [(Cp)**Co**(Cp^{NH})][OTf] and 1 mM ferrocene (not shown) in DME with 0.1 M [TBA][PF_6] with increasing concentrations of acetophenone (0-50 mM). In the absence of acetophenone (red trace), [(Cp)**Co**(Cp^{NH})][OTf] does not show any reactivity upon reduction consistent with the lack of HER activity. As also seen in **Fig. S37**, as the current intensity at ~−1.4 V increases concomitant with increasing acetophenone concentration. Again, we attribute this increase to the production of $[(Cp)\mathbf{Co}(Cp^{N})]^{+}$ from a PCET reaction between $[(Cp)\mathbf{Co}(Cp^{NH})]^{+}$ generated at the electrode and acetophenone.

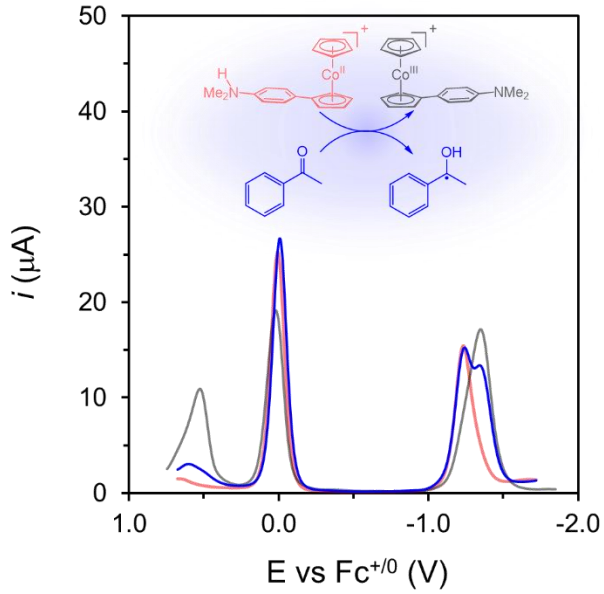

Fig. S39. DPVs of a solution containing 1 mM [(Cp)**Co**(Cp^{NH})][OTf] (red), 1 mM [(Cp)**Co**(Cp^{N})][OTf] (gray), and 1 mM [(Cp)**Co**(Cp^{NH})][OTf] in the presence of 50 mM acetophenone (blue) in DME with 0.1 M [TBA][PF_6].

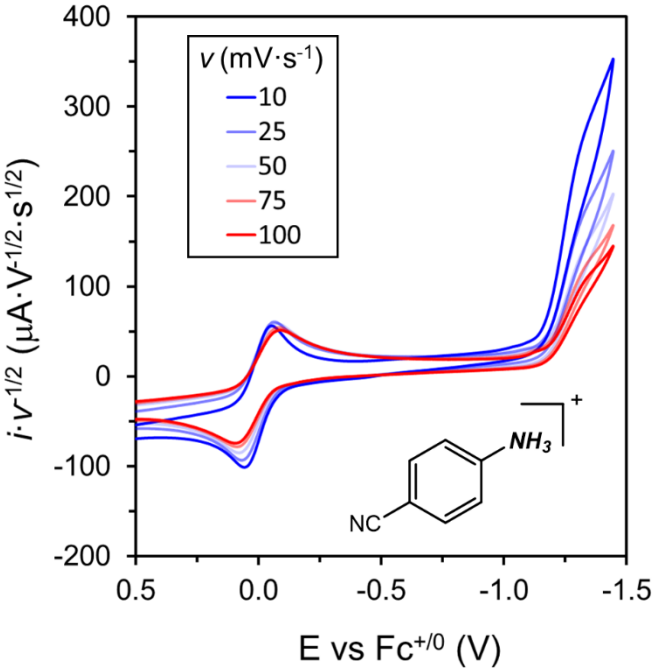

Fig. S40. Variable scan rate CVs of a solution containing 1 mM [(Cp)**Co**(Cp^{N})][OTf], 1 mM ferrocene, 50 mM [$^{4\text{-CN}}PhNH_3$][OTf] and 50 mM acetophenone in DME with 0.1 M [TBA][PF_6].

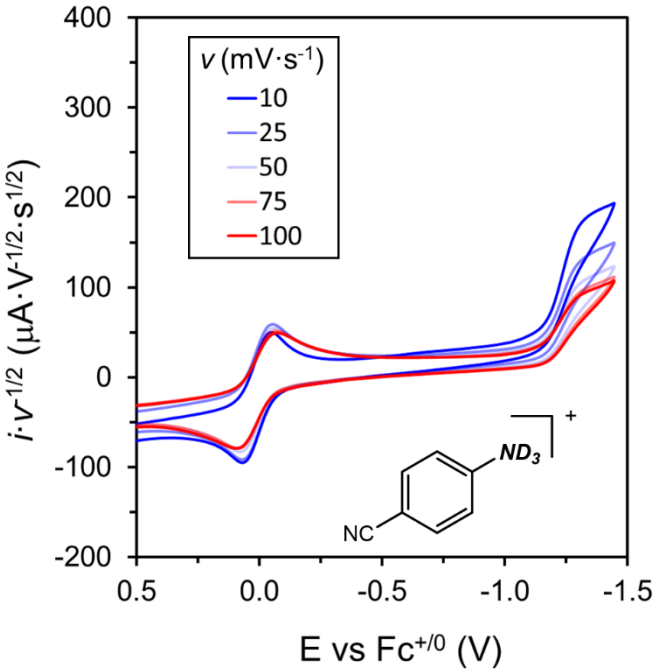

Fig. S41. Variable scan rate CVs of a solution containing 1 mM [(Cp)**Co**(Cp^{N})][OTf], 1 mM ferrocene, 50 mM [$^{4\text{-CN}}PhND_3$][OTf] and 50 mM acetophenone in DME with 0.1 M [TBA][PF_6].

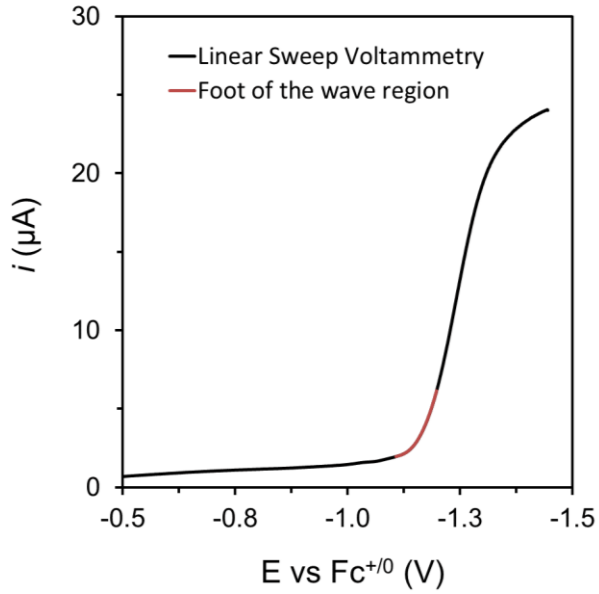

Fig. S42. Background corrected LSV of a solution containing 1 mM [(Cp)**Co**(Cp^N)][OTf], 1 mM ferrocene, 50 mM [$^{4\text{-CN}}$PhND$_3$][OTf] and 50 mM acetophenone in DME with 0.1 M [TBA][PF_6]. The red region corresponds to data of the foot of the catalytic wave used for further kinetic analysis.

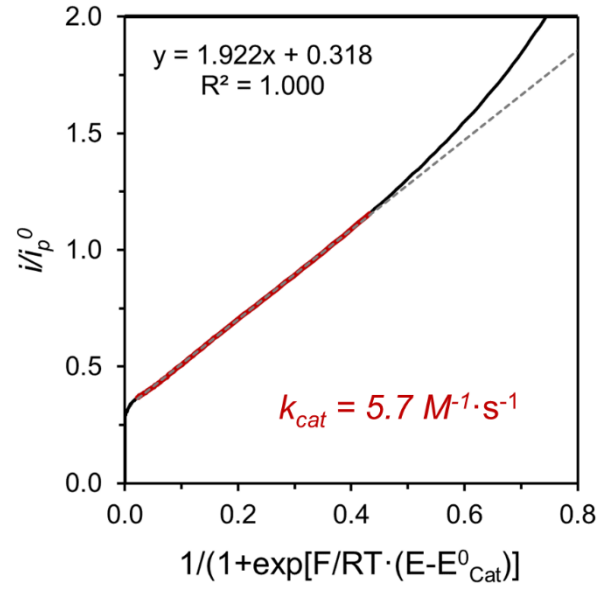

Fig. S43. Plot of i/i_p^0 versus 1/(1+exp[$F/RT\cdot(E-E^0_{Cat}$) according to FOWA for a EC_{cat} mechanism using the data obtained from the LSV shown in **Fig. S42**. The k_{cat} obtained from the slope of the linear fit using the data highlighted in red, is 5.7 $M^{-1}\cdot s^{-1}$, which is in very good agreement with the kinetic constant obtained assuming an ideal S-shaped electrocatalytic response for a system in a pure kinetic regime (4.6 $M^{-1}\cdot s^{-1}$).

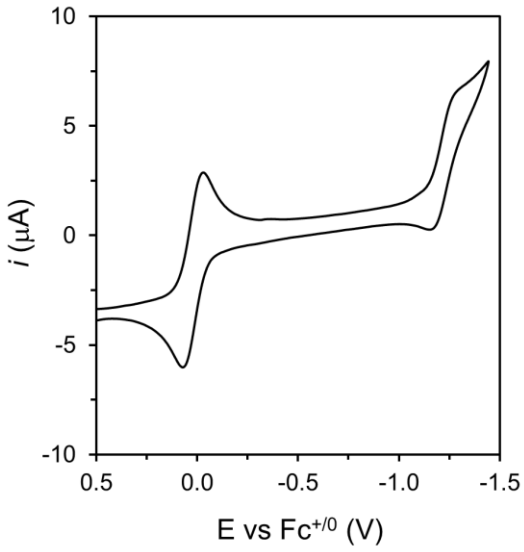

Fig. S44. CV of a 1 mM solution of [(Cp)**Co**(Cp^N)][OTf] with 1 mM ferrocene , 0.1 M [TBA][PF_6], and 0.1M acid ([$^{4\text{-CN}}PhNH_3$][OTf]) at 5 mV·s^{-1} in DME.

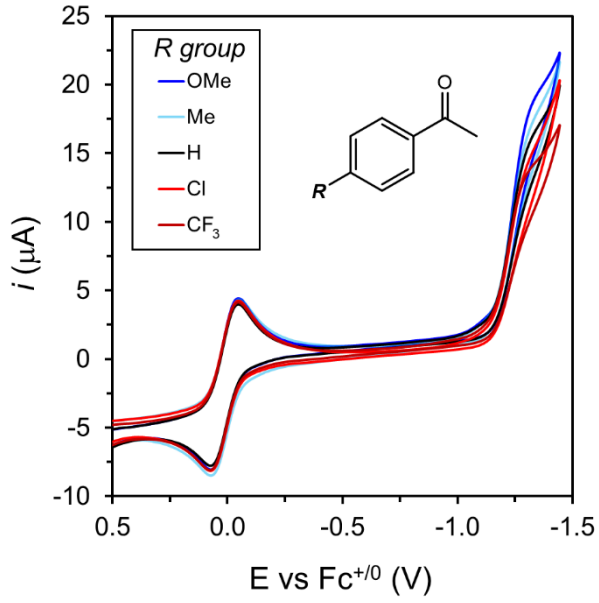

Fig. S45. CVs of a solution containing 1 mM [(Cp)**Co**(Cp^N)][OTf], 1 mM ferrocene and 50 mM [$^{4\text{-CN}}PhNH_3$][OTf] in DME with 0.1 M [TBA][PF_6] in the presence of 50 mM of different *para*-substituted acetophenones ($^{4\text{-R}}$PhC(O)Me R = OMe, Me, H, Cl, CF_3).

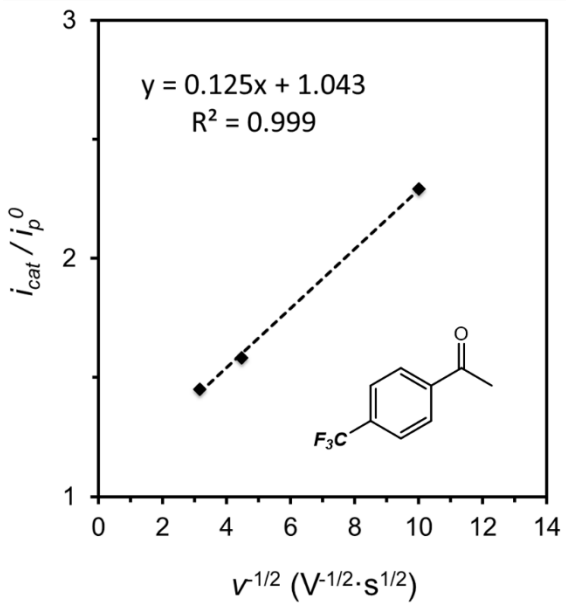

Fig. S46. Plot of i_{cat}/i_p^0 versus $v^{-1/2}$ obtained from the variable scan rate CVs of a solution containing 1 mM [(Cp)**Co**(Cp^N)][OTf], 1 mM ferrocene, 50 mM [$^{4\text{-CN}}$PhNH$_3$][OTf] and 50 mM 4-trifluoromethaneacetophenone ($^{4\text{-CF3}}$PhC(O)Me) in DME with 0.1 M [TBA][PF_6]. Kinetic analysis for an EC_{cat} mechanism assuming an ideal S-shape electrocatalytic response (**Eq. S7**) leads to a kinetic constant of 2.4 $M^{-1} \cdot s^{-1}$.

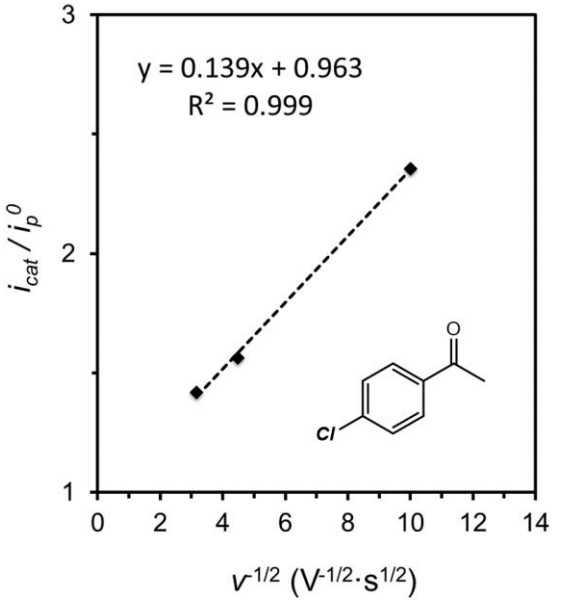

Fig. S47. Plot of i_{cat}/i_p^0 versus $v^{-1/2}$ obtained from the variable scan rate CVs of a solution containing 1 mM [(Cp)**Co**(Cp^N)][OTf], 1 mM ferrocene, 50 mM [$^{4\text{-CN}}$PhNH$_3$][OTf] and 50 mM 4-chloroacetophenone ($^{4\text{-Cl}}$PhC(O)Me) in DME with 0.1 M [TBA][PF_6]. Kinetic analysis for an EC_{cat} mechanism assuming an ideal S-shape electrocatalytic response (**Eq. S7**) leads to a kinetic constant of 3.1 $M^{-1} \cdot s^{-1}$.

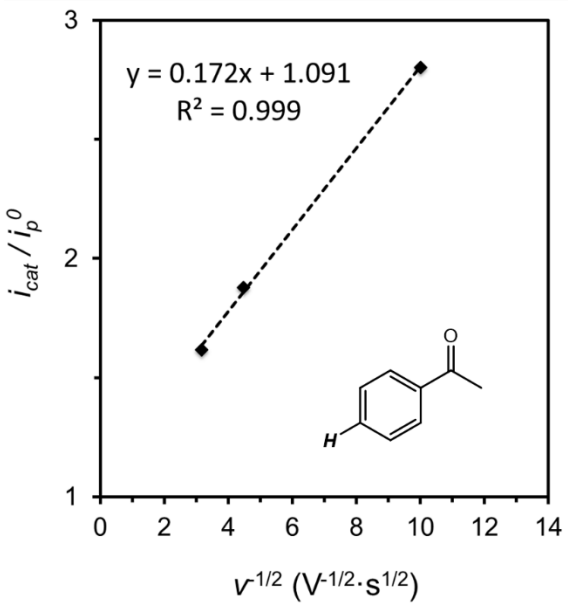

Fig. S48. Plot of i_{cat}/i_p^0 versus $v^{-1/2}$ obtained from the variable scan rate cyclic voltammograms of a solution containing 1 mM [(Cp)**Co**(Cp^N)][OTf], 1 mM ferrocene, 50 mM [$^{4\text{-CN}}PhNH_3$][OTf] and 50 mM acetophenone ($^{4\text{-H}}PhC(O)Me$) in DME with 0.1 M [TBA][PF_6]. Kinetic analysis for an EC_{cat} mechanism assuming an ideal S-shape electrocatalytic response (**Eq. S7**) leads to a kinetic constant of 4.6 $M^{-1} \cdot s^{-1}$.

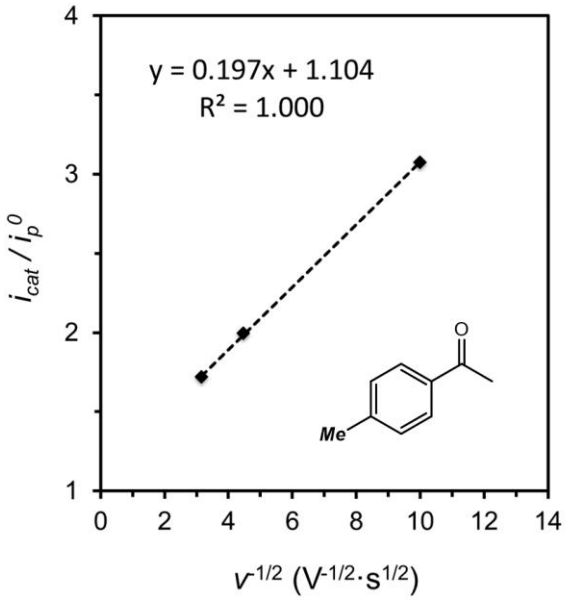

Fig. S49. Plot of i_{cat}/i_p^0 versus $v^{-1/2}$ obtained from the variable scan rate CVs of a solution containing 1 mM [(Cp)**Co**(Cp^N)][OTf], 1 mM ferrocene, 50 mM [$^{4\text{-CN}}PhNH_3$][OTf] and 50 mM 4-methylacetophenone ($^{4\text{-Me}}PhC(O)Me$) in DME with 0.1 M [TBA][PF_6]. Kinetic analysis for an EC_{cat} mechanism assuming an ideal S-shape electrocatalytic response (**Eq. S7**) leads to a kinetic constant of 5.9 $M^{-1} \cdot s^{-1}$.

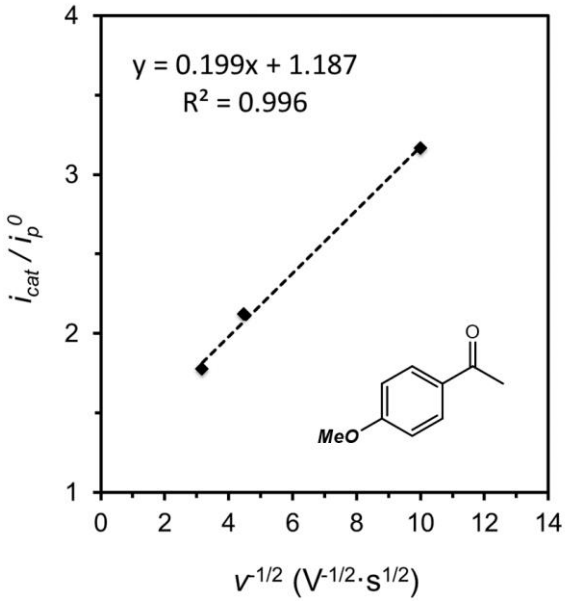

Fig. S50. Plot of i_{cat}/i_p^0 versus $v^{-1/2}$ obtained from the variable scan rate CVs of a solution containing 1 mM [(Cp)**Co**(Cp^N)][OTf], 1 mM ferrocene, 50 mM [$^{4\text{-CN}}$PhNH$_3$][OTf] and 50 mM 4-methoxylacetophenone in DME with 0.1 M [TBA][PF_6]. Kinetic analysis for an EC_{cat} mechanism assuming an ideal S-shape electrocatalytic response (**Eq. S7**) leads to a kinetic constant of 6.1 $M^{-1}·s^{-1}$.

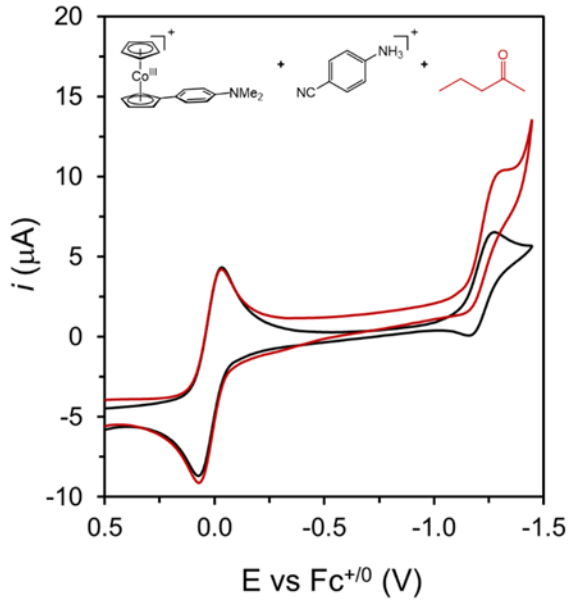

Fig. S51. CVs at 10 mV·s^{-1} of a solution containing 1 mM [(Cp)**Co**(Cp^N)][OTf], 1 mM ferrocene and 50 mM [$^{4\text{-CN}}$PhNH$_3$][OTf] in DME with 0.1 M [TBA][PF_6] (black trace) and after addition of 50 mM 2-pentanone (red trace).

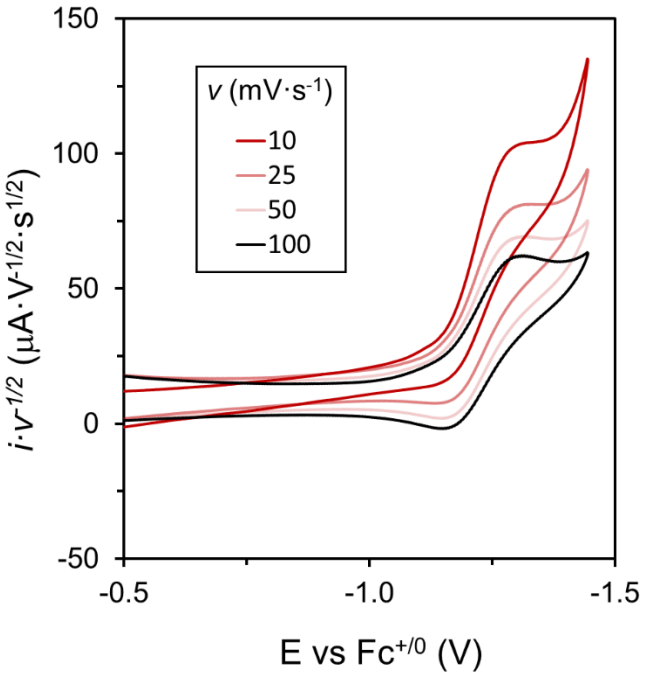

Fig. S52. Current intensity normalized by their scan rate according to the Randles-Sevcik equation from CVs of a solution containing 1 mM [(Cp)**Co**(Cp^N)][OTf], 1 mM ferrocene, 50 mM [$^{4\text{-}CN}PhNH_3$][OTf] and 50 mM 2-pentanone in DME with 0.1 M [TBA][PF_6]. The increased currents after normalization observed at the slower scan rates indicates the presence of a catalytic reaction.

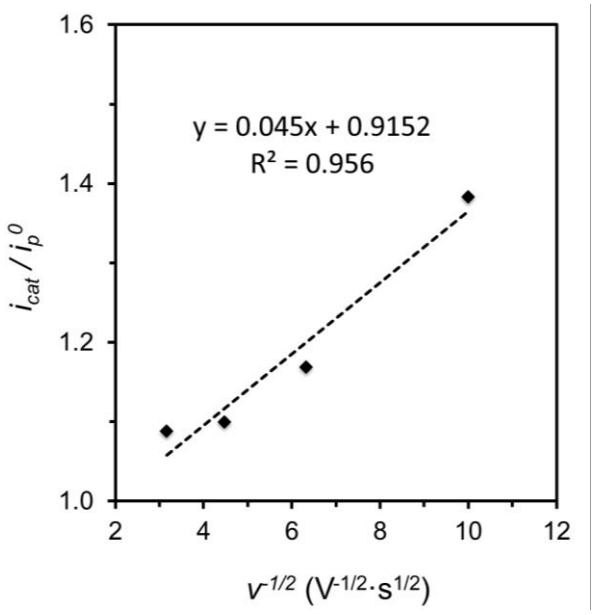

Fig. S53. Plot of i_{cat}/i_p^0 versus $v^{-1/2}$ obtained from the variable scan rate cyclic voltammograms of a solution containing 1 mM [(Cp)**Co**(Cp^N)][OTf], 1 mM ferrocene, 50 mM [$^{4\text{-}CN}PhND_3$][OTf] and 50 mM 2-pentanone in DME with 0.1 M [TBA][PF_6]. Kinetic analysis for an EC_{cat} mechanism assuming an ideal S-shape response allows for a determination of k_{cat} to be 0.31 $M^{-1}\cdot s^{-1}$.

S10. pK_a Determination

Experiments for pK_a determination were performed in MeCN-d_3 using ^{1}H NMR spectroscopy on a 400 MHz spectrometer to determine equilibria constants. In a standard experiment [(Cp)**Co**(Cp^{NH})][OTf]$_2$ was dissolved in MeCN-d_3 and added to a J-Young NMR tube. An initial NMR was taken to verify purity and then aliquots of an aniline base were added to the tube from a stock solution. Although care was taken to add exact amounts of acid (or base) the relative integrals of the species was used to evaluate the amounts of the species rather than an absolute amount as determined by the concentrations/volumes. The relative concentration of the protonated/deprotonated species was determined by the chemical shift of each peak. For each component (*i.e.*, acid/base and [(Cp)**Co**(Cp^{N})][OTf]/[(Cp)**Co**(Cp^{NH})][OTf]$_2$) the average of each of these equilibria were taken. These averages were then used to determine K_{eq} for a given loading of acid/base. These K_{eq} values from each loading were then averaged to give a K_{eq} from each run, which could then be converted to a pK_a based on the known pK_a of the anilinium acids in acetonitrile.

Table S2. NMR shifts of pure compounds used in the pK_a determination experiments.

Compound	[(Cp)**Co**(Cp^{N})][OTf]	[(Cp)**Co**(Cp^{NH})][OTf]$_2$	$^{4\text{-Cl}}$PhNH$_2$	[$^{4\text{-Cl}}$PhNH$_3$][OTf]	$^{2\text{-Cl}}$PhNH$_2$	[$^{2\text{-Cl}}$PhNH$_3$][OTf]
Shift 1	7.61	7.96	7.04	7.53	7.20	7.63
Shift 2	6.78	7.73	6.62	7.42	7.06	7.51
Shift 3	6.08	6.26			6.81	7.49
Shift 4	5.69	5.83			6.63	7.49
Shift 5	5.4	5.54				
Shift 6	3.01	3.29				

Table S3. NMR data for the cobalt complex during a titration of [(Cp)**Co**(Cp^{NH})][OTf]$_2$ with 4-chloroaniline. All chemical shifts are in ppm. In parentheses is the fraction of [(Cp)**Co(**Cp^{NH})][OTf]$_2$ indicated by that chemical shift.

Volume	Shift 1	Shift 2	Shift 3	Shift 4	Shift 5	Shift 6	Average	Std. Dev.
25 µL	7.84 (0.66)	7.42 (0.67	6.19 (0.61)	5.78 (0.64)	5.49 (0.64)	3.2 (0.68)	0.65	0.02
50 µL	7.75 (0.40)	7.17 (0.41)	6.14 (0.33)	5.74 (0.36)	5.45 (0.36)	3.12 (0.39)	0.38	0.03

75 μL	7.70 (0.26)	7.04 (0.27)	6.12 (0.22)	5.72 (0.21)	5.43 (0.21)	3.08 (0.25)	0.24	0.02
100 μL	7.67 (0.17)	6.97 (0.11)	6.10 (0.11)	5.71 (0.14)	5.42 (0.14	3.06 (0.18)	0.16	0.03

Table S4. NMR data for the aniline/anilinium during titration of [(Cp)**Co**(Cp^{NH})][OTf]$_2$ with 4-chloroaniline. Relative integral is determined by setting the most downfield aryl peaks in the cobalt complexes to an integral of 1 and integrating the acid peaks in comparison and taking the average of those integrals.

Volume	Shift 1	Shift 2	Average	Std. Dev.	Relative Integral
25 μL	7.49 (0.92)	7.35 (0.91)	0.92	0.003	0.35
50 μL	7.42 (0.78)	7.23 (0.76)	0.77	0.007	0.77
75 μL	7.34 (0.61)	7.11 (0.61)	0.61	0.0001	1.09
100 μL	7.28 (0.49)	7.01 (0.49)	0.49	0.001	1.54

Table S5. Equilibrium Constants derived from data in Table S3 and Table S4.

Volume	K_{eq}
25 μL	0.17
50 μL	0.18
75 μL	0.20
100 μL	0.19

Table S6. NMR data for the cobalt complex during a second titration of [(Cp)**Co**(Cp^{NH})][OTf]$_2$ with 4-chloroaniline. All chemical shifts are in ppm. In parentheses is the fraction of [(Cp)Co(CpNH)][OTf]$_2$ indicated by that chemical shift.

Volume	Shift 1	Shift 2	Shift 3	Shift 4	Shift 5	Shift 6	Average	Std. Dev.
25 µL	7.85 (0.69)	7.43 (0.68)	6.19 (0.61)	5.78 (0.64)	5.49 (0.64)	3.20 (0.68)	0.66	0.03
100 µL	7.68 (0.2)	6.11 (0.17)	5.72 (0.21)	5.72 (0.21)	5.43 (0.21	3.07 (0.21)	0.21	0.02
125 µL	7.67 (0.17)	6.94 (0.17)	6.10 (0.11)	5.71 (0.14)	5.42 (0.14)	3.06 (0.18)	0.15	0.02

Table S7. NMR data for the aniline/anilinium during a second titration of [(Cp)**Co**(Cp^{NH})][OTf]$_2$ with 4-chloroaniline. Relative integral is determined by setting the most downfield aryl peaks in the cobalt center to an integral of 1 and integrating the acid peaks in comparison and taking the average of those integrals.

Volume	Shift 1	Shift 2	Average	Std. Dev.	Relative Integral
25 µL	7.50 (0.94)	7.35 (0.91)	0.93	0.01	0.37
100 µL	7.33 (0.59)	7.08 (0.58)	0.58	0.01	1.54
125 µL	7.29 (0.51)	7.02 (0.50)	0.51	0.01	1.85

Table S8. Equilibrium Constants derived from data in Table S6 and Table S7.

Volume	K_{eq}
25 µL	0.15
100 µL	0.18
125 µL	0.18

Table S9. NMR data for the cobalt complex during titration of [(Cp)**Co**(Cp^{NH})][OTf]$_2$ with 2-chloroaniline. All chemical shifts are in ppm. In parentheses is the fraction of [(Cp)Co(CpNH)][OTf]$_2$ indicated by that chemical shift.

Volume	Shift 1	Shift 2	Shift 3	Shift 4	Shift 5	Shift 6	Average	Std. Dev.
10 μL	7.90 (0.83)	7.57 (0.83)	6.22 (0.78)	5.81 (0.86)	5.52 (0.86)	3.25 (0.86)	0.83	0.03
20 μL	7.88 (0.77)	7.52 (0.78)	6.21 (0.72)	5.80 (0.79)	5.51 (0.79)	3.23 (0.79)	0.78	0.02
40 μL	7.85 (0.69)	7.44 (0.69)	6.19 (0.61)	5.79 (0.71)	5.49 (0.64)	3.21 (0.71)	0.68	0.04
80 μL	7.81 (0.57)	7.35 (0.60)	6.17 (0.50)	5.77 (0.57)	5.48 (0.57)	3.18 (0.60)	0.57	0.03

Table S10. NMR data for the aniline/anilinium during a titration of [(Cp)**Co**(Cp^{NH})][OTf]$_2$ with 4-chloroaniline. Relative integral is determined by setting the most downfield aryl peak of the Co complex to 1 and then taking the average of the integrals from the acid/base system.

Volume	Shift 1	Shift 2	Shift 3	Shift 4	Average	Std. Dev.	Relative Integral
10 μL	7.33 (0.30)	7.19 (0.29)	7.05 (0.35)	6.91 (0.33)	0.32	0.02	0.28
20 μL	7.30 (0.23)	7.16 (0.22)	7.00 (0.28)	6.85 (0.26)	0.25	0.02	0.51
40 μL	7.27 (0.16)	7.13 (0.16)	6.94 (0.17)	6.78 (0.17)	0.17	0.01	0.90
80 μL	7.25 (0.12)	7.11 (0.11)	6.90 (0.13)	6.73 (0.11)	0.12	0.01	1.62

Table S11. Equilibrium Constants derived from data in Table S9 and Table S10.

Volume	K_{eq}
10 μL	10.9
20 μL	10.3

40 µL	10.2
80 µL	10.3

Table S12. Final equilibrium constants

Experiment #	K_{eq}	Std. Dev.	pK_a
1 ($^{4\text{-Cl}}PhNH_2$)	0.19	0.01 (6%)	8.83
2 ($^{4\text{-Cl}}PhNH_2$)	0.17	0.01 (7%)	8.88
3 ($^{2\text{-Cl}}PhNH_2$)	10.3	0.4 (3%)	8.87

Final pK_a is 8.86 ± 0.02.

S9.1 NMR data of Relevance to pK_a Determination:

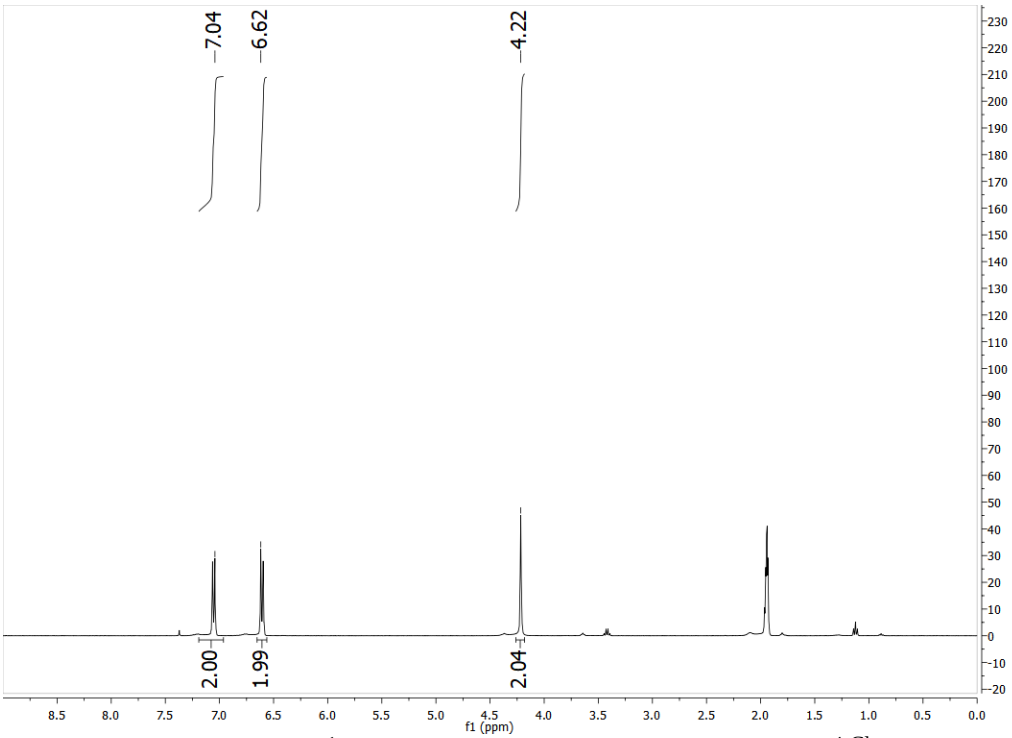

Fig. S54. The 400 MHz ^{1}H NMR spectrum of 4-chloroaniline ($^{4\text{-Cl}}PhNH_2$) in MeCN-d_3 at room temperature.

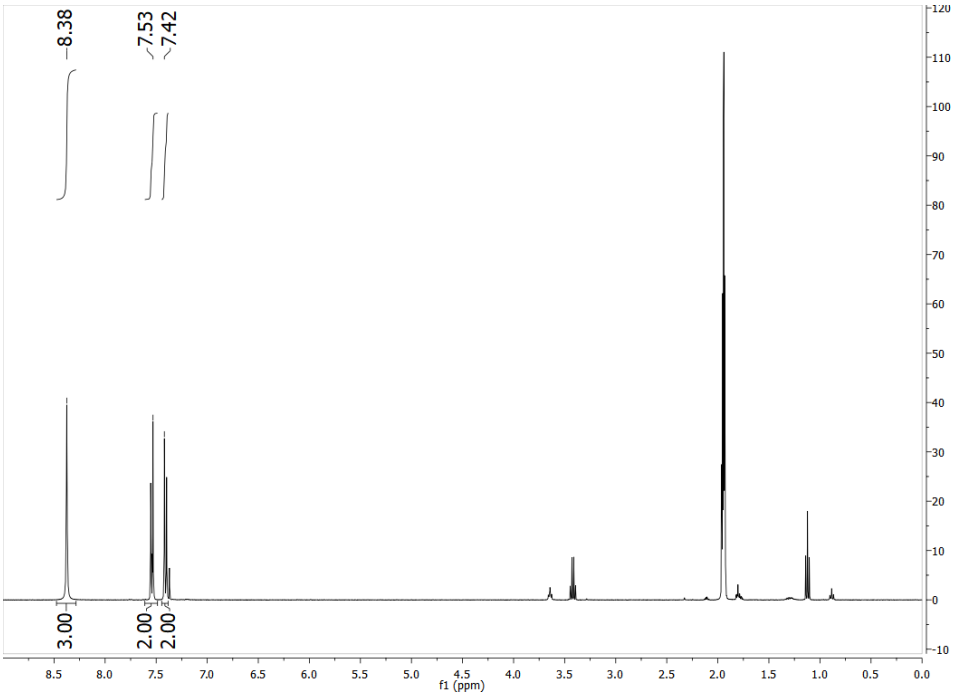

Fig. S55. The 400 MHz ^{1}H NMR spectrum of 4-chloroanilinium triflate ([$^{4\text{-Cl}}$PhNH$_3$][OTf]) in MeCN-d_3 at room temperature.

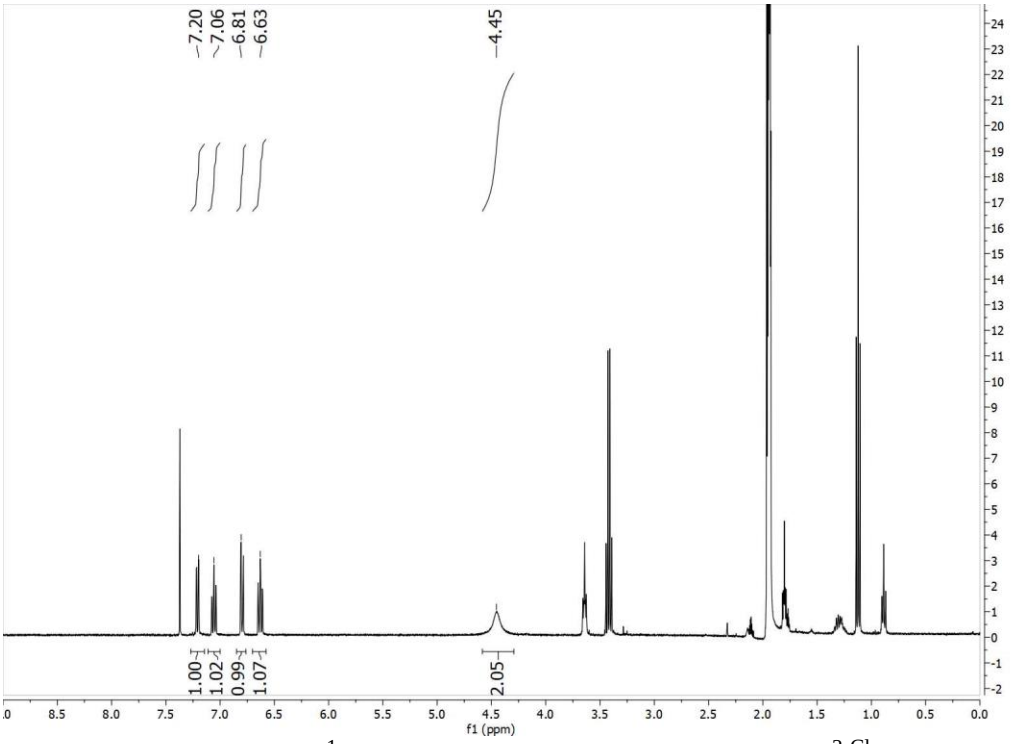

Fig. S56. The 400 MHz ^{1}H NMR spectrum of 2-chloroaniline ($^{2\text{-Cl}}$PhNH$_2$) in MeCN-d_3 at room temperature.

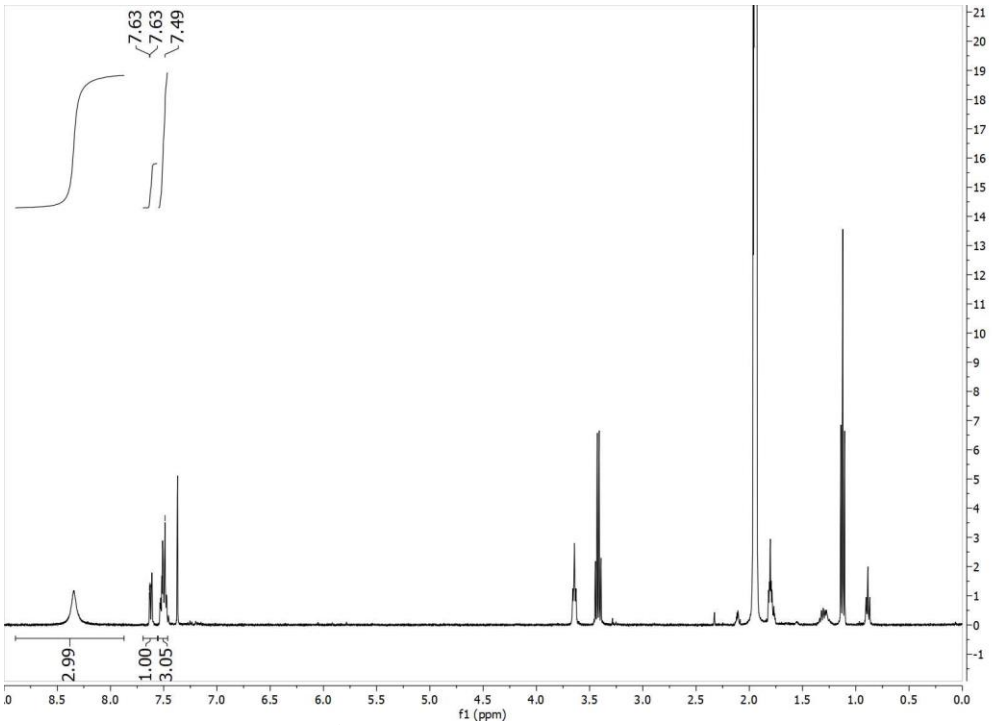

Fig. S57. The 400 MHz ^{1}H NMR spectrum of 2-chloroanilinium triflate ([$^{2\text{-Cl}}$PhNH$_3$][OTf]) in MeCN-d_3 at room temperature.

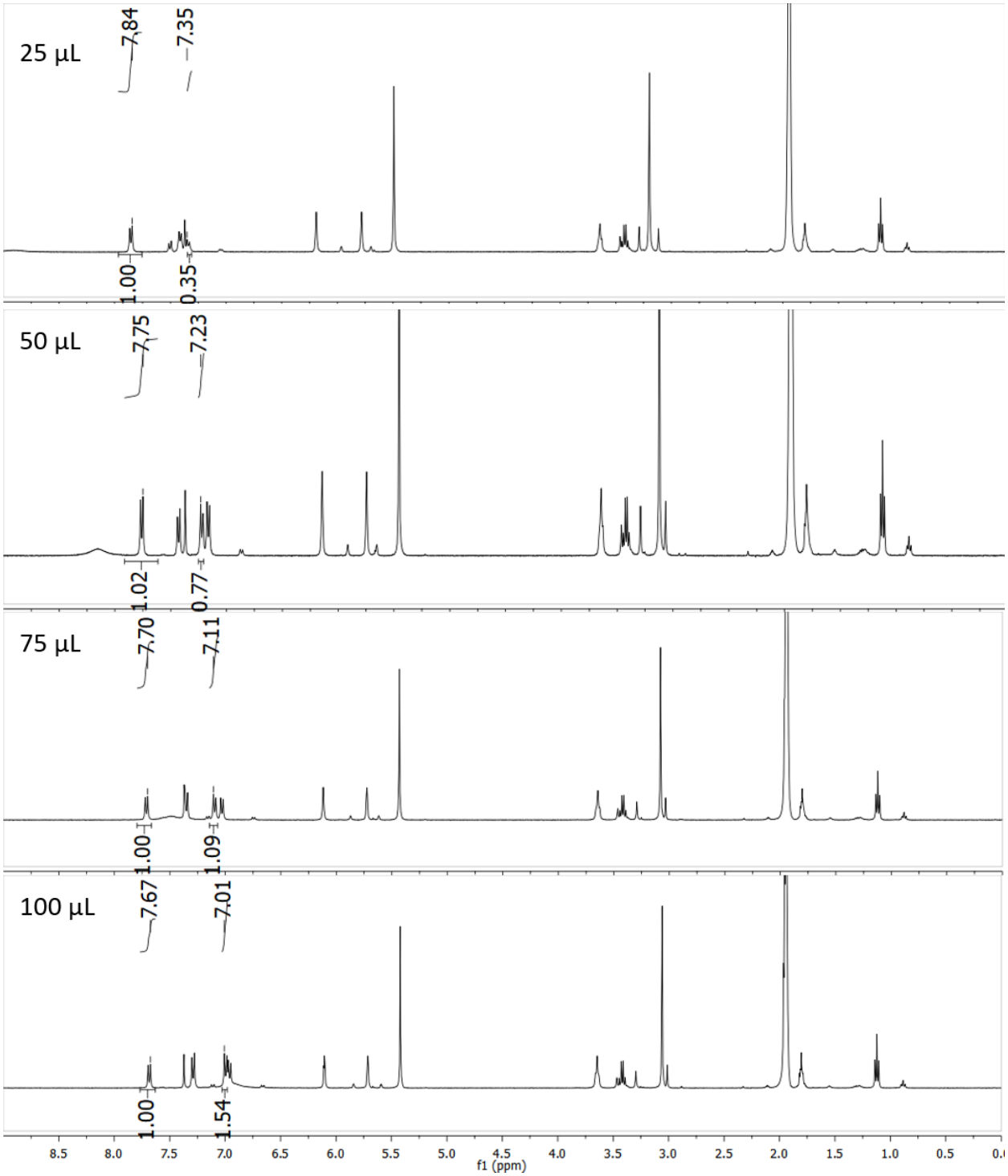

Fig. S58. 400 MHz ^{1}H NMR spectra in MeCN-d_3 at room temperature of titration experiments of [(Cp)**Co**(Cp^{NH})][OTf]$_2$ with $^{4\text{-Cl}}PhNH_2$. Only one integral and peak pick for both Co and the aniline are shown for clarity, but all of the data shown in above in Tables S3-S5 was used to determine the equilibrium constants (Experiment #1 in Table S12).

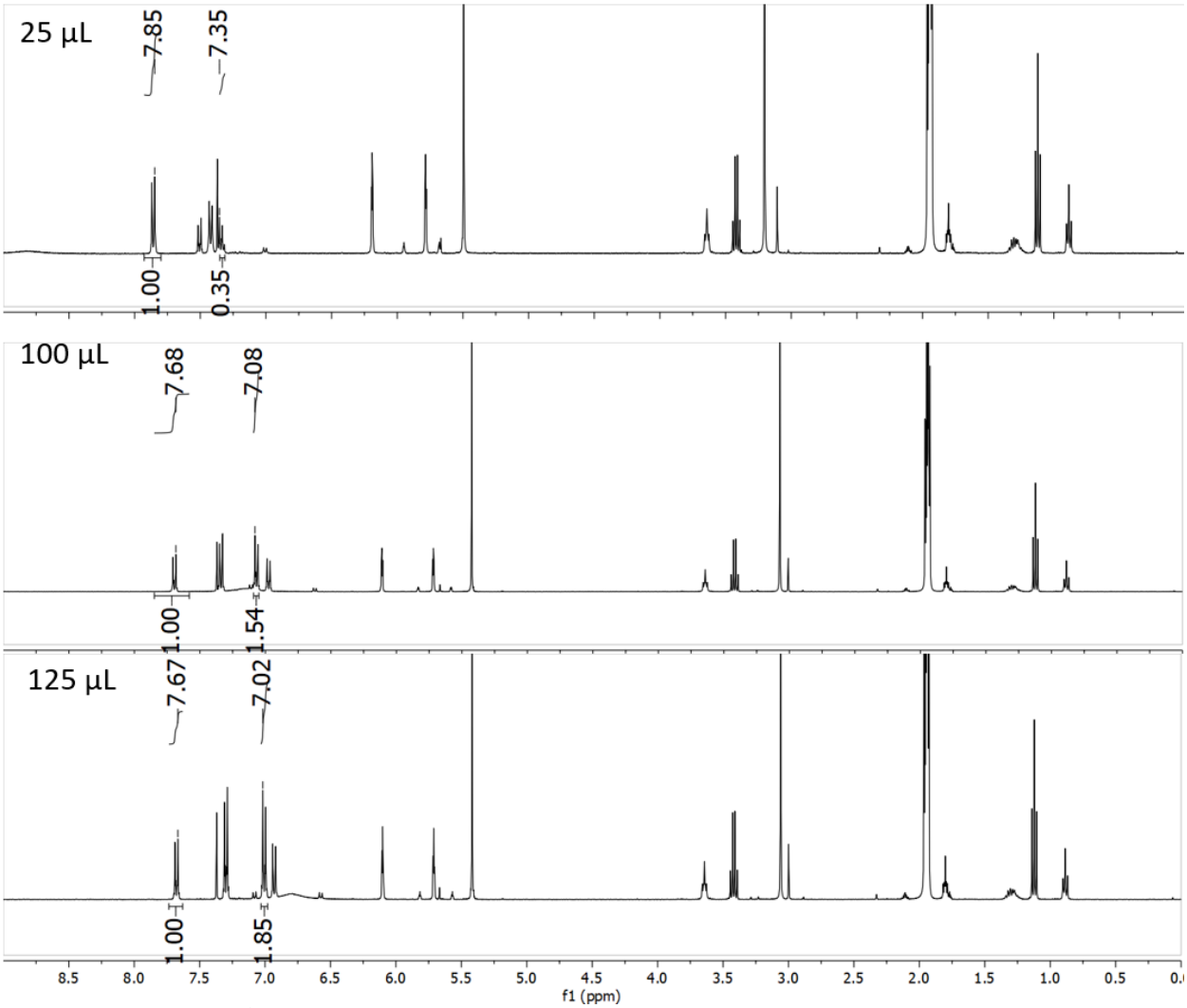

Fig. S59. 400 MHz ^{1}H NMR spectra in MeCN-d_3 at room temperature of titration experiments of [(Cp)**Co**(Cp^{NH})][OTf]$_2$ with $^{4\text{-Cl}}PhNH_2$. Only one integral and peak pick for both Co and the aniline are shown for clarity, but all the data shown in the above Tables S6-S8 was used to determine the equilibrium constants ((Experiment #2 in Table S12).

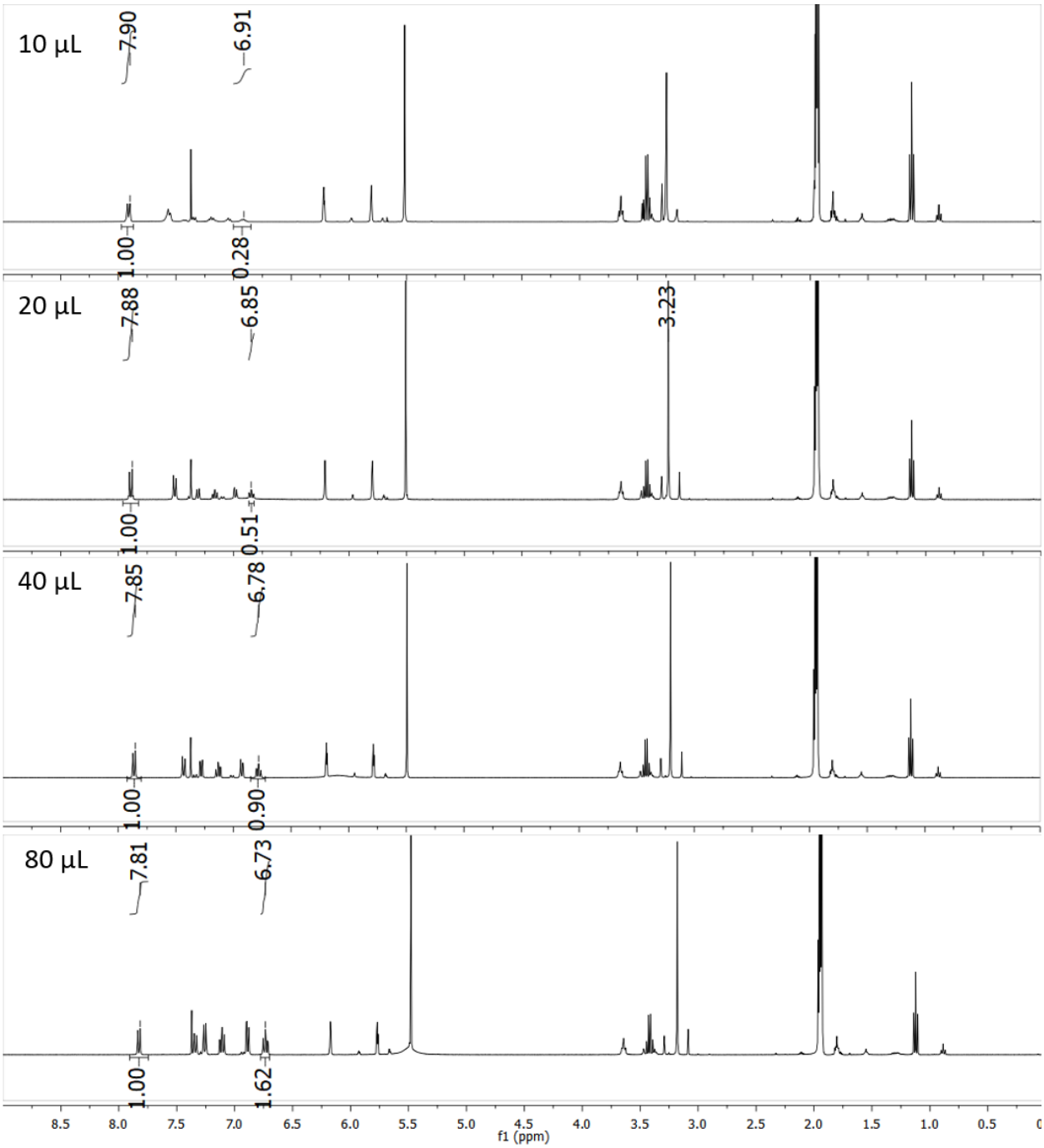

Fig. S60. 400 MHz ^{1}H NMR spectra in MeCN-d_3 at room temperature of titration experiments of [(Cp)**Co**(Cp^{NH})][OTf]$_2$ with $^{2\text{-Cl}}PhNH_2$. Only one integral and peak pick for both Co and the aniline are shown for clarity, but all the data shown in the above Tables S9-S11 was used to determine the equilibrium constants ((Experiment #3 in Table S12).

S.11. Experimental Thermochemistry:

BDFE = bond dissociation free energy

C_G = solvent-dependent thermodynamic constant accounting for the energy of formation of H· from one proton and one electron

$\Delta G(H^-)$ = hydricity

C_{Hyd} = solvent-dependent thermodynamic constant accounting for the energy of formation of H^- from one proton and two electrons

Calculation of the Homolytic N–H Bond Strength for [(Cp)**Co**(Cp^{NH})][OTf]:

$BDFE = 1.37\times pK_a + 23.06\times E°_1 + C_G$

$BDFE_1 = 1.37\times 8.6 + 23.06\times -1.21 + 54.9$

$BDFE_1 = 39\ kcal\cdot mol^{-1}$

Calculation of the Homolytic N–H Bond Strength for [(Cp)**Co**(Cp^{NH})][OTf]$_2$:

$BDFE = 1.37\times pK_a + 23.06\times E°_2 + C_G$

$BDFE_2 = 1.37\times 8.6 + 23.06\times 0.54 + 54.9$

$BDFE_2 = 79\ kcal\cdot mol^{-1}$

Calculation of the Heterolytic N–H Bond Strength for [(Cp)**Co**(Cp^{NH})][OTf]:

$\Delta G(H^-) = 1.37\times pK_a + 23.06\times E°_1 + 23.06\times E°_2 + C_{Hyd}$

$\Delta G(H^-) = 1.37\times 8.6 + 23.06\times 0.54 + 23.06\times -1.21 + 79.6$

$\Delta G(H^-) = 76\ kcal\cdot mol^{-1}$

Calculation of the pK_a of [(Cp)**Co**(Cp^{NH})][OTf]

$BDFE = 1.37\times pK_a + 23.06\times E°_3 + C_G$

$pK_a = (BDFE - 23.06\times E° - C_G)/1.37$

$pK_a = (38.8 - 23.06\times -1.35 - 54.9)/1.37$

$pK_a = 11.0$

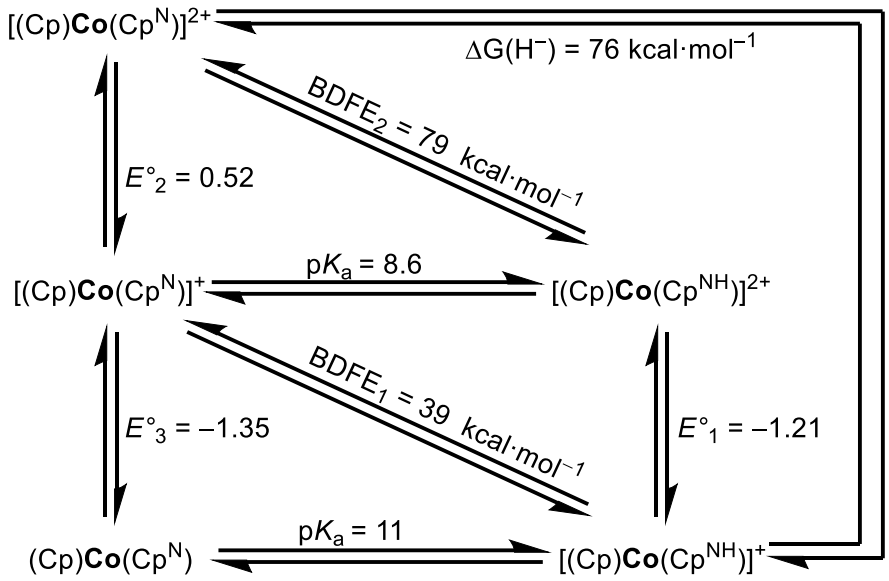

Fig. S61. Thermochemical relationships in acetonitrile for cobaltocene species in this study. Potentials are reported vs $Fc^{+/0}$.

S.12. Computational Thermochemistry

The experimentally-determined spin state was used for each calculation when known. For $[(Cp)\mathbf{Co}(Cp^N)]^-$ the ground state was assumed to be a triplet (S = 1) based on the spin state of other 20 e⁻ metallocenes.(*56*) For $[(Cp)\mathbf{Co}(Cp^N)]^{2+}$, the ground state was assumed to be S = ½ on the basis of other aniline radical cations.(*57*) Both $[(Cp)\mathbf{Co}(\eta^4\text{-}C_5H_6)]^+$ was assumed to occupy an S = ½ ground state based on analogy to the Cp*-variant, $[(Cp^*)\mathbf{Co}(\eta^4\text{-}C_5Me_5H)]^+$.(*16*)

Table S13. Calculated thermochemical properties of interest

Species	**Reduction Potential (V vs $Fc^{+/0}$)**	**pK_a**	**BDFE (kcal·mol^{-1})**	**Hydricity (kcal·mol^{-1})**	**ΔG_{calc} (Hartrees)**
$[(Cp)\mathbf{Co}(Cp^N)]^{2+}$ (S = ½)	0.42	N/A	N/A	N/A	−2134.8921
$[(Cp)\mathbf{Co}(Cp^N)]^+$ (S = 0)	−1.58	N/A	N/A	N/A	−2135.0765
$(Cp)\mathbf{Co}(Cp^N)$ (S = ½)	−2.28	N/A	N/A	N/A	−2135.1874
$[(Cp)\mathbf{Co}(Cp)]^-$ (S = 1)	N/A	N/A	N/A	N/A	−2135.2725
$[(Cp)\mathbf{Co}(Cp^{NH})]^{2+}$ (S = 0)	−1.19	7.9	75.6	N/A	−2135.5068
$[(Cp)\mathbf{Co}(Cp^{NH})]^+$ (S = ½)	N/A	14.5	38.5	70.8	−2135.6321
$[Cp_2Co]^+$ (S = 0)	−1.45	N/A	N/A	N/A	−1769.9628
Cp_2Co (S = ½)	−2.20	N/A	N/A	N/A	−1770.0783
$[Cp_2Co]^-$ (S = 1)	N/A	N/A	N/A	N/A	−1770.1639
$[(Cp)\mathbf{Co}(\eta^4\text{-}C_5H_6)]^+$	−0.42	9.0	33.8	N/A	−1770.5110

(*S* = ½)					
(Cp)**Co**(η^4-C_5H_6) (*S* = 0)	N/A		57.8	46.8	−1770.6645
PhC(O)Me (*S* = 0)	−2.32	N/A	N/A	N/A	−385.0247
$[PhC(O)Me]^-$ (*S* = ½)	N/A	N/A	N/A	N/A	−385.1083
$[PhC(OH)Me]^+$ (*S* = 0)	−0.73	0.3	N/A	N/A	−385.4384
PhC(OH)Me (*S* = ½)	N/A	N/A	38.7	N/A	−385.5806
$C_3H_7C(O)Me$ (*S* = 0)	N/A	N/A	N/A	N/A	−271.8412
$[C_3H_7C(OH)Me]^+$ (*S* = 0)	−1.09	0.4	N/A	N/A	−272.2520
$C_3H_7C(OH)Me$ (*S* = ½)	N/A	N/A	28.5	N/A	−272.3808
Cp_2Fe (*S* = 0)	N/A	N/A	N/A	N/A	−1651.0428
$[Cp_2Fe]^+$ (*S* = ½)	N/A	N/A	N/A	N/A	−1650.8737
CO_2 (*S* = 0)	N/A	N/A	N/A	N/A	−188.7065
$[HCO_2]^-$ (*S* = 0)	N/A	N/A	N/A	N/A	−189.4038
$^{2\text{-Cl}}PhNH_2$	N/A	N/A	N/A	N/A	−747.3458

(*S* = 0)					
$[^{2\text{-Cl}}PhNH_3]^+$ (*S* = 0)	N/A	N/A	N/A	N/A	−747.7760
$^{4\text{-CF3}}$PhC(O)Me (*S* = 0)	N/A	N/A	N/A	N/A	-722.2469
$^{4\text{-CF3}}$PhC(OH)Me (*S* = ½)	N/A	N/A	42.0	N/A	-722.8080
$^{4\text{-Cl}}$PhC(O)Me (*S* = 0)	N/A	N/A	N/A	N/A	-844.6732
$^{4\text{-Cl}}$PhC(OH)Me (*S* = ½)	N/A	N/A	39.0	N/A	-845.2296
$^{4\text{-Me}}$PhC(O)Me (*S* = 0)	N/A	N/A	N/A	N/A	-424.3407
$^{4\text{-Me}}$PhC(OH)Me (*S* = ½)	N/A	N/A	37.2	N/A	-424.8942
$^{4\text{-OMe}}$PhC(O)Me (*S* = 0)	N/A	N/A	N/A	N/A	-499.5916
$^{4\text{-OMe}}$PhC(OH)Me (*S* = ½)	N/A	N/A	36.5	N/A	-500.1441

S.13. GC calibration curves

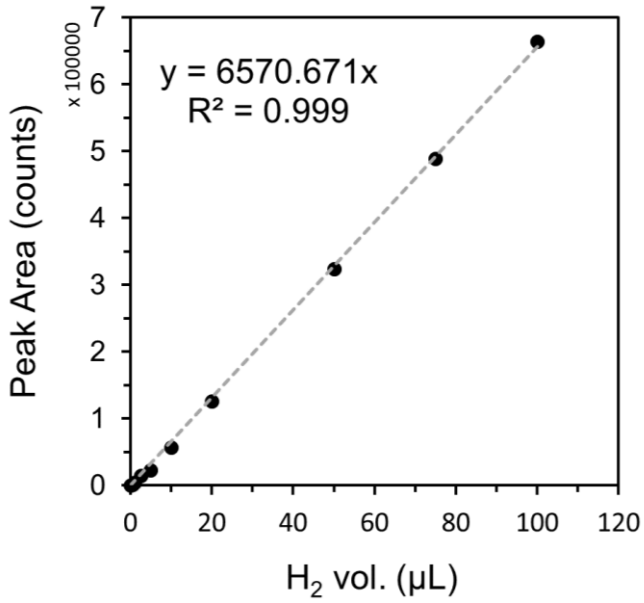

Fig. S62. Standard calibration curve for the quantification of H_2 by GC-TCD. The data for the linear fitting was obtained by direct injection of pure H_2 gas.

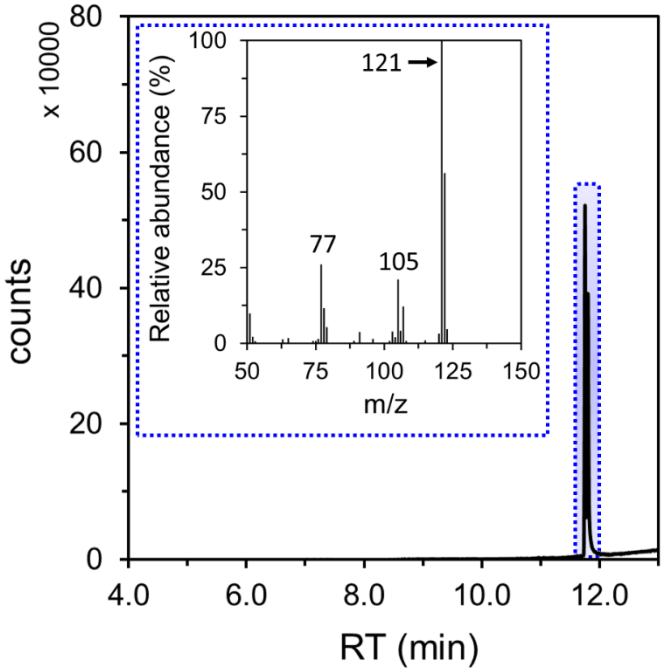

Fig. S63. Example of GC-FID chromatogram obtained by injection of an ethyl acetate solution containing 50 mM acetophenone 25 mM 2,3-diphenyl-2,3-butanediol. Inset shows the mass spectrum of the peaks placed at 11.66-11.87 min.

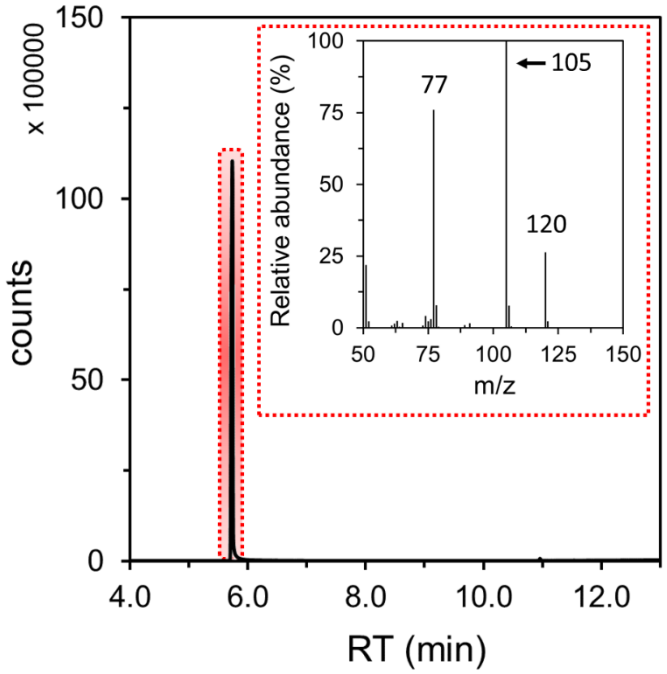

Fig. S64. Example of GC-FID chromatograms obtained by injection of an ethyl acetate solution containing 50 mM acetophenone. Inset shows the mass spectrum of the peak placed at 5.67-6.06 min.

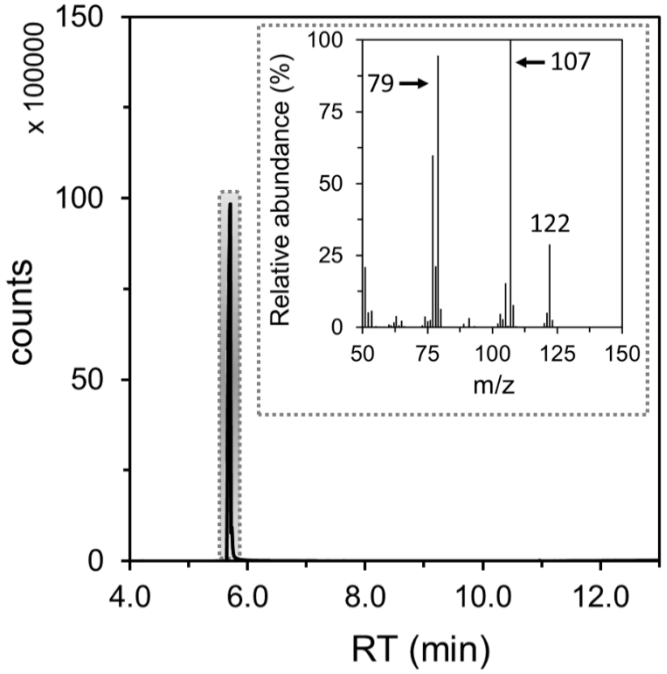

Fig. S65. Example of GC-FID chromatograms obtained by injection of an ethyl acetate solution containing 50 mM 1-phenylethanol. Inset shows the mass spectrum of the peak placed at 5.58-6.05 min.

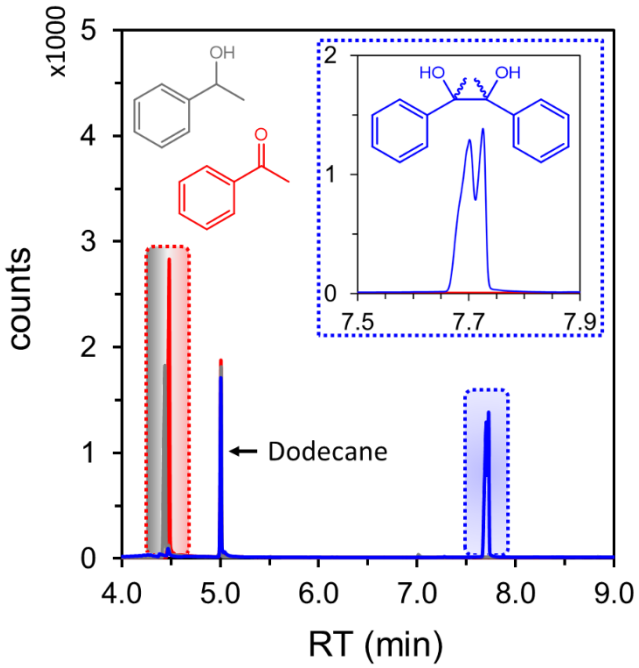

Fig. S66. Example of GC-FID chromatograms obtained by injection of an ethyl acetate solution containing dodecane as an internal standard and either 50 mM acetophenone (red trace) or 25 mM 2,3-diphenyl-2,3-butanediol (blue trace).

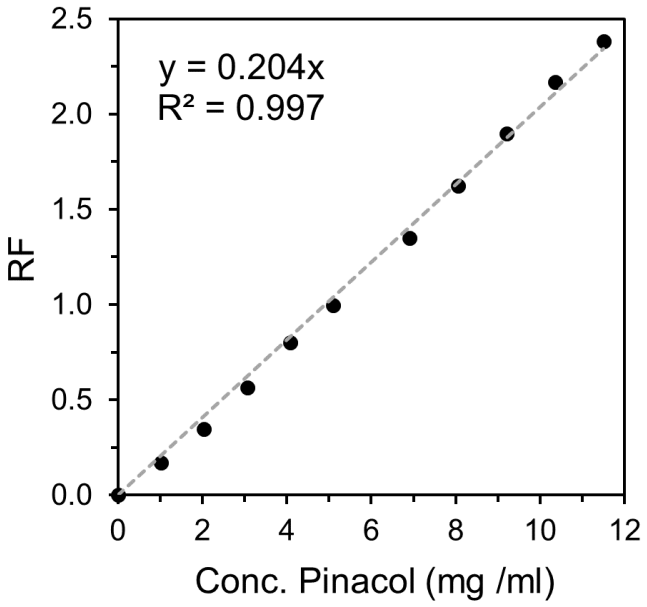

Fig. S67. Standard calibration curve for the quantification by GC-FID of 2,3-diphenyl-2,3-butanediol via GC-FID. The data for the linear fitting was obtained by injection of different standard solutions in ethyl acetate with different concentrations of 2,3-diphenyl-2,3-butanediol, obtained from dilution of a 50 mM stock solution. Dodecane was employed as internal standard.

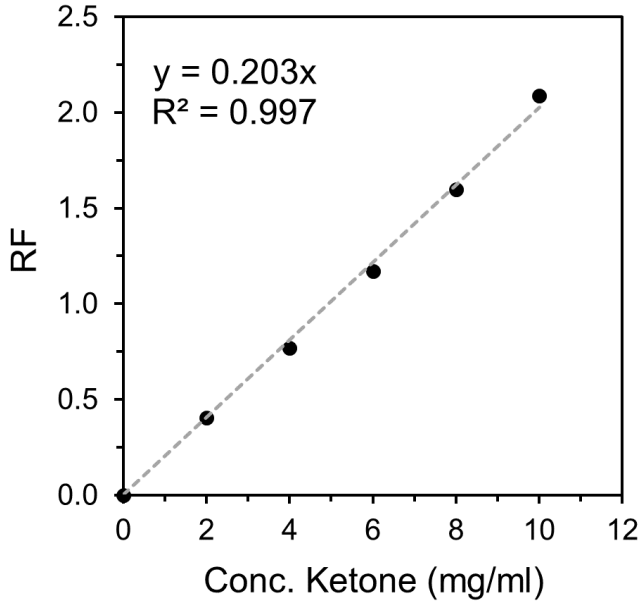

Fig. S68. Standard calibration curve for the quantification by GC-FID of acetophenone. The data for the linear fitting was obtained by injection of different standard solutions in ethyl acetate with different concentrations of acetophenone, obtained from dilution of a 50 mM stock solution. Dodecane was employed as internal standard.

S.14. Controlled Potential Coulometry

Table S14. Results summary from CPE experiments.

Run	% Pinacol (% FE)	% Ketone	TONs
[(Cp)**Co**(Cp^N)]$^+$	83.0 (39.0)	10.7	41.5
Blank	10.4 (46.6)	0	-
$[Cp_2Co]^+$	5.6 (2.6)	0	2.8

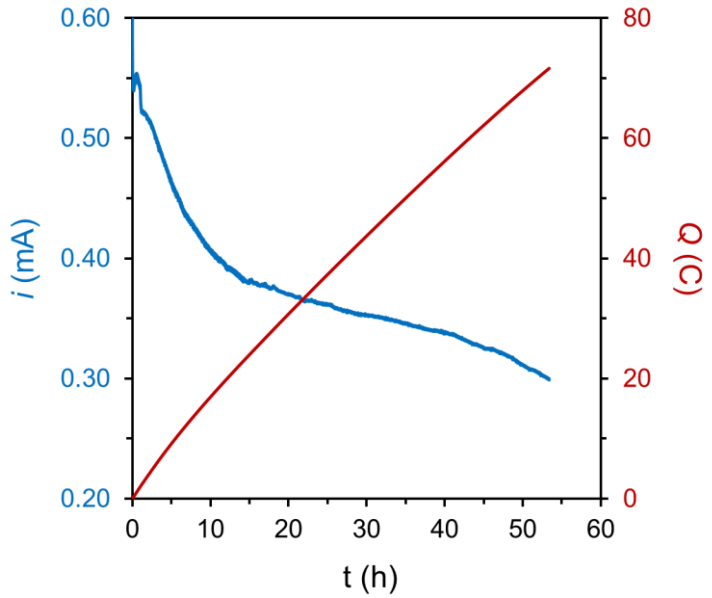

Fig. S69. Current intensity (blue trace) and charge (red trace) profiles obtained during CPE at −1.30 V vs $Fc^{+/0}$ of a solution containing 1 mM [(Cp)**Co**(Cp^N)][OTf], 100 mM [$^{4\text{-CN}}$PhNH$_3$][OTf] and 50 mM of acetophenone in DME with 0.1 M [TBA][PF_6]. A BDD plate (1 cm^2 geometric area) was used as the working electrode, a glassy carbon plate electrode as the counter electrode, and a silver wire in a 5 mM AgOTf solution as the reference electrode.

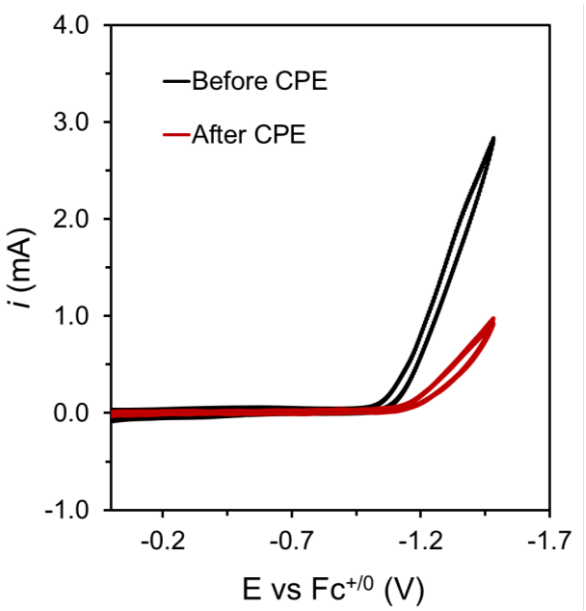

Fig. S70. CVs before (black trace) and after (red trace) CPE at −1.30 V vs $Fc^{+/0}$ of a solution containing 1 mM [(Cp)**Co**(Cp^{N})][OTf], 100 mM [$^{4\text{-}CN}PhNH_3$][OTf] and 50 mM acetophenone in DME with 0.1 M [TBA][PF_6]. The BDD plate used during the CPE electrode was used as the working electrode for the CVs.

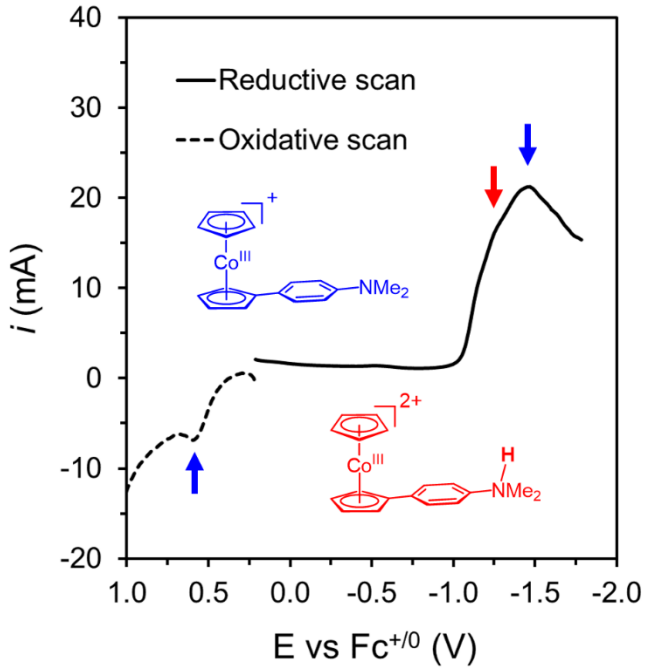

Fig. S71. DPVs in the oxidative (dashed line) and reductive (solid line) direction with respect to the open circuit potential of a solution containing 1 mM [(Cp)**Co**(Cp^{N})][OTf], 100 mM [$^{4\text{-}CN}PhNH_3$][OTf] and 50 mM acetophenone in DME with 0.1 M [TBA][PF_6] after CPE at −1.30 V vs $Fc^{+/0}$. A GC disk was used a working electrode.

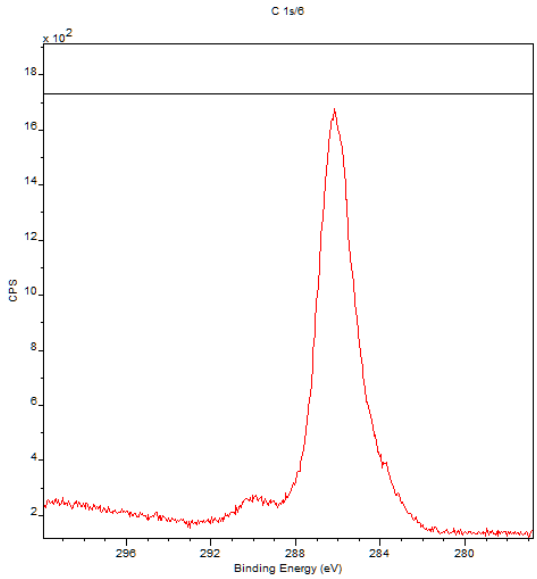

Fig. S72. XPS spectrum of the BDD plate electrode after CPE at −1.30 V vs $Fc^{+/0}$ of a solution containing 1 mM [(Cp)**Co**(Cp^{N})][OTf], 100 mM [$^{4\text{-}CN}PhNH_3$][OTf] and 50 mM acetophenone in DME with 0.1 M [TBA][PF_6]. Spectrum is centered on the region characteristic for the C 1s emission peak. Binding energy is corrected for surface charging by setting C 1s to be 285 eV.

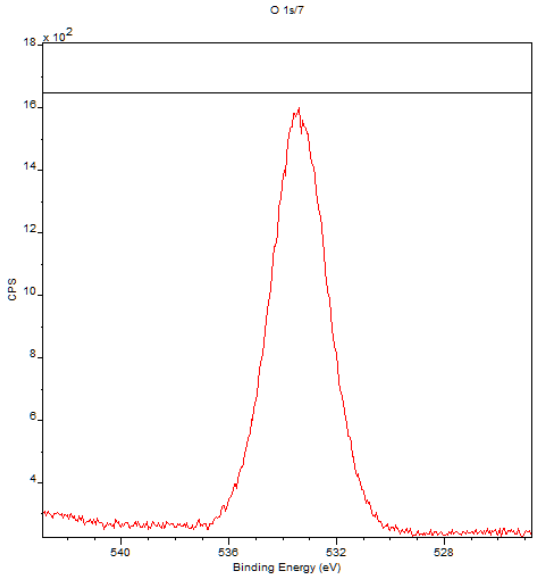

Fig. S73. XPS spectrum of the BDD plate electrode after CPE at −1.30 V vs $Fc^{+/0}$ of a solution containing 1 mM [(Cp)**Co**(Cp^{N})][OTf], 100 mM [$^{4\text{-}CN}PhNH_3$][OTf] and 50 mM acetophenone in DME with 0.1 M [TBA][PF_6]. Spectrum is centered on the region characteristic for the O 1s emission peak. Binding energy is corrected for surface charging by setting C 1s to be 285 eV.

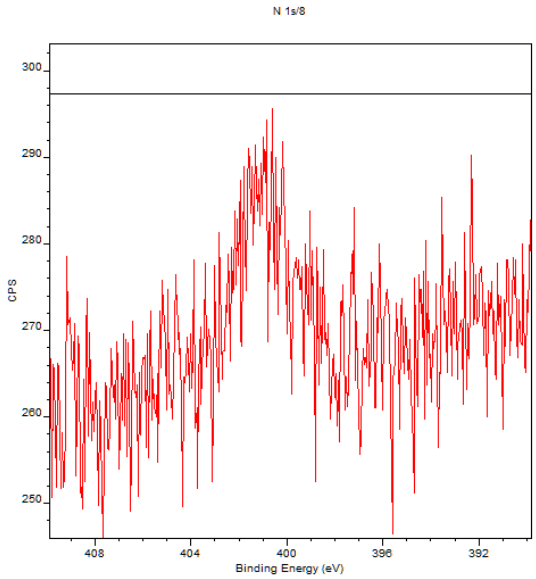

Fig. S74. XPS spectrum of BDD plate electrode after CPE at −1.30 V vs $Fc^{+/0}$ of a solution containing 1 mM [(Cp)**Co**(Cp^{N})][OTf], 100 mM [$^{4\text{-CN}}PhNH_3$][OTf] and 50 mM acetophenone in DME with 0.1 M [TBA][PF_6]. Spectrum is centered on the region characteristic for N 1s. Binding energy is corrected for surface charging by setting C 1s to be 285 eV.

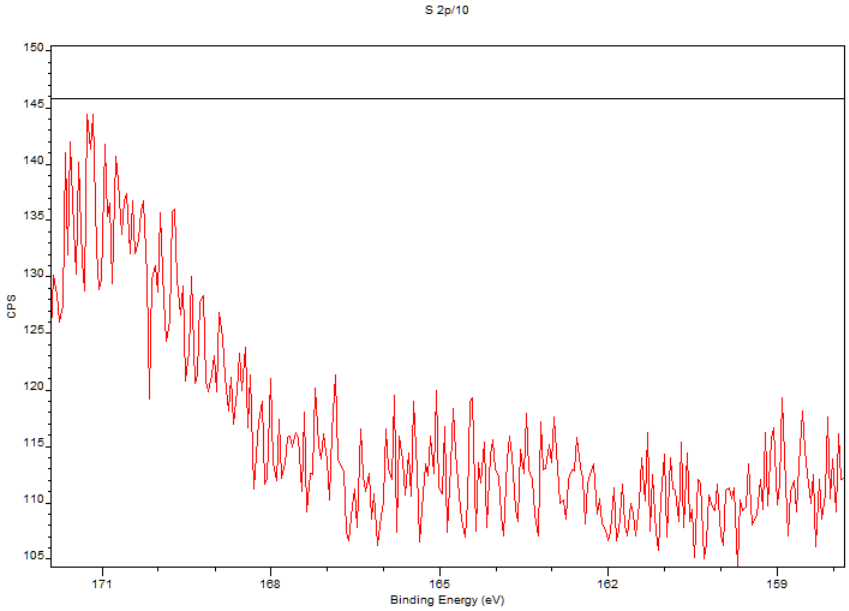

Fig. S75. XPS spectrum of the BDD plate electrode after CPE at −1.30 V vs $Fc^{+/0}$ of a solution containing 1 mM [(Cp)**Co**(Cp^{N})][OTf], 100 mM [$^{4\text{-CN}}PhNH_3$][OTf] and 50 mM acetophenone in DME with 0.1 M [TBA][PF_6]. Spectrum is centered on the region characteristic for the S 2p emission peak. Binding energy is corrected for surface charging by setting C 1s to be 285 eV.

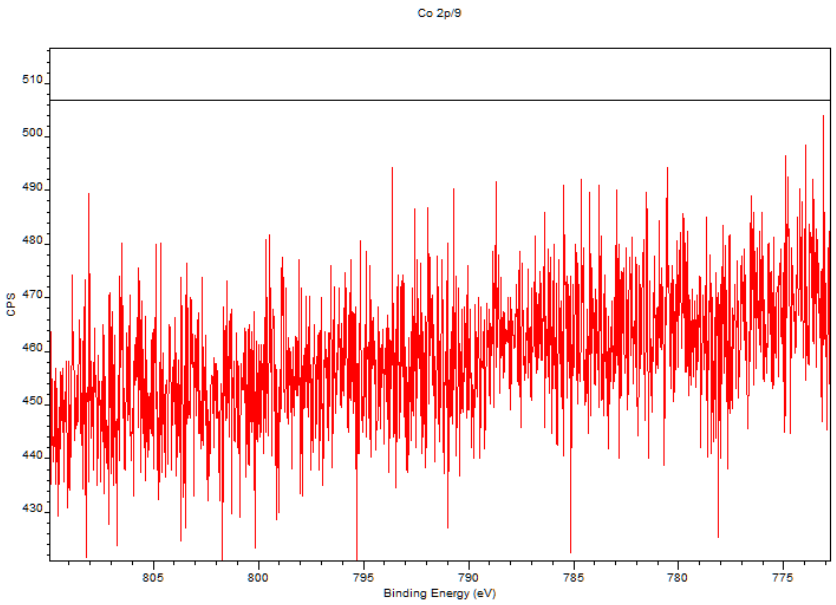

Fig. S76. XPS spectrum of the BDD plate electrode after CPE at −1.30 V vs $Fc^{+/0}$ of a solution containing 1 mM [(Cp)**Co**(Cp^{N})][OTf], 100 mM [$^{4\text{-CN}}PhNH_3$][OTf] and 50 mM acetophenone in DME with 0.1 M [TBA][PF_6]. Spectrum is centered on the region characteristic for Co 2p emission peak. Binding energy is corrected for surface charging by setting C 1s to be 285 eV.

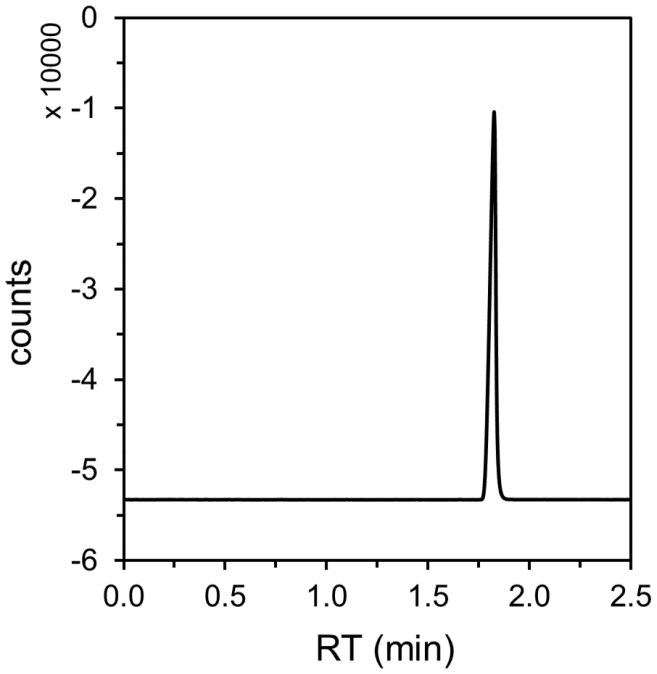

Fig. S77. GC-TCD chromatogram of the headspace after CPE at −1.30 V vs $Fc^{+/0}$ of a solution containing 1 mM [(Cp)**Co**(Cp^{N})][OTf] , 100 mM [$^{4\text{-CN}}PhNH_3$][OTf] and 50 mM acetophenone in DME with 0.1 M [TBA][PF_6], obtained by direct injection.

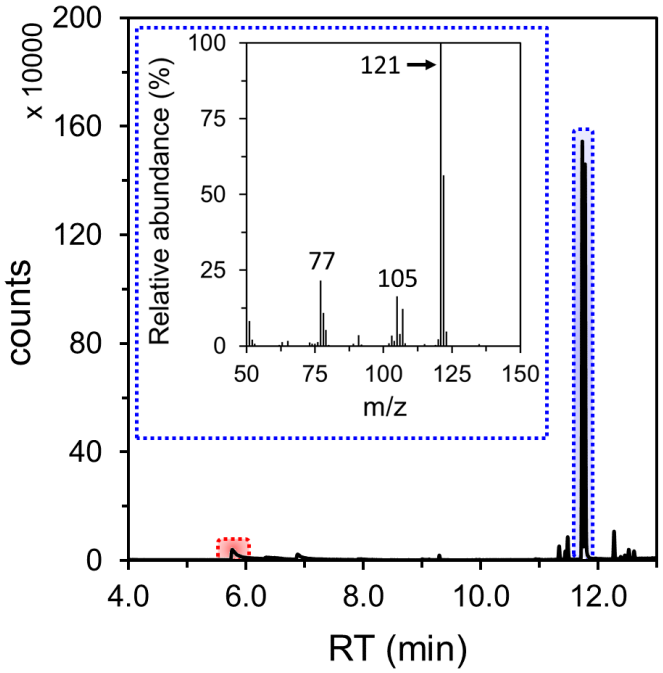

Fig. S78. GC-MS chromatogram of the analysis solution after CPE at −1.30 V vs $Fc^{+/0}$ of a solution containing 1 mM [(Cp)**Co**(Cp^{N})][OTf] , 100 mM [$^{4\text{-CN}}PhNH_3$][OTf] and 50 mM acetophenone in DME with 0.1 M [TBA][PF_6], using dodecane as internal standard. Inset shows the mass spectrum of the peaks placed at 11.66-11.87 min corresponding to the pinacol product.

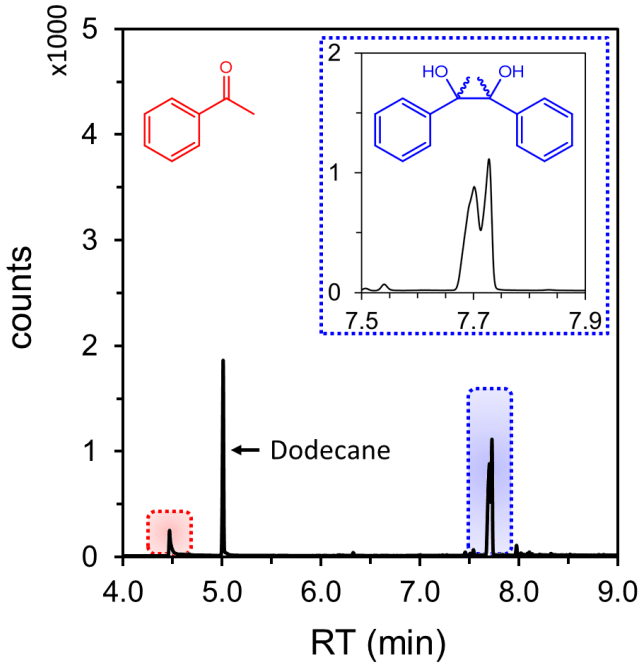

Fig. S79. GC-FID chromatogram of the analysis solution after CPE at −1.30 V vs $Fc^{+/0}$ of a solution containing 1 mM [(Cp)**Co**(Cp^{N})][OTf] , 100 mM [$^{4\text{-CN}}PhNH_3$][OTf] and 50 mM acetophenone in DME with 0.1 M [TBA][PF_6], using dodecane as internal standard.

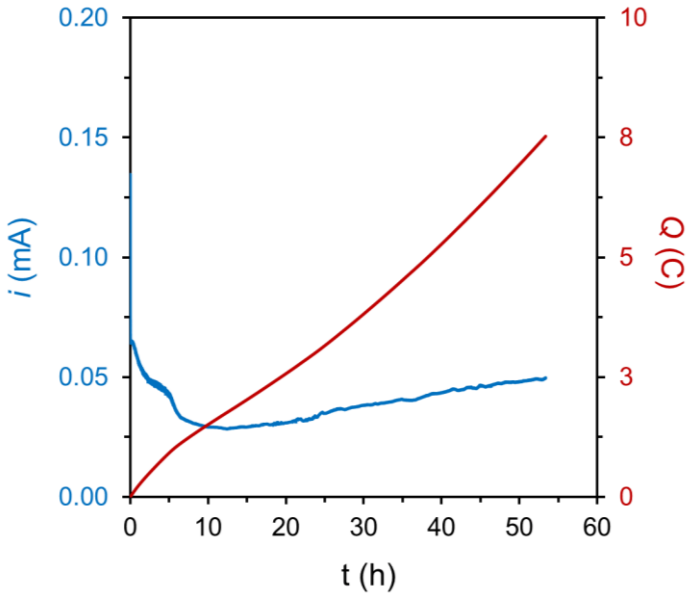

Fig. S80. Current intensity (blue trace) and charge (red trace) profiles obtained during CPE at −1.30 V vs $Fc^{+/0}$ of a solution containing 100 mM [$^{4\text{-CN}}$PhNH$_3$][OTf] and 50 mM of acetophenone in DME with 0.1 M [TBA][PF_6] in the absence of catalyst. A BDD plate (1 cm^2 geometric area) was used as working electrode, a glassy carbon plate electrode as counter electrode and a silver wire in a 5 mM AgOTf solution as reference electrode.

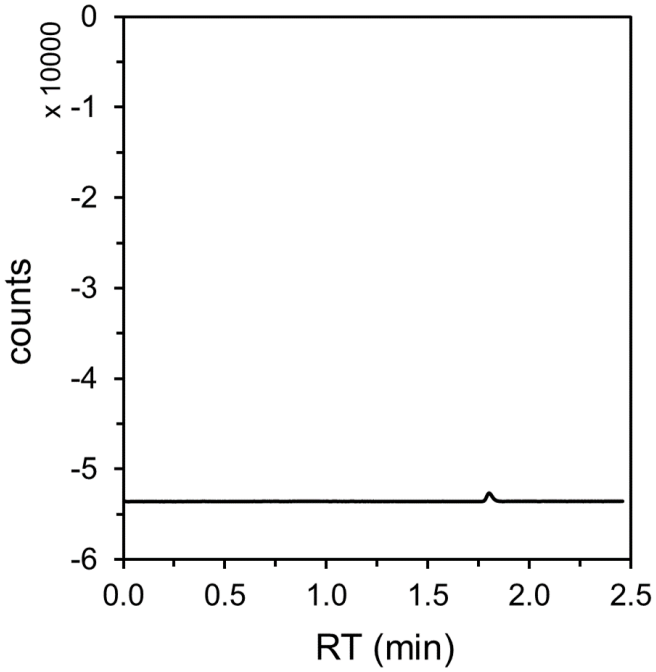

Fig. S81. GC-TCD chromatogram of the headspace after CPE at −1.30 V vs $Fc^{+/0}$ of a solution containing 100 mM [$^{4\text{-CN}}$PhNH$_3$][OTf] and 50 mM of acetophenone in DME with 0.1 M [TBA][PF_6] in the absence of catalyst, obtained by direct injection.

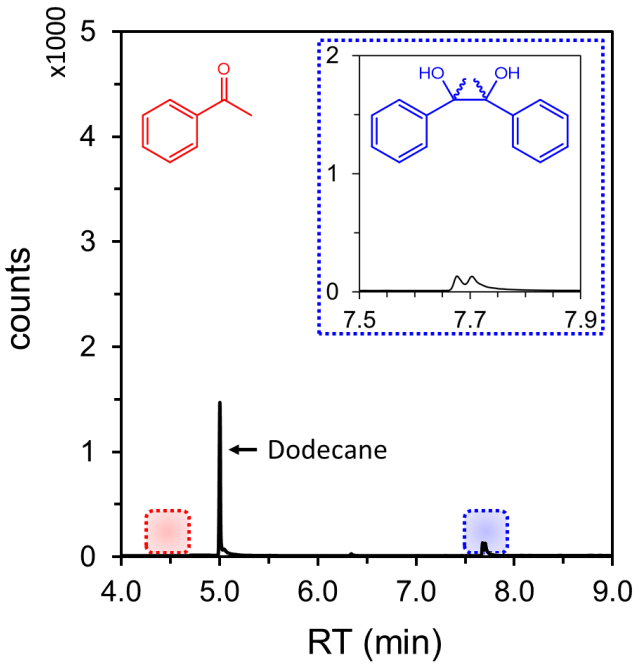

Fig. S82. GC-FID chromatogram of the analysis solution after CPE at −1.30 V vs $Fc^{+/0}$ of solution containing 100 mM [$^{4\text{-CN}}$PhNH$_3$][OTf] and 50 mM of acetophenone in DME with 0.1 M [TBA][PF_6] in the absence of catalyst, using dodecane as internal standard.

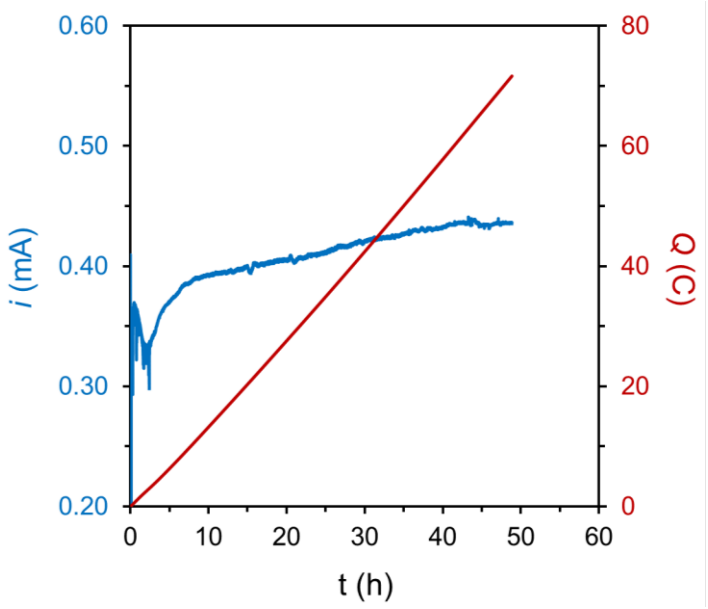

Fig. S83. Current intensity (blue trace) and charge (red trace) profiles obtained during CPE at −1.30 V vs $Fc^{+/0}$ of a solution containing 1 mM [Cp_2**Co**][PF_6], 100 mM [$^{4\text{-CN}}$PhNH$_3$][OTf] and 50 mM of acetophenone in DME with 0.1 M [TBA][PF_6]. A BDD plate (1 cm^2 geometric area) was used as working electrode, a glassy carbon plate electrode as counter electrode and a silver wire in a 5 mM AgOTf solution as reference electrode.

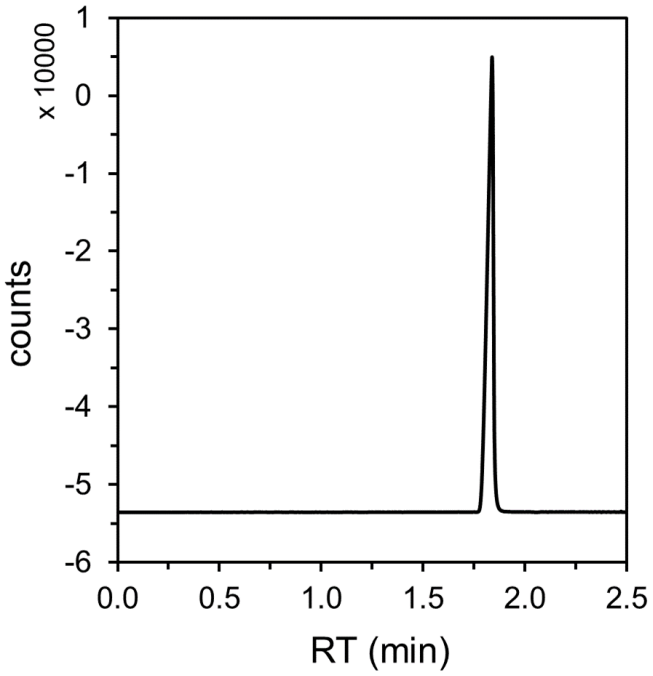

Fig. S84. GC-TCD chromatogram of the headspace after CPE at −1.30 V vs $Fc^{+/0}$ of a solution containing 1 mM [Cp_2**Co**][PF_6], 100 mM [$^{4\text{-CN}}PhNH_3$][OTf] and 50 mM of acetophenone in DME with 0.1 M [TBA][PF_6], obtained by direct injection.

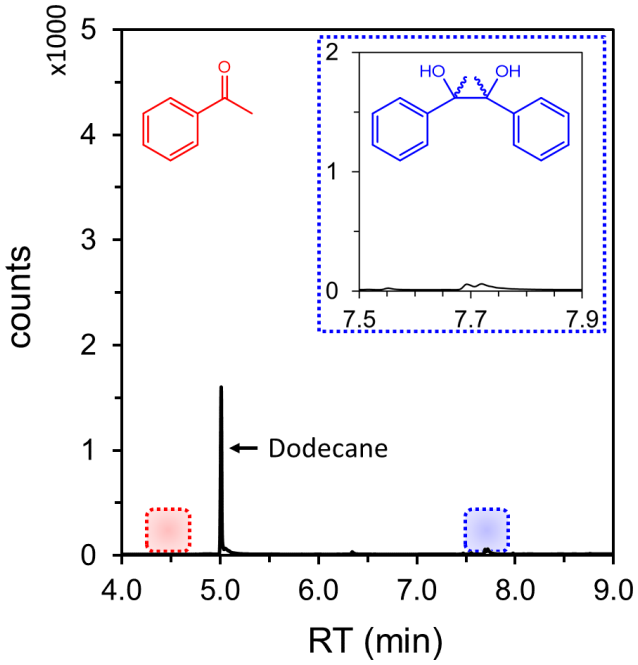

Fig. S85. GC-FID chromatogram of the analysis solution after CPE at −1.30 V vs $Fc^{+/0}$ of a solution containing 1 mM [Cp_2Co][PF_6], 100 mM [$^{4\text{-CN}}PhNH_3$][OTf] and 50 mM of acetophenone in DME with 0.1 M [TBA][PF_6], using dodecane as internal standard.

S.15 Discussion of Hammett Correlations

The log of the relative rates (k_x/k_H) was fit against a variety of Hammett and field and resonance parameters in addition to σ_p, including σ_p^+, σ_p^-, σ_f, σ_r, R^+, R^-, and F (**Figs. S86-S93**).(*28*) The fit of the data was best with σ_p, and this parameter has been used previously to contextualize CPET reactivity, so we chose to present that data. Nonetheless, all of the fits are broadly consistent with the interpretation presented in the main text.

Several reports have associated a negative Hammett slope with a CPET reaction. That framework was developed in looking at 4-substitution of phenol species that would donate a net H-atom to either organic radicals or metal-oxo species. Thus, a negative slope would be associated with positive charge build-up on the CPET donor (*i.e.*, the phenol). In our case, we are looking at substitution on the 4-position of the acetophenone, which is the H-atom acceptor. Thus, a negative slope implies positive charge build-up on the CPET acceptor, opposite of what was previously observed.

Furthermore, we observe that the reaction rate (**Fig. S94**) is slightly anti-correlated with the predicted bond strength of the α-radical species for the 4-substituted acetophenones. Although, these values are not experimentally known, the trend that the O–H bond is weaker with electron-donating substituents and stronger with electron-withdrawing substituents is consistent with observations for phenols and hydroxylamines.(*21*) Poor correlation of BDFE and rate has been previously observed for CPET reactions by Anderson and coworkers and was explained by invocation of a slightly asynchronous transition state in which the proton and electron transfer remain concerted but transfer of one is preferential to the other.(*29*) Recently, it has been posited that greater asynchronicity is associated with faster CPET reaction rates.(*30*) A full analysis of this phenomenon is, however, outside of the scope of this study.

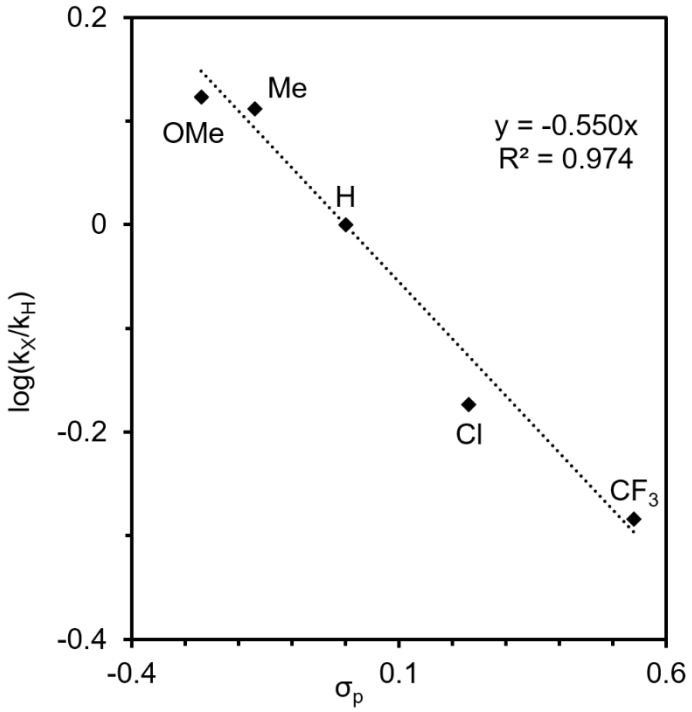

Fig. S86. Reproduction of Figure 3F in the main text showing the Hammett plot for the rate of CPET with 4-substituted acetophenones (^{R}PhC(O)Me) against σ_p.

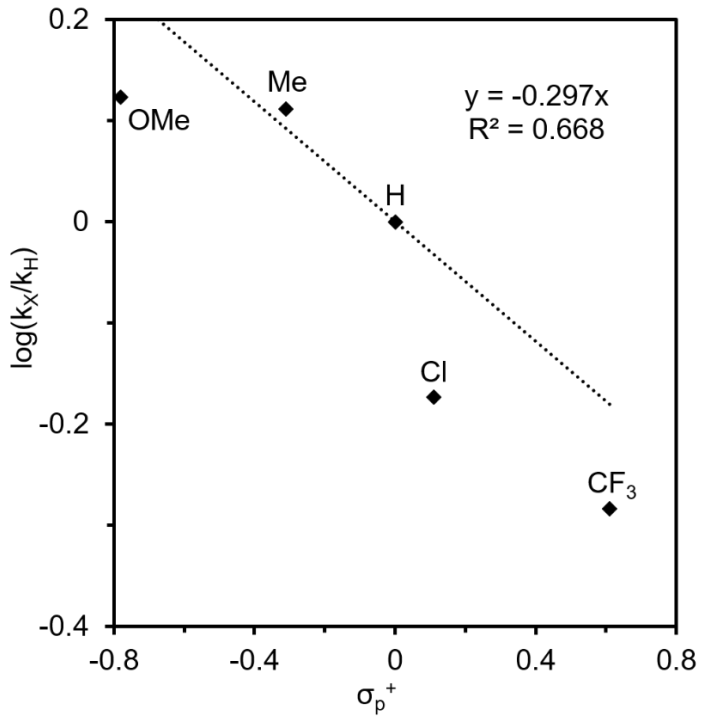

Fig. S87. Hammett plot for the rate of CPET with 4-substituted acetophenones (^{R}PhC(O)Me) against σ_p^+.

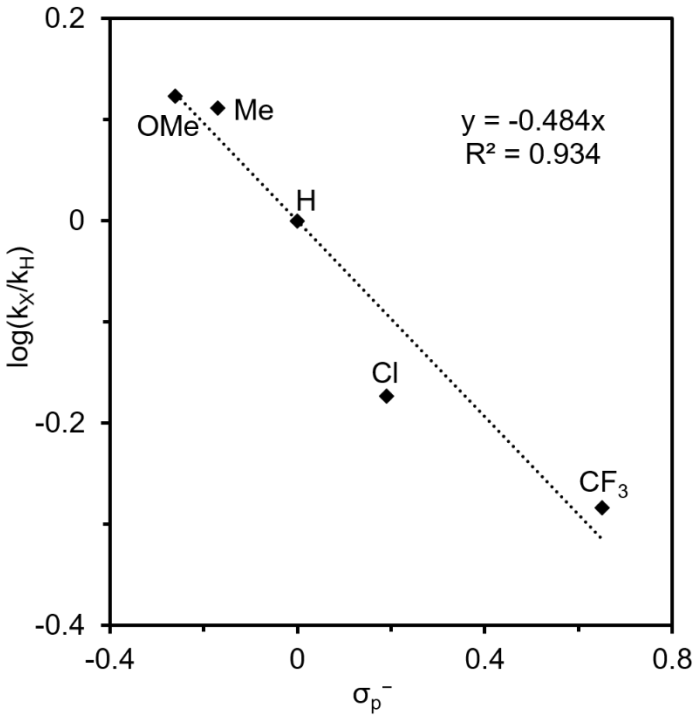

Fig. S88. Hammett plot for the rate of CPET with 4-substituted acetophenones (^{R}PhC(O)Me) against σ_p^-.

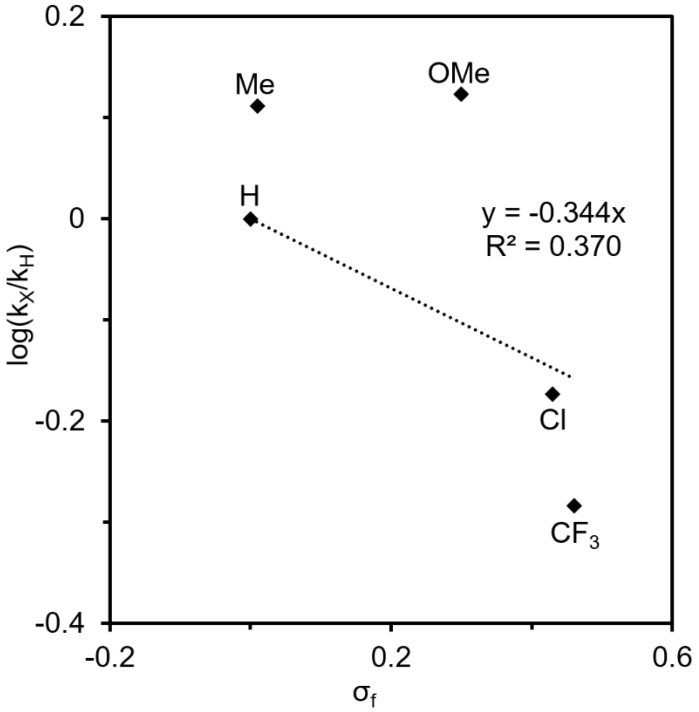

Fig. S89. Hammett plot for the rate of CPET with 4-substituted acetophenones (^{R}PhC(O)Me) against σ_f.

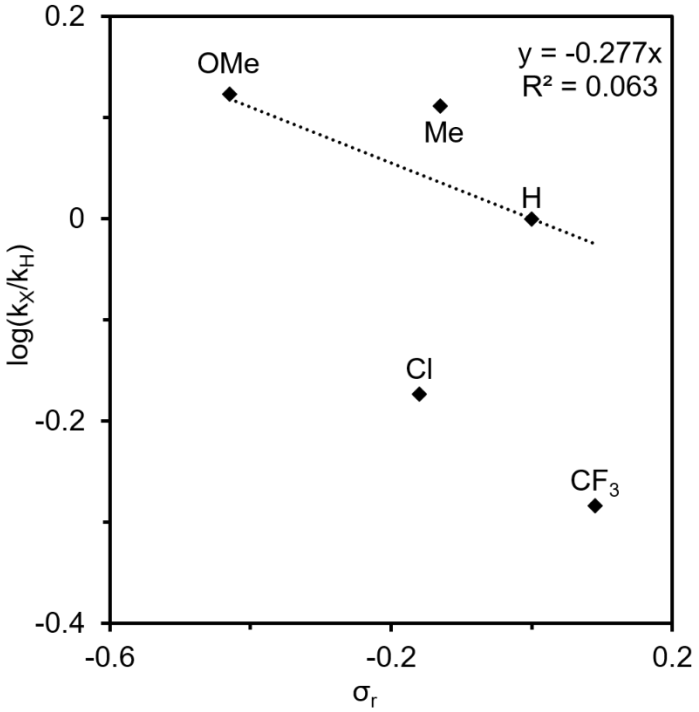

Fig. S90. Hammett plot for the rate of CPET with 4-substituted acetophenones (^{R}PhC(O)Me) against σ_r.

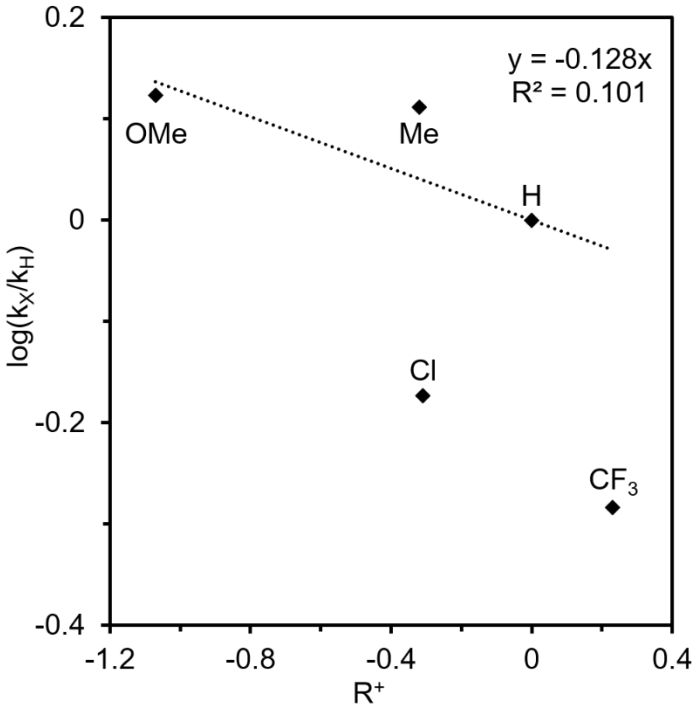

Fig. S91. Hammett plot for the rate of CPET with 4-substituted acetophenones (^{R}PhC(O)Me) against R^+.

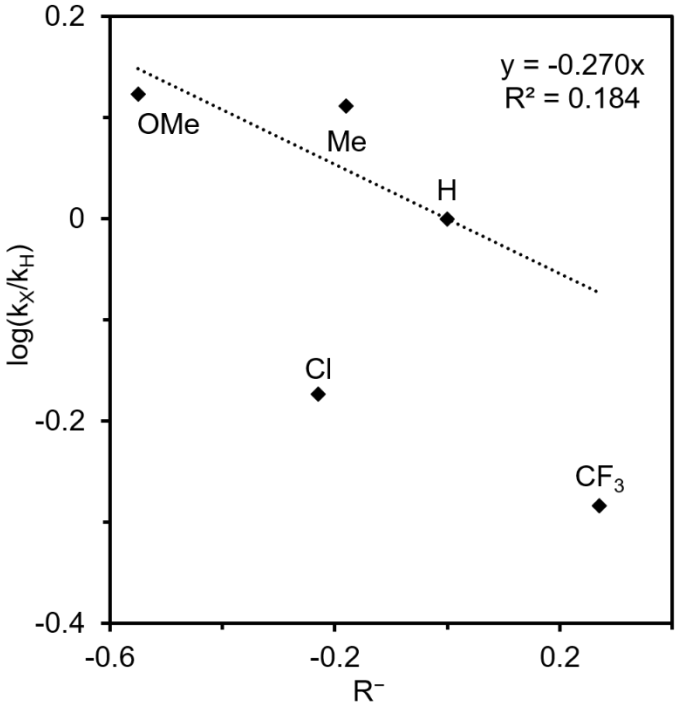

Fig. S92. Hammett plot for the rate of CPET with 4-substituted acetophenones (^{R}PhC(O)Me) against R^{-}.

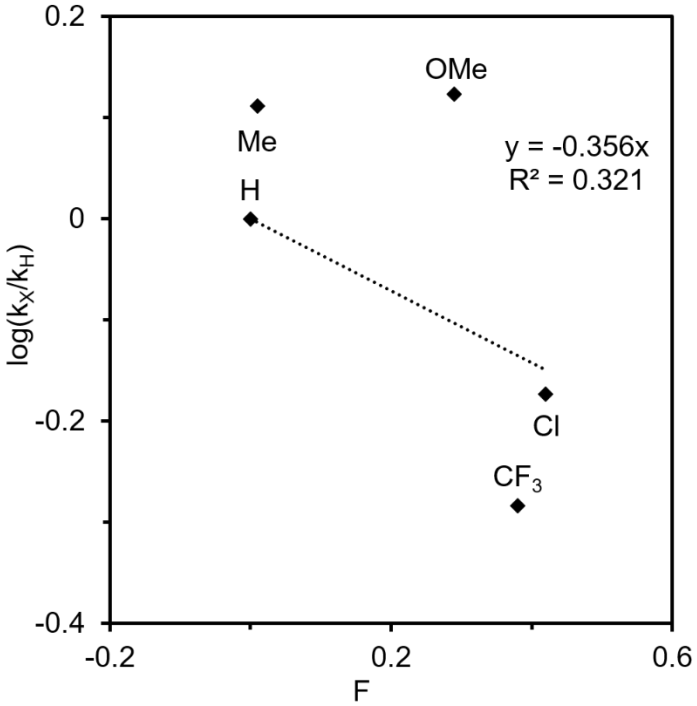

Fig. S93. Hammett plot for the rate of CPET with 4-substituted acetophenones (^{R}PhC(O)Me) against F.

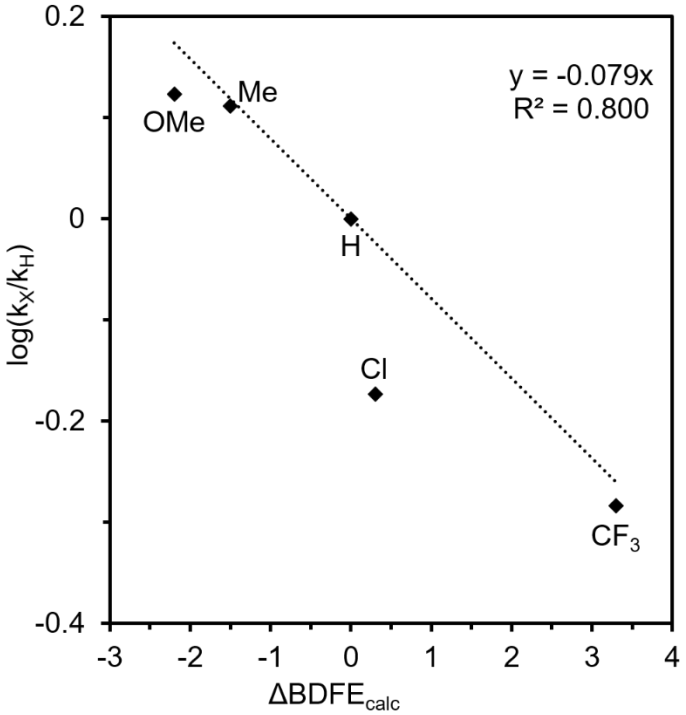

Fig. S94. Plot for the log of the relative rate of CPET with the difference in the DFT-calculated BDFE's for the neutral ketyl radical generated from 4-substituted acetophenones (^{R}PhC(O)Me).

S.16 DFT Coordinates:

Table S15. DFT coordinates for neutral ketyl radical of 2-pentanone ($C_3H_7C(OH)Me$) (S = ½).

C	-3.10464	-0.69811	0.00044	H	-4.07516	-1.00867	2.61588
H	-2.39207	-1.53097	-0.03710	C	-2.75887	0.15017	3.79375
H	-2.98495	-0.11378	-0.91898	C	-3.21681	-0.33604	5.13184
H	-4.11507	-1.12475	-0.00393	H	-3.12578	0.44755	5.89583
C	-2.87414	0.16750	1.24304	H	-4.26350	-0.65226	5.09139
H	-3.57372	1.01319	1.24365	H	-2.61973	-1.20080	5.47714
H	-1.86565	0.59430	1.21475	O	-1.50489	0.76059	3.75714
C	-3.04891	-0.62792	2.54918	H	-1.33086	1.15712	4.62934
H	-2.39180	-1.51963	2.50806				

Table S16. DFT coordinates for O-protonated 2-pentanone ($[C_3H_7C(OH)Me]^+$) (S = 0).

C	-3.18794	-0.67965	-0.00414	H	-4.22705	-0.64582	2.59339
H	-2.83890	-1.71746	-0.01521	C	-2.68680	0.02792	3.77552
H	-2.84256	-0.19426	-0.92122	C	-3.05098	-0.48718	5.10297
H	-4.28330	-0.68650	-0.01113	H	-3.59412	0.29720	5.64588
C	-2.65511	0.06204	1.22704	H	-3.65765	-1.38735	5.02759
H	-3.00101	1.10370	1.19873	H	-2.13354	-0.68605	5.67036
H	-1.55733	0.06912	1.19757	O	-1.94678	1.08253	3.77368
C	-3.12749	-0.59760	2.52212	H	-1.73191	1.38780	2.85829
H	-2.81717	-1.65270	2.59666				

Table S17. DFT coordinates for 2-pentanone ($C_3H_7C(O)Me$) (S = 0).

C	-3.18911	-0.68442	0.00544	H	-2.78435	-1.62417	2.60479
H	-2.84072	-1.72389	-0.00571	H	-4.20679	-0.61750	2.60295
H	-2.85554	-0.21114	-0.92451	C	-2.62213	0.11442	3.79865
H	-4.28577	-0.70093	-0.00106	C	-3.06002	-0.49480	5.11864
C	-2.65452	0.06611	1.22993	H	-3.61712	0.25596	5.69000
H	-2.99020	1.10918	1.20431	H	-3.68307	-1.38254	4.98635
H	-1.55908	0.09330	1.20286	H	-2.17190	-0.76051	5.70196
C	-3.10852	-0.57417	2.54013	O	-1.90834	1.11050	3.77167

Table S18. DFT coordinates for $[(Cp)\mathbf{Co}(Cp^{NH})]^{2+}$ (S = 0).

C	4.12539	-0.39598	18.94864	C	4.52642	-0.50629	17.57818
H	3.16139	-0.67304	19.35175	H	3.91645	-0.87680	16.76639
C	5.20133	0.20393	19.67676	C	5.02652	3.41591	18.11547
H	5.18935	0.46581	20.72592	H	6.00751	3.81728	18.32647
C	6.26451	0.46973	18.75744	C	4.57493	2.96067	16.84009
H	7.19748	0.96278	18.99116	H	5.15375	2.96228	15.92738
C	5.84783	0.02861	17.46030	C	3.25435	2.43549	16.99967
H	6.41238	0.13137	16.54430	H	2.65474	1.97574	16.22696

C	2.89074	2.56315	18.37386	H	5.61330	4.97087	20.30628
H	1.95991	2.23034	18.80995	Co	4.56814	1.43675	18.18612
C	3.98132	3.18791	19.07979	N	4.12873	4.50177	24.65712
C	4.02831	3.51149	20.51372	C	3.76182	5.94552	24.92063
C	3.15684	2.88844	21.42094	H	2.79632	6.13732	24.45547
H	2.45503	2.13466	21.07949	H	3.70759	6.07886	26.00031
C	3.19271	3.21201	22.77293	H	4.53441	6.58102	24.49170
H	2.52033	2.72571	23.47316	C	5.44098	4.13299	25.31307
C	4.10435	4.16465	23.21233	H	5.62972	3.07837	25.11879
C	4.98197	4.79879	22.34085	H	6.22564	4.75430	24.88486
H	5.68867	5.54378	22.69115	H	5.34008	4.32158	26.38131
C	4.93964	4.46702	20.99058	H	3.40508	3.92945	25.10650

Table S19. DFT coordinates for [(Cp)**Co**(Cp^{NH})]$^+$ (S = ½).

C	4.28971	-0.45951	18.96226	C	2.97737	3.06978	21.41368
H	3.35478	-0.79421	19.39252	H	2.18721	2.40913	21.07254
C	5.36080	0.16594	19.66941	C	3.04205	3.38940	22.76411
H	5.36819	0.42751	20.71878	H	2.30880	2.98909	23.45874
C	6.35254	0.50826	18.70485	C	4.06048	4.22149	23.22070
H	7.27231	1.04343	18.90116	C	5.01623	4.73981	22.34819
C	5.94728	-0.01712	17.42054	H	5.80879	5.39162	22.70282
H	6.50268	0.07881	16.49730	C	4.94291	4.41716	20.99994
C	4.67878	-0.61792	17.58038	H	5.68446	4.83346	20.32644
H	4.07525	-1.06419	16.80154	Co	4.58300	1.40941	18.15232
C	4.89373	3.44792	18.09880	N	4.11537	4.54950	24.66738
H	5.85130	3.91966	18.27442	C	3.92662	6.02432	24.93955
C	4.43189	2.98915	16.81865	H	2.99341	6.33581	24.47306
H	4.98248	3.05109	15.89001	H	3.88670	6.16218	26.01972
C	3.15902	2.39182	17.01008	H	4.77128	6.56304	24.51378
H	2.54919	1.91697	16.25374	C	5.36393	4.02230	25.33641
C	2.84452	2.47711	18.40872	H	5.41993	2.95142	25.14685
H	1.94206	2.08735	18.85989	H	6.22412	4.53636	24.91098
C	3.86635	3.23568	19.08326	H	5.28372	4.22627	26.40391
C	3.92430	3.57617	20.49411	H	3.32246	4.06873	25.10626

Table S20. DFT coordinates for (Cp)**Co**(Cp^{N}) (S = ½).

C	4.87670	-0.32609	19.15997	C	4.97163	-0.60230	17.74135
H	4.12181	-0.72475	19.82538	H	4.29487	-1.22957	17.17611
C	5.95226	0.52574	19.52743	C	4.60039	3.50675	17.99948
H	6.14426	0.92961	20.51189	H	5.47176	4.14395	18.08216
C	6.64108	0.87131	18.32092	C	4.11152	2.94025	16.76675
H	7.48325	1.54719	18.24573	H	4.55352	3.07668	15.78893
C	6.07562	0.11646	17.23064	C	2.99481	2.13263	17.08460
H	6.39829	0.15478	16.19888	H	2.41065	1.53653	16.39622

C	2.79963	2.20172	18.51189	H	5.09095	5.26542	20.11670
H	2.02292	1.67625	19.05270	Co	4.67476	1.44431	18.11020
C	3.72528	3.14226	19.07768	N	4.15447	4.71554	24.56382
C	3.84305	3.53707	20.47974	C	5.14373	5.72022	24.94477
C	3.23185	2.80060	21.51371	H	4.98361	6.65193	24.39331
H	2.67201	1.90081	21.27252	H	5.02636	5.93682	26.00774
C	3.34420	3.16674	22.84924	H	6.17729	5.38318	24.76640
H	2.86088	2.54830	23.59675	C	3.72465	3.79062	25.60983
C	4.08013	4.31369	23.23721	H	2.67533	3.51152	25.47372
C	4.72103	5.03940	22.20371	H	4.32980	2.87148	25.63433
H	5.31518	5.91572	22.43747	H	3.81439	4.29333	26.57425
C	4.59435	4.66142	20.87165				

Table S21. DFT coordinates for $[(Cp)\mathbf{Co}(Cp^{N})]^{2+}$ (S = ½).

C	4.84469	-0.36008	19.04960	C	3.19733	2.76360	21.53454
H	4.06651	-0.85531	19.61349	H	2.54408	1.93314	21.29108
C	5.82274	0.54137	19.57678	C	3.34382	3.12530	22.85117
H	5.90790	0.85205	20.60923	H	2.80548	2.58078	23.61555
C	6.61480	1.02391	18.48774	C	4.20222	4.21058	23.20588
H	7.40636	1.75687	18.55525	C	4.90416	4.89737	22.16953
C	6.13360	0.41172	17.28687	H	5.55761	5.72650	22.40756
H	6.49569	0.60402	16.28684	C	4.74919	4.51509	20.85864
C	5.04021	-0.44349	17.63354	H	5.28484	5.05714	20.08803
H	4.43243	-1.00847	16.94078	Co	4.65140	1.47629	18.19076
C	4.53451	3.49781	17.99492	N	4.34490	4.58324	24.50129
H	5.38331	4.16450	18.04700	C	5.22440	5.69957	24.87687
C	4.05676	2.86082	16.81430	H	4.88698	6.61732	24.38781
H	4.48228	2.96134	15.82601	H	5.18049	5.82301	25.95588
C	2.96377	2.01133	17.17612	H	6.25193	5.48115	24.57211
H	2.41486	1.36295	16.50769	C	3.62277	3.88536	25.57424
C	2.76646	2.11466	18.58280	H	2.54438	3.96824	25.41006
H	2.03015	1.56682	19.15292	H	3.90910	2.83008	25.58703
C	3.72654	3.05944	19.10948	H	3.88681	4.34689	26.52170
C	3.89285	3.44460	20.50466				

Table S22. DFT coordinates for $[(Cp)\mathbf{Co}(Cp^{N})]^{+}$ (S = 0).

C	4.86891	-0.38820	18.98434	C	5.06151	-0.47805	17.56608
H	4.09660	-0.88915	19.55155	H	4.45826	-1.05564	16.87975
C	5.84238	0.51918	19.50857	C	4.53367	3.47220	18.00995
H	5.92853	0.83296	20.53971	H	5.38481	4.13642	18.05962
C	6.62413	1.00385	18.41374	C	4.03949	2.86111	16.81803
H	7.41282	1.74068	18.47487	H	4.44625	2.98838	15.82462
C	6.14542	0.38213	17.21394	C	2.95570	2.00147	17.18236
H	6.50837	0.57102	16.21356	H	2.39257	1.36599	16.51304

C	2.78757	2.08426	18.59781	H	5.30842	5.02453	20.12179
H	2.06761	1.51807	19.17148	Co	4.65798	1.44601	18.12751
C	3.73508	3.03508	19.13148	N	4.32677	4.62654	24.54987
C	3.88790	3.43826	20.51992	C	5.22503	5.72405	24.90445
C	3.18686	2.79089	21.55834	H	4.93730	6.65183	24.39585
H	2.52322	1.96197	21.32909	H	5.16576	5.88806	25.98008
C	3.32744	3.16873	22.88090	H	6.26508	5.49018	24.64344
H	2.76907	2.63308	23.63919	C	3.59753	3.93262	25.61002
C	4.18941	4.23939	23.24810	H	2.51313	4.00509	25.45978
C	4.89949	4.88996	22.20206	H	3.87478	2.87215	25.65626
H	5.56723	5.71358	22.42555	H	3.84726	4.39627	26.56362
C	4.74899	4.49254	20.88542				

Table S23. DFT coordinates for [(Cp)**Co**(Cp^N)]$^-$ (*S* = 1).

C	4.95054	-0.51911	19.06901	C	3.11956	2.89001	21.50005
H	4.18168	-1.03429	19.63268	H	2.50318	2.02544	21.26691
C	5.87890	0.43430	19.59197	C	3.25755	3.25671	22.83536
H	5.93395	0.77030	20.62044	H	2.73354	2.67464	23.58531
C	6.71723	0.87024	18.51804	C	4.06407	4.35380	23.21859
H	7.52956	1.58328	18.59385	C	4.74570	5.02865	22.17968
C	6.30062	0.19217	17.33026	H	5.39755	5.86575	22.40608
H	6.74591	0.29577	16.34765	C	4.59247	4.65299	20.84770
C	5.20819	-0.66489	17.67104	H	5.13193	5.21909	20.09259
H	4.67474	-1.31745	16.98965	Co	4.65417	1.43347	18.10450
C	4.42576	3.62186	17.94644	N	4.16179	4.76550	24.55357
H	5.25345	4.31859	18.00163	C	5.27805	5.63240	24.92488
C	3.96246	2.98467	16.75948	H	5.24402	6.57114	24.36491
H	4.34938	3.14155	15.75946	H	5.19085	5.87580	25.98556
C	2.87274	2.12437	17.11799	H	6.25925	5.15902	24.75292
H	2.27612	1.53090	16.43504	C	3.72309	3.83597	25.59218
C	2.67574	2.23385	18.52675	H	2.66419	3.59044	25.46973
H	1.90953	1.72105	19.09567	H	4.30003	2.89701	25.59519
C	3.62649	3.17586	19.05629	H	3.84286	4.32049	26.56329
C	3.77146	3.57617	20.45343				

Table S24. DFT coordinates for (Cp)**Co**(η^4-C_5H_6) (*S* = 0).

Co	0.06602	0.13108	0.00002	H	-1.51420	-0.63200	-2.15911
H	-1.73212	-2.18579	0.00034	H	-3.24485	-1.24532	0.00022
C	-1.52210	1.05778	-0.71863	H	-1.51477	-0.63102	2.15942
C	-1.55701	-0.31973	-1.12054	H	-1.45179	1.92706	1.36148
C	-2.13679	-1.16986	0.00021	C	1.66161	-0.39293	-1.15159
C	-1.55722	-0.31923	1.12070	C	1.57606	-1.24308	-0.00054
C	-1.52221	1.05807	0.71820	C	1.66150	-0.39404	1.15130
H	-1.45208	1.92645	-1.36238	C	1.85012	0.96040	0.71079

C	1.85028	0.96104	-0.70983	H	1.59455	-0.71501	2.18257
H	1.59497	-0.71283	-2.18321	H	1.94378	1.82610	1.35284
H	1.45955	-2.31865	-0.00096	H	1.94350	1.82720	-1.35129

Table S25. DFT coordinates for $[(Cp)\mathbf{Co}(\eta^4\text{-}C_5H_6)]^+$ (S = ½).

Co	0.03089	-0.01039	-0.00013	H	-1.38662	1.97366	1.34632
H	-1.53810	-2.11306	-0.00192	C	1.67613	-0.44529	-1.15118
C	-1.52187	1.10185	-0.72015	C	1.67258	-1.28717	0.00062
C	-1.62587	-0.22934	-1.16790	C	1.67584	-0.44431	1.15170
C	-2.00832	-1.12280	-0.00072	C	1.76352	0.92389	0.70764
C	-1.62515	-0.23096	1.16755	C	1.76365	0.92328	-0.70820
C	-1.52146	1.10085	0.72137	H	1.62834	-0.77341	-2.18031
H	-1.38729	1.97527	-1.34431	H	1.58700	-2.36570	0.00117
H	-1.62434	-0.54542	-2.20235	H	1.62755	-0.77168	2.18104
H	-3.10094	-1.30608	-0.00038	H	1.76752	1.79612	1.34640
H	-1.62309	-0.54845	2.20158	H	1.76683	1.79484	-1.34788

Table S26. DFT coordinates for Cp_2Co (S = ½).

Co	5.64298	2.98848	0.00015	C	6.66943	1.53235	1.16848
C	5.22994	5.01199	-0.00076	H	4.86287	4.67955	-2.19497
H	5.98647	5.78657	0.00014	H	6.42374	1.29730	2.19508
C	4.61738	4.44194	1.16821	H	6.42140	1.29937	-2.19435
H	4.86406	4.67769	2.19445	C	3.73593	3.42916	-0.72436
C	3.73272	3.43100	0.72531	C	7.55021	2.54787	0.72417
H	3.14945	2.76808	1.35141	C	7.55308	2.54602	-0.72551
C	6.05609	0.96498	0.00096	H	3.15374	2.76580	-1.35107
H	5.29960	0.19037	0.00024	H	8.13264	3.21118	1.35074
C	6.66834	1.53506	-1.16816	H	8.13604	3.20910	-1.35173
C	4.61688	4.44462	-1.16842				

Table S27. DFT coordinates for $[Cp_2Co]^+$ (S = 0).

Co	5.64309	2.98841	0.00004	C	6.58580	1.60296	1.15754
C	5.27157	4.99087	0.00012	H	4.96409	4.58464	-2.18444
H	6.04315	5.74814	0.00030	H	6.32194	1.39303	2.18461
C	4.70047	4.37385	1.15758	H	6.32129	1.39265	-2.18442
H	4.96429	4.58422	2.18456	C	3.77602	3.37502	-0.71558
C	3.77593	3.37496	0.71550	C	7.51028	2.60188	0.71538
H	3.21859	2.69971	1.35003	C	7.51009	2.60183	-0.71571
C	6.01456	0.98599	0.00013	H	3.21971	2.69936	-1.35061
H	5.24274	0.22898	0.00013	H	8.06658	3.27769	1.35023
C	6.58548	1.60286	-1.15750	H	8.06680	3.27742	-1.35047
C	4.70054	4.37402	-1.15743				

Table S28. DFT coordinates for $[Cp_2Co]^-$ (S = 1).

Co	5.64300	2.98849	0.00027	C	6.73337	1.46785	1.15654
C	5.12444	5.12473	0.00031	H	4.77176	4.76328	-2.18701
H	5.85624	5.92424	0.00062	H	6.51577	1.21404	2.18743
C	4.55281	4.50889	1.15645	H	6.51359	1.21411	-2.18687
H	4.77089	4.76257	2.18730	C	3.62954	3.51118	-0.71518
C	3.62923	3.51089	0.71448	C	7.65686	2.46601	0.71457
H	3.02606	2.87415	1.35151	C	7.65633	2.46595	-0.71511
C	6.16162	0.85223	0.00038	H	3.02724	2.87426	-1.35282
H	5.42984	0.05269	0.00068	H	8.25958	3.10306	1.35168
C	6.73252	1.46784	-1.15622	H	8.25893	3.10269	-1.35267
C	4.55337	4.50935	-1.15632				

Table S29. DFT coordinates for Cp_2Fe (S = 0).

				C	4.69641	4.37842	-1.15895
Fe	5.64299	2.98850	0.00008	C	6.58982	1.59862	1.15901
C	5.26800	4.99611	0.00008	H	4.94511	4.60357	-2.18778
H	6.02558	5.76905	0.00025	H	6.34139	1.37353	2.18793
C	4.69624	4.37838	1.15902	H	6.34060	1.37339	-2.18773
H	4.94492	4.60351	2.18787	C	3.77076	3.37809	-0.71658
				C	7.51537	2.59892	0.71639
C	3.77065	3.37805	0.71648	C	7.51518	2.59894	-0.71667
H	3.19650	2.71625	1.35222	H	3.19738	2.71600	-1.35270
C	6.01801	0.98090	0.00011	H	8.08912	3.26085	1.35236
H	5.26046	0.20792	0.00010	H	8.08899	3.26090	-1.35255
C	6.58953	1.59859	-1.15896				

Table S30. DFT coordinates for $[Cp_2Fe]^+$ (S = 1/2).

Fe	5.64300	2.98844	0.00003	C	6.66035	1.55089	1.17023
C	5.22829	5.01774	-0.01922	H	4.87499	4.64270	-2.19999
H	5.99410	5.78098	-0.02587	H	6.41128	1.33364	2.19987
C	4.66848	4.39092	1.14266	H	6.36034	1.37187	-2.17058
H	4.92576	4.60555	2.17046	C	3.70044	3.43926	-0.72957
C	3.72372	3.41052	0.69571	C	7.58550	2.53764	0.72970
H	3.15622	2.73831	1.32474	C	7.56227	2.56665	-0.69558
C	6.05782	0.95915	0.01902	H	3.13176	2.77597	-1.36732
H	5.29209	0.19583	0.02550	H	8.15357	3.20126	1.36766
C	6.61768	1.58616	-1.14272	H	8.12969	3.23915	-1.32440
C	4.62566	4.42587	-1.17032				

Table S31. DFT coordinates for $[^{2\text{-Cl}}PhNH_3]^+$ (S = 0).

C	-0.78516	-0.76780	0.00607	C	1.29697	0.46916	0.00458
C	0.60409	-0.74007	0.01072	C	0.59533	1.67273	-0.00610

C	-0.79796	1.64761	-0.01006	N	1.34092	-2.01510	0.02729
C	-1.48843	0.43416	-0.00435	H	1.14777	-2.54803	0.88553
H	-1.30275	-1.72179	0.01051	H	2.35732	-1.86107	-0.01645
H	1.13821	2.61091	-0.01168	Cl	3.04530	0.47826	0.00886
H	-1.34243	2.58592	-0.01804	H	1.08330	-2.60840	-0.77176
H	-2.57294	0.41950	-0.00737				

Table S32. DFT coordinates for $^{2\text{-Cl}}PhNH_2$ (S = 0).

C	-0.78091	-0.78224	0.03880	H	1.16567	2.56615	-0.02628
C	0.62832	-0.81676	0.06390	H	-1.32713	2.58366	-0.05584
C	1.29015	0.42716	0.03826	H	-2.56077	0.40761	-0.01946
C	0.60496	1.63735	-0.00483	N	1.31624	-2.01442	0.17546
C	-0.78982	1.64143	-0.02297	H	0.80767	-2.83345	-0.13740
C	-1.47460	0.42254	-0.00144	H	2.27343	-2.00628	-0.15929
H	-1.32051	-1.72569	0.05392	Cl	3.05285	0.44400	0.05640

Table S33. DFT coordinates for neutral ketyl radical of acetophenone (PhC(OH)Me) (S = ½).

C	1.51980	5.09335	10.88507	H	2.92959	5.45715	7.78510
H	0.99401	5.64029	11.66137	C	1.91903	5.76295	9.68813
C	1.79465	3.74830	11.07830	C	1.65048	7.13429	9.46837
H	1.47687	3.26998	12.00116	O	2.11149	7.65451	8.28220
C	2.47505	3.00121	10.10318	C	0.94263	8.08143	10.37503
H	2.68711	1.94852	10.26294	H	0.10836	8.56583	9.84808
C	2.87690	3.63929	8.91979	H	0.53888	7.58693	11.25874
H	3.40340	3.07511	8.15375	H	1.62040	8.87875	10.71312
C	2.61159	4.98362	8.70761	H	1.85184	8.59148	8.22434

Table S34. DFT coordinates for O-protonated acetophenone ($[PhC(OH)Me]^+$) (S = 0).

C	1.51936	5.13313	10.87443	H	2.86348	5.44218	7.73109
H	0.99444	5.70185	11.63268	C	1.89239	5.74040	9.65209
C	1.83437	3.80379	11.10833	C	1.60034	7.12174	9.42072
H	1.55276	3.33844	12.04631	O	2.01441	7.61098	8.28096
C	2.51185	3.06602	10.13166	C	0.93680	8.03201	10.37843
H	2.75244	2.02405	10.31795	H	0.46696	8.86982	9.85691
C	2.88110	3.65469	8.91419	H	0.20133	7.51997	10.99792
H	3.40465	3.07274	8.16341	H	1.71546	8.43364	11.04334
C	2.57783	4.98159	8.66939	H	1.79209	8.56595	8.19647

Table S35. DFT coordinates for acetophenone (PhC(O)Me) (S = 0).

C	1.44238	5.13159	10.79843	H	1.24129	3.29095	11.89570
H	0.87656	5.70061	11.52884	C	2.37553	3.01876	10.08206
C	1.64770	3.76807	11.00883	H	2.53584	1.95718	10.24780

C	2.89841	3.63589	8.94032	O	2.22237	7.74240	8.37499
H	3.46410	3.05370	8.21855	C	0.98980	8.03810	10.40116
C	2.69281	4.99540	8.72900	H	-0.03035	7.65157	10.50706
H	3.09171	5.48691	7.84716	H	1.46130	7.98021	11.38886
C	1.96326	5.75997	9.65523	H	0.95164	9.07835	10.07474
C	1.76489	7.22088	9.39174				

Table S36. DFT coordinates for anionic ketyl radical of acetophenone ($[PhC(O)Me]^{-}$) (S = ½).

C	1.44332	5.12432	10.80651	H	3.09586	5.46680	7.82945
H	0.87345	5.68250	11.54566	C	1.95855	5.80098	9.64591
C	1.65436	3.76926	11.01186	C	1.76768	7.20078	9.39071
H	1.24619	3.29889	11.90542	O	2.22429	7.78298	8.34325
C	2.38594	2.99032	10.08770	C	0.98494	8.03179	10.40589
H	2.54863	1.92930	10.25597	H	-0.06316	7.70833	10.49434
C	2.89970	3.63261	8.93821	H	1.41445	7.97690	11.41690
H	3.46497	3.05301	8.20896	H	0.99257	9.07769	10.08539
C	2.69749	4.98408	8.71836				

Table S37. DFT coordinates for 4-trifluoromethylacetophenone ($^{4\text{-}CF3}PhC(O)Me$) (S = 0).

C	-3.53984	-0.63183	-0.82638	H	-4.12022	1.80215	1.50006
C	-2.14819	-0.60834	-0.82153	C	0.01879	0.27247	0.00838
C	-1.46050	0.27837	0.01829	H	0.47600	-0.45139	-0.69611
C	-2.17368	1.15108	0.85505	O	0.72056	0.99202	0.70582
C	-3.56116	1.13345	0.85468	C	-5.73899	0.24452	-0.00650
C	-4.23616	0.23671	0.01667	F	-6.26468	-0.95857	-0.35823
H	-4.07744	-1.31864	-1.47084	F	-6.27806	0.57321	1.19822
H	-1.59224	-1.28215	-1.46771	F	-6.23069	1.15284	-0.90359
H	-1.63086	1.83397	1.50062				

Table S38. DFT coordinates for neutral ketyl radical of 4-trifluoromethylacetophenone ($^{4\text{-}CF3}PhC(OH)Me$) (S = ½).

C	-3.55797	-0.64411	-0.83981	O	0.62053	1.07950	0.78705
C	-2.17684	-0.65005	-0.86626	C	0.81951	-0.69098	-0.91069
C	-1.42078	0.22648	-0.03001	H	0.61855	-1.74825	-0.69527
C	-2.14453	1.11245	0.82702	H	0.61291	-0.52983	-1.97646
C	-3.52508	1.11127	0.84627	H	1.88637	-0.50960	-0.74313
C	-4.24688	0.22923	0.02167	C	-5.73243	0.26702	0.01381
H	-4.11295	-1.32044	-1.48217	H	1.58466	0.97394	0.69560
H	-1.66513	-1.33653	-1.53287	F	-6.26258	0.65891	1.20885
H	-1.60042	1.79191	1.47333	F	-6.29653	-0.93932	-0.28716
H	-4.05630	1.79013	1.50601	F	-6.24673	1.14819	-0.91535
C	-0.01063	0.20684	-0.05214				

Table S39. DFT coordinates for 4-chloroacetophenone ($^{4\text{-Cl}}$PhC(O)Me) (S = 0).

C	-8.13645	-1.03305	0.00436	H	-9.91856	0.18635	0.00515
C	-6.73254	-1.05242	0.00218	C	-5.95490	-2.33143	0.00357
C	-6.03666	0.16739	-0.00133	C	-6.71841	-3.63631	-0.00049
C	-6.71530	1.37961	-0.00329	H	-6.01342	-4.46842	-0.00444
C	-8.11165	1.36419	-0.00117	H	-7.36318	-3.70694	0.88314
C	-8.83408	0.17229	0.00295	H	-7.36762	-3.70140	-0.88117
H	-8.70212	-1.95813	0.00745	O	-4.72452	-2.31533	0.00858
H	-4.95113	0.15479	-0.00314	Cl	-8.98043	2.88641	-0.00402
H	-6.17681	2.32067	-0.00644				

Table S40. DFT coordinates for neutral ketyl radical of 4-chloroacetophenone ($^{4\text{-Cl}}$PhC(OH)Me) (S = ½).

C	-8.15544	-1.01762	0.00090	H	-9.92489	0.19694	-0.00201
C	-6.72664	-1.06489	0.00169	C	-6.05370	-2.30699	0.00220
C	-6.03865	0.18754	0.00212	C	-6.72242	-3.64131	0.00354
C	-6.72273	1.39195	0.00005	H	-5.96793	-4.43072	-0.01091
C	-8.12218	1.38881	-0.00208	H	-7.34839	-3.77819	0.89460
C	-8.83962	0.18513	-0.00125	H	-7.37254	-3.76844	-0.87120
H	-8.72494	-1.94084	0.00182	O	-4.68845	-2.39498	0.00321
H	-4.95135	0.22784	0.00361	Cl	-8.99238	2.91506	-0.00558
H	-6.17848	2.33045	0.00012	H	-4.28660	-1.50660	0.00745

Table S41. DFT coordinates for 4-methylacetophenone ($^{4\text{-Me}}$PhC(O)Me) (S = 0).

C	-3.55190	-0.63315	-0.82590	C	0.05767	0.26953	0.00769
C	-2.15904	-0.63386	-0.83876	O	0.66536	1.04711	0.74557
C	-1.43548	0.24143	-0.01171	C	0.80934	-0.68007	-0.90001
C	-2.15089	1.11365	0.82630	H	0.55166	-1.72052	-0.66944
C	-3.54024	1.11029	0.83532	H	0.54210	-0.50675	-1.94909
C	-4.26795	0.23807	0.00785	H	1.88313	-0.53365	-0.76894
H	-4.09335	-1.32134	-1.47033	C	-5.77439	0.25755	-0.00174
H	-1.63934	-1.32403	-1.49582	H	-6.17560	0.54526	0.97472
H	-1.59739	1.78980	1.47096	H	-6.14247	0.98732	-0.73465
H	-4.07535	1.79009	1.49403	H	-6.18482	-0.71848	-0.27730

Table S42. DFT coordinates for neutral ketyl radical of 4-methylacetophenone ($^{4\text{-Me}}$PhC(OH)Me) (S = ½).

C	-3.56833	-0.63077	-0.82809	C	-4.29483	0.23832	0.01022
C	-2.18318	-0.64230	-0.84763	H	-4.10935	-1.31557	-1.47813
C	-1.42200	0.23350	-0.01336	H	-1.66809	-1.33305	-1.50851
C	-2.16715	1.10629	0.83763	H	-1.65808	1.79446	1.51070
C	-3.55416	1.10038	0.84028	H	-4.08202	1.78014	1.50616

C	-0.00866	0.21119	-0.04663	C	-5.80199	0.26629	-0.00618
O	0.75164	1.04132	0.73817	H	-6.20749	0.56100	0.96741
C	0.81658	-0.68919	-0.90542	H	-6.17889	0.98676	-0.74558
H	0.63580	-1.74808	-0.67630	H	-6.21644	-0.71264	-0.26928
H	0.59724	-0.54788	-1.97201	H	0.17824	1.61517	1.27866
H	1.87732	-0.48079	-0.74357				

Table S43. DFT coordinates for 4-methoxyacetophenone ($^{4\text{-OMe}}$PhC(O)Me) (S = 0).

C	-3.54107	-0.72510	-0.71160	O	0.69344	1.04341	0.71618
C	-2.15884	-0.66752	-0.79532	C	0.80018	-0.58696	-1.02836
C	-1.41518	0.19366	0.03693	H	0.60137	-1.64897	-0.84047
C	-2.11542	0.99284	0.95531	H	0.46433	-0.37170	-2.04933
C	-3.50056	0.94872	1.05335	H	1.87298	-0.40011	-0.95233
C	-4.22414	0.08346	0.21398	O	-5.57679	-0.03939	0.22447
H	-4.11324	-1.38820	-1.35328	C	-6.32545	0.77554	1.15420
H	-1.65608	-1.30161	-1.51856	H	-6.17238	1.84014	0.94683
H	-1.55162	1.65933	1.60095	H	-7.36997	0.51099	0.98805
H	-4.00957	1.57901	1.77344	H	-6.04295	0.54586	2.18691
C	0.06714	0.28192	-0.02682				

Table S44. DFT coordinates for neutral ketyl radical of 4-methoxyacetophenone ($^{4\text{-OMe}}$PhC(OH)Me) (S = ½).

C	-3.59344	-0.65771	-0.78724	O	0.64089	0.95168	0.86019
C	-2.21485	-0.65195	-0.87462	C	0.87442	-0.59791	-1.00952
C	-1.41163	0.14105	0.00364	H	1.46607	-1.35738	-0.47614
C	-2.11322	0.92007	0.97340	H	0.30373	-1.10603	-1.78827
C	-3.50085	0.91113	1.05915	H	1.58658	0.07766	-1.50544
C	-4.25837	0.12244	0.17985	O	-5.62842	0.04257	0.18208
H	-4.18386	-1.26770	-1.46537	C	-6.33282	0.82343	1.16400
H	-1.74218	-1.26985	-1.63200	H	-6.14227	1.89473	1.02646
H	-1.54963	1.53728	1.66463	H	-7.39068	0.61384	0.99819
H	-3.98528	1.52077	1.81462	H	-6.05238	0.52392	2.18073
C	-0.00046	0.15998	-0.07098	H	1.60051	0.90172	0.70674

References and Notes

1. M. Yan, Y. Kawamata, P. S. Baran, Synthetic organic electrochemical methods since 2000: On the verge of a renaissance. *Chem. Rev.* **117**, 13230–13319 (2017). doi:10.1021/acs.chemrev.7b00397 Medline

2. B. A. Frontana-Uribe, R. D. Little, J. G. Ibanez, A. Palma, R. Vasquez-Medrano, Organic electrosynthesis: A promising green methodology in organic chemistry. *Green Chem.* **12**, 2099–2119 (2010). doi:10.1039/c0gc00382d

3. E. Steckhan, Indirect electroorganic syntheses—A modern chapter of organic electrochemistry. *Angew. Chem. Int. Ed.* **25**, 683–701 (1986). doi:10.1002/anie.198606831

4. B. K. Peters, K. X. Rodriguez, S. H. Reisberg, S. B. Beil, D. P. Hickey, Y. Kawamata, M. Collins, J. Starr, L. Chen, S. Udyavara, K. Klunder, T. J. Gorey, S. L. Anderson, M. Neurock, S. D. Minteer, P. S. Baran, Scalable and safe synthetic organic electroreduction inspired by Li-ion battery chemistry. *Science* **363**, 838–845 (2019). doi:10.1126/science.aav5606 Medline

5. M. M. Baizer, The electrochemical route to adiponitrile. 1: Discovery. *Chemtech* **10**, 161–164 (1980).

6. A. Badalyan, S. S. Stahl, Cooperative electrocatalytic alcohol oxidation with electron-proton-transfer mediators. *Nature* **535**, 406–410 (2016). doi:10.1038/nature18008 Medline

7. E. J. Horn, B. R. Rosen, Y. Chen, J. Tang, K. Chen, M. D. Eastgate, P. S. Baran, Scalable and sustainable electrochemical allylic C–H oxidation. *Nature* **533**, 77–81 (2016). doi:10.1038/nature17431 Medline

8. J. Hartung, J. R. Norton, in *Catalysis Without Precious Metals*, R. M. Bullock, Ed. (Wiley, 2010), pp. 1–24.

9. S. W. M. Crossley, C. Obradors, R. M. Martinez, R. A. Shenvi, Mn-, Fe-, and Co-catalyzed radical hydrofunctionalizations of olefins. *Chem. Rev.* **116**, 8912–9000 (2016). doi:10.1021/acs.chemrev.6b00334 Medline

10. D. C. Miller, K. T. Tarantino, R. R. Knowles, Proton-coupled electron transfer in organic synthesis: Fundamentals, applications, and opportunities. *Top. Curr. Chem.* **374**, 30 (2016). doi:10.1007/s41061-016-0030-6 Medline

11. T. V. Chciuk, R. A. Flowers 2nd, Proton-coupled electron transfer in the reduction of arenes by SmI_2–water complexes. *J. Am. Chem. Soc.* **137**, 11526–11531 (2015). doi:10.1021/jacs.5b07518 Medline

12. D. Kim, S. M. W. Rahaman, B. Q. Mercado, R. Poli, P. L. Holland, Roles of iron complexes in catalytic radical alkene cross-coupling: A computational and mechanistic study. *J. Am. Chem. Soc.* **141**, 7473–7485 (2019). doi:10.1021/jacs.9b02117 Medline

13. G. Qiu, R. R. Knowles, Rate–driving force relationships in the multisite proton-coupled electron transfer activation of ketones. *J. Am. Chem. Soc.* **141**, 2721–2730 (2019). doi:10.1021/jacs.8b13451 Medline

14. Z.-W. Hou, Z.-Y. Mao, H.-B. Zhao, Y. Y. Melcamu, X. Lu, J. Song, H.-C. Xu, Electrochemical C−H/N−H functionalization for the synthesis of highly functionalized (aza)indoles. *Angew. Chem. Int. Ed.* **55**, 9168–9172 (2016). doi:10.1002/anie.201602616 Medline

15. M. J. Chalkley, T. J. Del Castillo, B. D. Matson, J. P. Roddy, J. C. Peters, Catalytic N_2-to-NH_3 conversion by Fe at lower driving force: A proposed role for metallocene-mediated PCET. *ACS Cent. Sci.* **3**, 217–223 (2017). doi:10.1021/acscentsci.7b00014 Medline

16. M. J. Chalkley, P. H. Oyala, J. C. Peters, Cp* noninnocence leads to a remarkably weak C–H bond via metallocene protonation. *J. Am. Chem. Soc.* **141**, 4721–4729 (2019). doi:10.1021/jacs.9b00193 Medline

17. M. J. Chalkley, T. J. Del Castillo, B. D. Matson, J. C. Peters, Fe-mediated nitrogen fixation with a metallocene mediator: Exploring pK_a effects and demonstrating electrocatalysis. *J. Am. Chem. Soc.* **140**, 6122–6129 (2018). doi:10.1021/jacs.8b02335 Medline

18. R. Cai, R. D. Milton, S. Abdellaoui, T. Park, J. Patel, B. Alkotaini, S. D. Minteer, Electroenzymatic C–C bond formation from CO_2. *J. Am. Chem. Soc.* **140**, 5041–5044 (2018). doi:10.1021/jacs.8b02319 Medline

19. R. A. Henderson, Protonation of unsaturated hydrocarbon ligands: Regioselectivity, stereoselectivity, and product specificity. *Angew. Chem. Int. Ed.* **35**, 946–967 (1996). doi:10.1002/anie.199609461

20. Y. Peng, M. V. Ramos-Garcés, D. Lionetti, J. D. Blakemore, Structural and electrochemical consequences of [Cp*] ligand protonation. *Inorg. Chem.* **56**, 10824–10831 (2017). doi:10.1021/acs.inorgchem.7b01895 Medline

21. J. J. Warren, T. A. Tronic, J. M. Mayer, Thermochemistry of proton-coupled electron transfer reagents and its implications. *Chem. Rev.* **110**, 6961–7001 (2010). doi:10.1021/cr100085k Medline

22. W.-Z. Liu, F. G. Bordwell, Gas-phase and solution-phase homolytic bond dissociation energies of H−N^+ bonds in the conjugate acids of nitrogen bases. *J. Org. Chem.* **61**, 4778–4783 (1996). doi:10.1021/jo950933r Medline

23. I. Kaljurand, A. Kütt, L. Sooväli, T. Rodima, V. Mäemets, I. Leito, I. A. Koppel, Extension of the self-consistent spectrophotometric basicity scale in acetonitrile to a full span of 28 pK_a units: Unification of different basicity scales. *J. Org. Chem.* **70**, 1019–1028 (2005). doi:10.1021/jo048252w Medline

24. T. H. Parsell, M.-Y. Yang, A. S. Borovik, C–H bond cleavage with reductants: Re-investigating the reactivity of monomeric Mn($^{III/IV}$)-oxo complexes and the role of oxo ligand basicity. *J. Am. Chem. Soc.* **131**, 2762–2763 (2009). doi:10.1021/ja8100825 Medline

25. S. Pattanayak, A. J. Jasniewski, A. Rana, A. Draksharapu, K. K. Singh, A. Weitz, M. Hendrich, L. Que Jr., A. Dey, S. Sen Gupta, Spectroscopic and reactivity comparisons of a pair of bTAML complexes with Fe^V═O and Fe^{IV}═O Units. *Inorg. Chem.* **56**, 6352–6361 (2017). doi:10.1021/acs.inorgchem.7b00448 Medline

26. C. Costentin, S. Drouet, M. Robert, J.-M. Savéant, Turnover numbers, turnover frequencies, and overpotential in molecular catalysis of electrochemical reactions. Cyclic voltammetry and preparative-scale electrolysis. *J. Am. Chem. Soc.* **134**, 11235–11242 (2012). doi:10.1021/ja303560c Medline

27. T. V. Chciuk, W. R. Anderson Jr., R. A. Flowers 2nd, Proton-coupled electron transfer in the reduction of carbonyls by samarium diiodide–water complexes. *J. Am. Chem. Soc.* **138**, 8738–8741 (2016). doi:10.1021/jacs.6b05879 Medline

28. C. Hansch, A. Leo, R. W. Taft, A survey of Hammett substituent constants and resonance and field parameters. *Chem. Rev.* **91**, 165–195 (1991). doi:10.1021/cr00002a004

29. M. K. Goetz, J. S. Anderson, Experimental evidence for pK_a-driven asynchronicity in C–H activation by a terminal Co(III)–oxo complex. *J. Am. Chem. Soc.* **141**, 4051–4062 (2019). doi:10.1021/jacs.8b13490 Medline

30. D. Bím, M. Maldonado-Domínguez, L. Rulíšek, M. Srnec, Beyond the classical thermodynamic contributions to hydrogen atom abstraction reactivity. *Proc. Natl. Acad. Sci. U.S.A.* **115**, E10287–E10294 (2018). doi:10.1073/pnas.1806399115 Medline

31. M. P. J. Brennan, O. R. Brown, Mechanism of the cathodic reduction of acetophenone in acidic aqueous-methanolic media. *J. Chem. Soc., Faraday Trans. 1* **69**, 132–142 (1973). doi:10.1039/f19736900132

32. F. Wang, S. S. Stahl, Electrochemical oxidation of organic molecules at lower overpotential: Accessing broader functional group compatibility with electron−proton transfer mediators. *Acc. Chem. Res.* **53**, 561–574 (2020). doi:10.1021/acs.accounts.9b00544 Medline

33. Y. Tanabe, K. Nakajima, Y. Nishibayashi, Phosphine oxidation with water and ferrocenium(III) cation induced by visible-light irradiation. *Chemistry* **24**, 18618–18622 (2018). doi:10.1002/chem.201805129 Medline

34. K. Kato, W. Kim, D. Kim, H. Yorimitsu, A. Osuka, Porphyrin analogues of a trityl cation and anion. *Chemistry* **22**, 7041–7045 (2016). doi:10.1002/chem.201600473 Medline

35. A. G. Osborne, Long range cyano ^{13}C–^{1}H coupling constants in some cyanopyridines and benzonitriles. *Spectrochim. Acta A Mol. Biomol. Spectrosc.* **53**, 2475–2480 (1997). doi:10.1016/S1386-1425(97)00150-9

36. K. Abdur-Rashid, T. P. Fong, B. Greaves, D. G. Gusev, J. G. Hinman, S. E. Landau, A. J. Lough, R. H. Morris, An acidity scale for phosphorus-containing compounds including metal hydrides and dihydrogen complexes in THF: Toward the unification of acidity scales. *J. Am. Chem. Soc.* **122**, 9155–9171 (2000). doi:10.1021/ja994428d

37. F. Neese, The ORCA program system. *WIREs Comput. Mol. Sci.* **2**, 73–78 (2012). doi:10.1002/wcms.81

38. F. Neese, Software update: The ORCA program system, version 4.0. *WIREs Comput. Mol. Sci.* **8**, e1327 (2018). doi:10.1002/wcms.1327

39. J. Tao, J. P. Perdew, V. N. Staroverov, G. E. Scuseria, Climbing the density functional ladder: Nonempirical meta-generalized gradient approximation designed for molecules

and solids. *Phys. Rev. Lett.* **91**, 146401–146404 (2003). doi:10.1103/PhysRevLett.91.146401 Medline

40. F. Weigend, R. Ahlrichs, Balanced basis sets of split valence, triple zeta valence and quadruple zeta valence quality for H to Rn: Design and assessment of accuracy. *Phys. Chem. Chem. Phys.* **7**, 3297–3305 (2005). doi:10.1039/b508541a Medline

41. F. Weigend, Accurate Coulomb-fitting basis sets for H to Rn. *Phys. Chem. Chem. Phys.* **8**, 1057–1065 (2006). doi:10.1039/b515623h Medline

42. S. Grimme, J. Antony, S. Ehrlich, H. Krieg, A consistent and accurate ab initio parametrization of density functional dispersion correction (DFT-D) for the 94 elements H-Pu. *J. Chem. Phys.* **132**, 154104 (2010). doi:10.1063/1.3382344 Medline

43. A. V. Marenich, C. J. Cramer, D. G. Truhlar, Universal solvation model based on solute electron density and on a continuum model of the solvent defined by the bulk dielectric constant and atomic surface tensions. *J. Phys. Chem. B* **113**, 6378–6396 (2009). doi:10.1021/jp810292n Medline

44. E. S. Wiedner, M. B. Chambers, C. L. Pitman, R. M. Bullock, A. J. M. Miller, A. M. Appel, Thermodynamic hydricity of transition metal hydrides. *Chem. Rev.* **116**, 8655–8692 (2016). doi:10.1021/acs.chemrev.6b00168 Medline

45. G. M. Sheldrick, Crystal structure refinement with SHELXL. *Acta Cryst.* **C71**, 3–8 (2015). doi:10.1107/S2053229614024218 Medline

46. O. V. Dolomanov, L. J. Bourhis, R. J. Gildea, J. K. Howard, H. Puschmann, OLEX2: A complete structure solution, refinement and analysis program. *J. Appl. Cryst.* **42**, 339–341 (2009). doi:10.1107/S0021889808042726

47. J. V. Macpherson, A practical guide to using boron doped diamond in electrochemical research. *Phys. Chem. Chem. Phys.* **17**, 2935–2949 (2015). doi:10.1039/C4CP04022H Medline

48. L. Chiang, W. Keown, C. Citek, E. C. Wasinger, T. D. P. Stack, Simplest monodentate imidazole stabilization of the oxy-tyrosinase Cu_2O_2 core: Phenolate hydroxylation through a Cu^{III} intermediate. *Angew. Chem. Int. Ed.* **55**, 10453–10457 (2016). doi:10.1002/anie.201605159 Medline

49. D. F. Evans, The determination of the paramagnetic susceptibility of substances in solution by nuclear magnetic resonance. *J. Chem. Soc.* **1959**, 2003–2005 (1959). doi:10.1039/jr9590002003

50. B. D. McCarthy, D. J. Martin, E. S. Rountree, A. C. Ullman, J. L. Dempsey, Electrochemical reduction of Brønsted acids by glassy carbon in acetonitrile-implications for electrocatalytic hydrogen evolution. *Inorg. Chem.* **53**, 8350–8361 (2014). doi:10.1021/ic500770k Medline

51. S. Stoll, A. Schweiger, EasySpin, a comprehensive software package for spectral simulation and analysis in EPR. *J. Magn. Reson.* **178**, 42–55 (2006). doi:10.1016/j.jmr.2005.08.013 Medline

52. J. H. Ammeter, EPR of orbitally degenerate sandwich compounds. *J. Magn. Reson. (1969)* **30**, 299–325 (1978). doi:10.1016/0022-2364(78)90103-8

53. J. H. Ammeter, J. D. Swalen, Electronic structure and dynamic Jahn-Teller effect of cobaltocene from EPR and optical studies. *J. Chem. Phys.* **57**, 678–698 (1972). doi:10.1063/1.1678300

54. J. Hulliger, L. Zoller, J. H. Ammeter, Orientation effects in EPR powder samples induced by the static magnetic field. *J. Magn. Reson. (1969)* **48**, 512–518 (1982). doi:10.1016/0022-2364(82)90082-8

55. C. Costentin, J.-M. Savéant, Multielectron, multistep molecular catalysis of electrochemical reactions: Benchmarking of homogeneous catalysts. *ChemElectroChem* **1**, 1226–1236 (2014). doi:10.1002/celc.201300263

56. G. Wilkinson, P. L. Pauson, F. A. Cotton, Bis-cyclopentadienyl compounds of nickel and cobalt. *J. Am. Chem. Soc.* **76**, 1970–1974 (1954). doi:10.1021/ja01636a080

57. X. Chen, X. Wang, Y. Sui, Y. Li, J. Ma, J. Zuo, X. Wang, Synthesis, characterization, and structures of a persistent aniline radical cation. *Angew. Chem. Int. Ed.* **51**, 11878–11881 (2012). doi:10.1002/anie.201205478 Medline